



저작자표시-비영리-변경금지 2.0 대한민국

이용자는 아래의 조건을 따르는 경우에 한하여 자유롭게

- 이 저작물을 복제, 배포, 전송, 전시, 공연 및 방송할 수 있습니다.

다음과 같은 조건을 따라야 합니다:



저작자표시. 귀하는 원저작자를 표시하여야 합니다.



비영리. 귀하는 이 저작물을 영리 목적으로 이용할 수 없습니다.



변경금지. 귀하는 이 저작물을 개작, 변형 또는 가공할 수 없습니다.

- 귀하는, 이 저작물의 재이용이나 배포의 경우, 이 저작물에 적용된 이용허락조건을 명확하게 나타내어야 합니다.
- 저작권자로부터 별도의 허가를 받으면 이러한 조건들은 적용되지 않습니다.

저작권법에 따른 이용자의 권리는 위의 내용에 의하여 영향을 받지 않습니다.

이것은 [이용허락규약\(Legal Code\)](#)을 이해하기 쉽게 요약한 것입니다.

[Disclaimer](#)

공학박사학위논문

**High Harmonic Combustion Instability Characteristics
of H₂/CH₄ Fuel in a Partially Premixed Combustor**

**부분예혼합 연소기에서 H₂/CH₄ 연료조성 변화에
따른 고주파 공진 불안정 특성**

2017년 2월

서울대학교 대학원

기계항공공학부

윤 지 수

ABSTRACT

Advancing the current technology of power-generation sources is essential because of increasing concerns related to emission regulations and the specific necessity of reducing emissions of CO₂. The main source of power generation is slowly changing from fossil fuels to renewable energy sources. However, renewable energy technology is not adequate at this time to replace the total amount of power generated by fossil fuels. Therefore, interest is increasing in the combined-cycle gas turbine, which is both efficient and eco-friendly. The gas turbine, the core technology of the combined cycle, has better emission characteristics compared to those of the coal-fired plant, and can be easily applied to new fuels including Syngas, Synthetic Natural Gas (SNG), and gas extracted from shale. The newer fuels contain a higher H₂ composition, which has been shown to be correlated with problems related to flashback. A different approach to minimize the disadvantage of higher H₂ composition is essential. Therefore, partially premixed or diffusion-type combustion systems were introduced to minimize hazards based on combustion characteristics (including flashback). Various fuel compositions must be usable and detailed research must inform fuel composition, with the minimization of combustion instability being one of the key issues for these new types of turbines.

This paper details a set of experiments related to combustion instability and how it is affected by the fuel composition in the partially premixed combustor. The reason of high harmonic instability mode shifting and the categorization of the occurred multi-mode instability were investigated. In addition, the flame transfer function was also measured to form a foundation of research that could predict the high harmonic combustion instability.

The first step of these experiments was to examine the H₂/CH₄/CO composition variation in 45 test cases conducted to delineate the characteristics of the combustor. Combustion instabilities primarily occurred in fuel including H₂, CH₄ composed fuel

composition and the mode analysis of each instability cases were conducted. Combustion instabilities in the partially premixed combustor were found in the 3rd, 4th, and 6th harmonic modes of the longitudinal fundamental mode. The fuel composition was reduced as H_2/CH_4 to conduct intensive research into instability characteristics. Combustor length and load variation tests were conducted to this end; the instabilities that occurred were confirmed as occurring in the longitudinal mode during the combustor length variation tests. In addition, high harmonic instability and instability-related mode shifting were found.

One of the specific objectives was to build understanding of the reasons for high harmonic combustion instability. The combustion instability mode varied from the 1st mode to the 6th mode with variations in the fuel composition. The other parameters (such as air flow rate and equivalence ratio) were varied to find the reason for instability mode shifting. From the parametric study, the structural variation of the flame was suspected to be the main parameter for instability mode shifting, and related to the convection time in time-lag analysis. Therefore, the simplified convection times of all cases were calculated based on OH planar laser-induced fluorescence (OH-PLIF) flame images, leading to finding the inverse relationships between convection time and the instability mode/frequency shifting. The convection-time reductions directly related to the decrease in total time delay is the main reason for shifts in the instability mode/frequency, which were analyzed based on the simplified Rayleigh criterion. In conclusion, the reduction of the combustion system's convection time is the main reason for instability mode shifting.

During the instability mode shifting analysis, the complex multi-mode occurrence were found in some experimental cases. The measured instability cases were categorized based on the time and frequency domain in 6 cases. The continuous wavelet transform was applied in these representative cases to determine the frequency characteristics during the time variations. In detail, the multi-mode instability can be divided into two cases. In one case, the various frequencies co-existed during the entire period of instability; in the other case, one of the dominant frequencies was found, but its duration was very short (i.e., its intermittency characteristics were found). The removal of multi-mode instability cases in the convection time–instability frequency graph, which were

found during mode-shifting analysis, shows the distinct convection time range of each mode. Convection-time overlapping indicated that the condition satisfies several instability modes at the same time. In conclusion, the reason for multi-mode instability is the co-satisfaction of multiple potential regions of instability.

Finally, the flame transfer function, which can be directly used in the instability prediction, was measured at different selected instability conditions. The flame transfer function gain decreasing tendency and flame transfer function phase decreasing gradient reduction was found during the increase of H₂ composition. The increase of H₂ composition directly related with the increase of volume flow rate of the fuel and it can reduce the inlet perturbation delivery time. In addition, the importance of flame structure and convection time was found based on the airflow rate and equivalence ratio variation tests. The measured flame transfer function gain was compared with that reported in previous research to determine the reasons for the trend. Last, the measured flame transfer function was used to predict the combustion instability phenomenon. The prediction results successfully follow the characteristics of instability mode shifting. These results allowed confirmation of accurate prediction of instability based on an accurate flame transfer function.

The high harmonic instability characteristics in a partially premixed combustor during various fuel compositions were understandable based on the experimental approach. In addition, accurate predictions of the possibility of instability were also made based on the measurements yielded by the flame-transfer function. Hopefully, these results can be used as the basic parameter for the development of a fuel-flexible gas turbine that uses premixed fuel with a high H₂ composition.

Keywords: Partially Premixed Combustor, Combustion Instability, Fuel Flexibility, High Harmonic Instability, Instability Mode Shifting, Multi-Mode, Flame Transfer Function, OH-PLIF, PIV, Instability Prediction.

Student Number: 2012-30180

LIST

ABSTRACT	i
LIST	iv
LIST OF FIGURES	vi
LIST OF TABLES	xi
NOMENCLATURE	xii
CHAPTER 1	
INTRODUCTION	1
CHAPTER 2	
EXPERIMENT AND MEASUREMENT SYSTEMS.....	9
2.1 Combustor and Nozzles.....	9
2.2 Flame Imaging.....	12
2.2.1 Chemiluminescence Spectroscopy.....	12
2.2.2 Abel Transform	14
2.3 Laser Diagnostics	15
2.3.1 OH PLIF Measurements	15
2.3.2 PIV Measurements.....	20
2.4 Flame Transfer Fucntion Measurement.....	24
2.5 Continuous Wavelet Transfrom	27
2.6 Instability Prediction by 1D Lumped Newsork Model.....	30
CHAPTER 3	
COMBUSTION CHARACTERISTICS IN	
VARIOUS FUEL COMPOSITION	31
3.1 Objectives and Test Conditions	31
3.2 Combustion Instability Characteristics.....	35

3.2.1 Effects of heat input and inlet temperature variations.....	35
3.2.2 Classification of the instability conditions.....	37
3.3 Instability Analysis	39
3.3.1 Instability mode analysis.....	39
3.3.2 Flame structure analysis based on H ₂ composition.....	41
3.3.3 Dump plane temperature analysis based on the flame structure	44
3.3.4 Effects of combustor length on combustion instability.....	47
CHAPTER 4	
HIGH HARMONIC INSTABILITY CHARACTERISTICS	51
4.1 Objectives and Test Conditions	51
4.2 Instability Mode Shifting.....	54
4.2.1 Variable Effects in Instability Mode Shifting.....	55
4.2.2 Convection Time Approach	57
4.2.3 Detailed Instability Mode Shifting Mechanism	64
4.3 Multi-mode Instability Characteristics	70
4.3.1 Instability Categorization.....	70
4.3.2 Reason of Multi-mode Instability	78
CHAPTER 5	
FLAME TRANSFER FUNCTION.....	88
5.1 Objectives and Test Conditions	88
5.2 Flame Transfer Function Characteristics	90
5.3 Gain Trend Analysis	93
5.4 Instability Prediction.....	96
CHAPTER 6	
CONCLUSION.....	98
REFERENCES.....	101
ABSTRACT IN KOREAN.....	110

LIST OF FIGURES

Fig. 1.1	Electricity generation by fuel (a) OECE countries (b) United States of America (c) Korea.	1
Fig. 2.1	Schematic diagram of the partially premixed gas turbine test facility.	9
Fig. 2.2	Schematic diagram of measurements sensor location (a) model combustor (b) cross-sectional view of fuel nozzle (c) direct photo of tested fuel nozzle.	11
Fig. 2.3	Schematic of relaxation processes emission of photons.	15
Fig. 2.4	OH excitation spectrum; In this study, $Q_1(6)$ was used for OH PLIF.	16
Fig. 2.5	OH fluorescence spectrum for $Q_1(6)$.	17
Fig. 2.6	Transmittance of filter (a) WG-305 (b) UG-11.	18
Fig. 2.7	Schematic diagram of OH-PLIF measurement system.	18
Fig. 2.8	Schematic diagram of PIV measurement system.	20
Fig. 2.9	Principle of typical PIV system.	21
Fig. 2.10	Field of view of PIV and OH-PLIF measurement.	23
Fig. 2.11	Change of continuous wavelet transform results according to wavelet changes.	25
Fig. 2.12	Schematic diagram of the FTF measurement system.	27
Fig. 2.13	Modulation amplitude effects on FTF characteristics (a) $H_2 : CH_4 = 25 : 75$, (b) $H_2 : CH_4 = 50 : 50$.	28
Fig. 3.1	Fuel composition sets for each load and inlet temperature test.	31
Fig. 3.2	Calculated Lewis number variation based on fuel composition change.	34
Fig. 3.3	Ternary diagram of the RMS dynamic pressure amplitude at the dump plane (a) 40 kW heat input, 473K inlet air temperature (b) 50 kW heat input, 473K inlet air temperature.	35
Fig. 3.4	Ternary diagram of the RMS dynamic pressure amplitude at the dump plane, 40 kW heat input, 629K inlet air temperature condition.	36
Fig. 3.5	Combustion instability frequency classification of the ternary stability	38

	map (a) 40 kW heat input, 473K inlet air temperature (b) 40 kW heat input, 629K inlet air temperature.	
Fig. 3.6	Mode analysis based on the RMS pressure amplitude of each dynamic sensor location (a) case 1, 750 Hz instability (b) case 2, 1000 Hz instability (c) case 3, 1500 Hz instability.	40
Fig. 3.7	Averaged OH chemiluminescence images of each fuel composition at the 40 kW heat input and 473k inlet air temperature condition.	41
Fig. 3.8	Abel inverted images of each fuel composition at the 40 kW heat input and 473k inlet air temperature condition.	42
Fig. 3.9	Instantaneous flame edge (a) H ₂ :CH ₄ = 25:75, (b) H ₂ :CH ₄ = 50:50, (c) H ₂ :CH ₄ = 75:25 and averaged flame (d) H ₂ :CH ₄ = 25:75, (e) H ₂ :CH ₄ = 50:50, (f) H ₂ :CH ₄ = 75:25 measured by 7 kHz OH-PLIF.	43
Fig. 3.10	Dump pane temperature fluctuation based on the combustion stability (a) 40 kW, 473K inlet air temperature (b) 40 kW, 629K inlet air temperature.	44
Fig. 3.11	Phase-averaged and Abel-inverted OH chemiluminescence image for the unstable condition near 1,000 Hz.	45
Fig. 3.12	Phase-resolved instantaneous OH-PLIF images, measured in the unstable condition.	46
Fig. 3.13	Dynamic pressure amplitude and frequency plots in various fuel composition, heat load and combustor length.	47
Fig. 3.14	Flame structure variation based on OH chemiluminescence during the combustor length variation at fixed H ₂ :CH ₄ = 37.5:62.5 fuel composition and 40kW heat input.	48
Fig. 3.15	Measured combustor temperature variation during the combustor length variation at fixed H ₂ :CH ₄ = 37.5:62.5 fuel composition and 40kW heat input.	48
Fig. 3.16	Instability frequency and mode shifting results while the variation of the combustor length from 1160mm to 1400mm (a) 40kW, H ₂ :CH ₄ = 37.5:62.5, (b) 45kW, H ₂ :CH ₄ = 75.0:25.0.	49

Fig. 4.1	Calculated chemical properties based on GRI 3.0 mechanism (a) adiabatic flame temperature (b) laminar flame speed.	53
Fig. 4.2	FMS tendency during fuel composition variations.	54
Fig. 4.3	(a) Instability frequency and (b) Averaged OH-PLIF images according to the airflow rate at $\phi=0.56$.	55
Fig. 4.4	(a) Instability frequency and (b) Averaged OH-PLIF images according to ϕ at a $\dot{V}_{air}=1,100$ slpm.	56
Fig. 4.5	Mixing length and convection time differences for the mixing type of the combustor based on time-lag analysis (a) premixed combustor and (b) partially premixed combustor.	58
Fig. 4.6	Schematic flame structure and the unburned mixture length.	59
Fig. 4.7	Calculated τ_{conv_global} and combustion instability frequency.	60
Fig. 4.8	Velocity field mapped with OH-PLIF images at (a) $H_2:CH_4 = 25:75$, (b) $H_2:CH_4 = 50:50$, and (c) $H_2:CH_4 = 75:25$. The unburned mixture region is shown as yellow lines, and the velocity field is depicted as white arrows.	62
Fig. 4.9	Calculated τ_{conv_real} and combustion instability frequency.	63
Fig. 4.10	Schematic prediction of the 3rd mode occurrence process based on the time-lag approach in a short $\tau_{conv_{(3)}}$ condition. ($\tau_{etc} = \tau_{acoustic} + \tau_{chemical} + \tau_{ignition}$)	64
Fig. 4.11	Calculated parameters and instability FMS (a) adiabatic flame temperature (b) laminar flame speed.	65
Fig. 4.12	Inverse relation between calculated parameters and FMS (a) invers of adiabatic flame temperature (b) invers of laminar flame speed (c) global convection time.	66
Fig. 4.13	Application τ_{conv} approach in the previous research related with the instability FMS phenomenon. (a) T. Lieuwen, (b) R. Balachandran, (c) S.J. Shanbhogue	67
Fig. 4.14	Convection time, instability frequency and instability amplitude relation.	67
Fig. 4.15	Schematic analysis of instability FMS during the combustor length	68

	variation (a) Instability FMS trends during the combustor length variation and Simplified time-lag analysis (b) case 1 (c) case 2 (d) case 3.	
Fig. 4.16	Definition of convection time based on OH PLIF.	70
Fig. 4.17	Instability mode shifting characteristics of various test conditions. (a) Relation between the calculated convection time and instability frequency. (b) Instability of the possible region base in a simplified time-lag analysis.	71
Fig. 4.18	Combustion instability categorization based on the time and frequency domain. (a) Time domain: periodic. (b) Time domain: dynamic. (c) Frequency domain: single instability. (d) Frequency domain: dual instability. (e) Frequency domain: multiple frequency instability.	73
Fig. 4.19	Overall trend and specific cycle of the steady unstable condition characteristics based on the time domain pressure signal: (a) Case 1 (periodic: single instability), (b) Case 2 (periodic: dual instability), (c) Case 3 (periodic: multiple instability).	75
Fig. 4.20	Comparison of the measured time domain signal and reconstructed signal, Case 2 (periodic: dual instability)	75
Fig. 4.21	Overall trend and specific cycle of unsteady unstable condition characteristics based on the time domain pressure signal: (a) Case 4 (dynamic: single instability), (b) Case 5 (dynamic: dual instability), (c) Case 6 (dynamic: multiple instability).	76
Fig. 4.22	Frequency domain characteristics comparison between periodic and dynamic instability conditions. Cases: (a) 1, (b) 2, (c) 3, (d) 4, (e) 5, (f) 6.	77
Fig. 4.23	Applied results in the continuous wavelet transform in the periodic instability condition. (a) Case 1, (b) Case 2, (c) Case 3.	79
Fig. 4.24	Applied results of the continuous wavelet transform in a dynamic instability condition. (a) Case 4, (b) Case 5, (c) Case 6.	80
Fig. 4.25	Continuous wavelet transform application in the intermittency condition of instability. (a) High-frequency to low-frequency shifting region (b)	81

	Low-frequency to high-frequency shifting and drastic amplitude fluctuating region.	
Fig. 4.26	Instability occurrence possibility of each type based on categorized test condition.	82
Fig. 4.27	Simplified calculated convection time and frequency based on categorized test conditions (upper) and the removal of the multi-mode instability occurrence condition (lower).	83
Fig. 4.28	Simplified Rayleigh's criteria of each instability case (a) single mode instability (b) multi-mode instability (green area indicates the positive Rayleigh index (instability possible region) and black area indicates the total time delay between pressure wave and heat release).	84
Fig. 4.29	Simplified calculated convection time and frequency based on dual frequency instability cases (upper) and multiple frequency instability cases (lower).	86
Fig. 5.1	Measured FTF under varying fuel compositions; (a) FTF gain and phase (b) phase normalized by the Strouhal number (St).	90
Fig. 5.2	Measured FTF gain for (a) airflow rate and (b) ϕ variations.	92
Fig. 5.3	Measured FTF gain trend comparison between premixed and partially premixed combustor (a) CNRS, (b) present study.	93
Fig. 5.4	Block diagram representation of mechanisms generating heat-release rate fluctuations in swirling flows (Candel et al. 2014).	94
Fig. 5.5	Constructive and destructive interaction between flame breathing motion and flame angle oscillation in the FTF gain.	95
Fig. 5.6	Fig. 5.6 Instability FMS phenomenon during the fuel composition variation (a) experimental results, (b) flame location considered prediction results.	97

LIST OF TABLES

Table 1.1	Emission characteristics in various power generation systems (IEA 2012).	2
Table 1.2	Categorized combustion instability prediction research.	6
Table 2.1	Formation and destruction of OH radical.	15
Table 2.2	High-speed PLIF application research summary.	19
Table 2.3	Summary of flow modulation device and application	27
Table 3.1	Summary of the fuel composition test conditions.	32
Table 3.2	Representative conditions for classification of the mode analysis at 40 kW heat input, 473K inlet air temperature.	39
Table 3.3	Measured and calculated frequency comparison of each representative instability case.	40
Table 4.1	High harmonic instability test conditions.	52
Table 4.2	Selected test conditions for each of the six categorized cases	74
Table 5.1	Flame transfer function test conditions	88

NOMENCLATURE

Alphabet

AES	Atomic Emission Spectroscopy
A-USC	Advanced Ultra-supercritical
CCGT	Combined Cycle Gas Turbine
CCS	Carbon Capture and Storage
CFD	Computational Fluid Dynamics
DME	Dimetylene ether
FFT	Fast Fourier Transform
FMS	frequency/mode shifting
IEA	International Energy Agency
IGCC	Integrated Gasification Combined Cycle
IGFC	Integrated Gasification Fuel Cell
MFC	Mass flow controller
OECD	Organization for Economic Co-operation and Development
PLIF	Planar Laser Induced Fluorescence
PIV	Particle Image Velocimetry
PMT	Photon multiplier tube
RMS	Root Mean Square
SNG	Synthetic Natural Gas
USC	Ultra-supercritical
D_{swirl_in}	inner diameter of swirler
D_{swirl_out}	outer diameter of swirler
l_{ub}	equally divided local length along the mixture trajectory
L_{ub}	length of the convective path in the unburned mixture region
$P'(3)$	3rd dynamic pressure sensor
\dot{q}	heat release rate fluctuation
q_{mean}	average heat release rate

r	radial location from the origin in chemiluminescence image
s	scale parameters in continuous wavelet transform
S'	swirl number fluctuation
S	swirl number
u	axial average velocity
u'	axial velocity fluctuation
u_l	local velocity at each local distance
\dot{u}	inlet velocity fluctuation
u_{mean}	average inlet velocity
U_e	simplified mean exit velocity at the fuel nozzle
v	radial average velocity
v'	radial velocity fluctuation
y	axial location from the origin in chemiluminescence image
θ	swirl vane angle
τ	translation parameters in continuous wavelet transform
τ_{conv}	convection time
$\tau_{\text{conv_global}}$	global convection time
$\tau_{\text{conv_real}}$	real convection time base on PIV
$\psi(t)$	transformation function in continuous wavelet transform

Subscript

ub	unburned mixture region
e	nozzle exit
l	local

CHAPTER 1

INTRODUCTION

Fig. 1.1(a) shows the total electricity generation as of 2015 according to the Organization of Economic Co-operation and Development (OECD) [1]. Electricity generation and consumption has gradually increased based on the energy balance among the countries that comprise the OECD [1]. The portion of oil and nuclear energy used to generate electricity gradually decreased in recent decade, with the share of natural gas increasing. The trend towards using natural gas for power generation can be clearly found in the statistics of the United States of America. The active development of shale gas in recent years directly influences the share of electricity generation by fuel. The gas share with respect to energy generation has also increased for the Republic of Korea. These trends show the importance of gas as a fuel for power generation, as shown in Fig. 1.1(c).

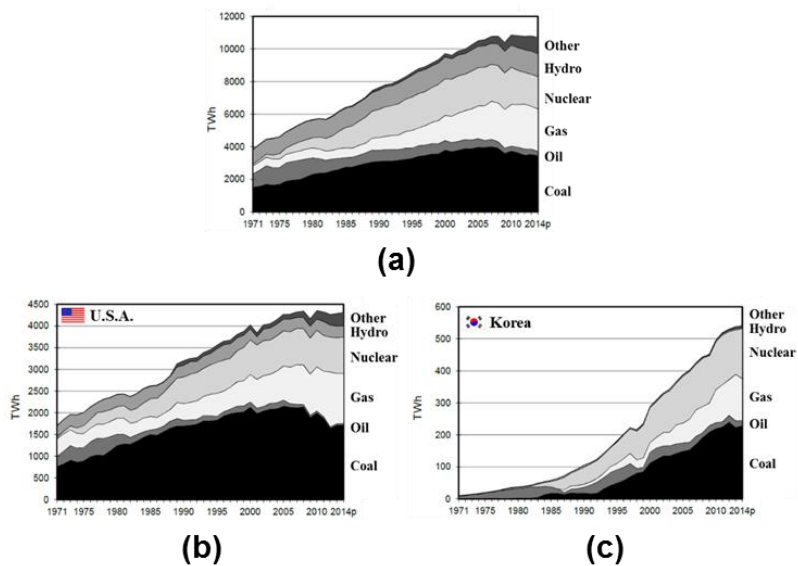


Fig. 1.1 Electricity generation by fuel (a) OECE countries (b) United States of America (c) Korea

As mentioned before, sources of power generation can be conventionally separated into nuclear, coal, gas, oil, and renewable energy. However, nuclear-based power generation includes the basic danger of radioactivity and the problem of disposing of radioactive waste. In addition, the technical maturity of wind, solar, geo-thermal, and other newly tapped resources of energy (and the associated technology) is not adequate for these renewable energies to be a major power-generation source.

Conversely, the combined-cycle gas turbine shows possibilities for considerable power generation that also has a net positive impact on the environment. By comparing the combined-cycle gas turbine with the coal-fired power plant, environmental characteristics (such as the decrease of NO_x, SO_x, and particulate matter emissions and CO₂ reduction) drastically improve. As shown in Table. 1.1, the combined-cycle gas turbine basically cuts in half the CO₂ emissions with the same power-output generation, with no particulate. The higher efficiency of the combined-cycle gas turbine ($\approx 60\%$) compared to the coal-fired cycle ($\approx 40\%$) is the main reason for the reduction in emissions; the other main reason for the different emission characteristics is the fundamental difference in chemical properties between gaseous fuel (CNG, LNG, etc.) and coal is the other reason.

Table 1.1 Emission characteristics in various power generation systems (IEA 2012).

	Type	CO ₂ g/kWh	NO _x mg/Nm ³	SO _x mg/Nm ³	Particle	Power
Coal	USC	740	50~100	20~100	<10	1050
	A-USC	669	50~100	20~100	<10	<1000
	IGCC	669~740	<30	<20	<1	335
	IGFC	500~550	<30	<20	<1	500
Gas	CCGT	400	<20	0	0	410

In addition to the emissions-related advantages described above, the gas turbine has the advantage of being able to easily utilize renewable fuels such as Syngas, Synthetic Natural Gas (SNG), and shale gas among others. Syngas is yielded by a way to clean coal in transforming the solid fuel to gaseous fuel. Power plants use a syngas as part of what is

termed the Integrated Gasification Combined Cycle (IGCC); the fuel used in the plant detailed by this study is a mixture of mainly H_2 , CH_4 and CO . In addition, SNG is a fuel gas that can be produced from fossil fuels such as lignite coal and oil, rather than from biofuels. The composition of it is similar to that of natural gas, but the H_2 composition is slightly higher than that found in conventional fuel. Shale gas, a type of natural gas extracted from shale formations, has become an increasingly important source of natural gas in the United States. Interest in this technique has now spread to potential gas shales across the rest of the world. In 2000, shale gas provided only 1% of natural gas production in the U.S.; by 2010, this proportion had increased to more than 20%, and the U.S. Government's Energy Information Administration predicts that by 2035, 46% of the U.S. natural gas supply will come from shale gas. The composition of shale gas is the same as that of conventional natural gas.

These types of new fuels are concerning in terms of how gas turbines can be adapted for use in generating power. Therefore, major gas turbine manufacturers have put their efforts into developing fuel-flexible gas turbines that meet current environmental requirements. Two major issues exist in the current gas turbine development process: NO_x emissions must be minimized, and combustion instability suppressed. The H_2 composition of the new fuel is commonly higher than for conventional fuel, and the H_2 composition directly influences the characteristics of the combustion. Of note, the higher flame speed results in a higher possibility of flashback flames in a premixed-type combustion system. Therefore, the partially premixed combustion concept was introduced in fuel with a high H_2 composition to suppress flashback. Understanding the instability characteristics of H_2 composed fuel in the partially premixed combustor is essential for the gas turbine development process.

For example, performance tests of a multiple injection dry low NO_x combustor with H_2/CH_4 fuel were performed [2] and experimental investigation of thermo-acoustic oscillations in a syngas premixed multi-swirler model combustor was also conducted [3]. In addition, the effects that fuel composition had on flame structure and combustion dynamics in a lean premixed combustor was investigated [4] and the effect that syngas

mixture composition had on flashback and blowout was also studied [5, 6], .

A key issue in the development of the fuel-flexible gas turbine is combustion instability suppression. In the last decade, many researchers have focused on combustion instabilities and fuel effects on combustion instability. Research on combustion instability has been ongoing since it was first described in the early development of space propulsion engines and later in dry low-NO_x gas turbines. For the past three decades, a better understanding of the combustion instability mechanisms has been obtained from many studies on time-lag analysis[7, 8], flame/vortex interactions[9, 10], processing vortex core [11, 12], swirl strength fluctuation [13], swirl number fluctuations [14], and interference between acoustic and convective disturbances [15]. Improvements in measurement techniques, such as high-repetition rate planar laser-induced fluorescence (PLIF), have provided a deeper understanding and have facilitated the quantification of information about continuous flame behavior [16, 17]. Furthermore, the effect of fuel composition was studied by Noble et al. They determined that the syngas mixture composition affects flashback and blowout of H₂, CH₄ and CO composed fuel [18].

However, these studies have been conducted primarily using lean premixed combustors, whereas recent interest in fuel diversification and global warming has shifted the combustion concept from fully premixed to partially premixed types. The partially premixed combustion concept is preferred, as it achieves the mutual benefits of anti-flashback and NO_x reduction because the new fuels, such as biomass, SNG, and syngas derived from coal or wastes, contain considerable amounts of H₂. Allison et al. [19, 20], who utilized a partially premixed model combustor at the German Aerospace Center to investigate syngas and hydrocarbon fuels (CH₄, C₃H₈, and C₂H₄), found that the combustion instability frequency varied according to the fuel (i.e., when the flame speeds were matched, a similar combustion instability frequency was found). Lee et al. [21] observed a shifting phenomenon in both the instability frequency and mode with increases in the H₂ composition, and they suggested a new time scale of skewness for the precise application of a time-lag analysis in a partially premixed model combustor.

The combustion instability frequency/mode shifting (FMS) phenomenon was also

found during the airflow rate variation in a premixed natural gas combustor [22]. However, most researchers [22-25] have either reported FMS only phenomenologically or the FMS phenomenon was not the main topic. Therefore, the present study was conducted to investigate the characteristics of FMS, as well as to identify the reason for FMS from the longitudinal fundamental mode to other modes.

In addition, High multi-mode instability is not a well-known part of instability research. The cause of instability mode shifting based on various test parameters and FTF characteristics was identified in previous research [26]. Some studies have been conducted on higher mode characteristics during the combustion instability. Mullter et al. conducted an experimental study on self-excited combustion instability and compared the ratio between the 1st, 2nd, and 3rd modes [27]. Moreover, Hester et al. compared the time domain characteristics of 1st, 2nd and 3rd longitudinal modes in a rocket combustor [28]. In addition, higher mode occurrence characteristics based on the flame-describing function was studied by Noiray et al. [29]. Despite the above efforts, studies to identify the cause of multi-mode instability have rarely been undertaken in previous research. Therefore, the present study was conducted to investigate the characteristics and identify the cause of multi-mode instability in the partially premixed combustor.

The other main topic of interest during gas turbine development is instability prediction. Research about instability prediction can be separated into four categories: analytic solutions, lumped network models, large eddy simulation (LES), and experimental approaches. Table 1.2 shows the recent progress in each of these four categories. Experimental measurements, computational approaches, and the combination of experiments and computational fluid dynamics (CFD) are among the various ways that instability predictions are actively investigated. One of the key parameters for instability prediction is finding the relationship between the heat release and external fluctuation. Flame transfer function (FTF) is the main parameter that must be found before instability prediction, as summarized in Table 1.2, and a lot of research has been put into this function and its diverse applications. FTF is a transfer function that represents the relationships between input and output variables. The equivalence ratio or inlet velocity is commonly

selected as the input variable, with the heat release fluctuation of the flame normally selected as the output variable. FTF can be used to study combustor characteristics and to predict combustion instability.

Table 1.2 Categorized combustion instability prediction research.

Category	Year	Affiliation	Research Group	Contents
Analytic solution	2010	University of Leicester	P.D. Williams	Lean premixed FTF was compared with analytic formulation [30]
	2010	GIT	T. Lieuwen	G-equation based analytic solution [31]
	2011	CNRS	T. Schuller	Analytic model was compared with the experimental data [32]
	2012	MIT	A.F. Ghoniem	Analytic model was compared with the experimental data [33]
Lumped Network Model	2010	Alstom	W. Mohr	Transfer matrix was applied in the real scale swirl gas turbine [34]
	2011	CNRS	S. Candel	Non-linear characteristics of swirl flame was found by acoustic transfer matrix [25]
CFD	2013	Universitat Munchen	W. Polifke	Effects of thermal boundary condition on the flame dynamic characteristics [35]
Experimental Approach	2010	Pennsylvania State University	D.A. Santavicca	Non-linear characteristics of FTF and local FTF [36-40]
	2012	Queen Mary University of London	C. Lawn	Non-linear characteristics of CH ₄ flame [41]

Analytic and computational solutions using the nonlinear G equation during the disturbance were derived and compared to the experimental data by Preetham at GE [42]. Santavicca et al conducted the FTF measurements of turbulent premixed flames. The forced flame response of gas turbine can be quantitatively generalized using the flame shape and Strouhal number [36]. Various results were reported by the Candel group, and one of their experiments was conducted with the swirl premixed combustor. The flame describing function shows local minimum and maximum gain values. These experiments were also

well received by LES [43]. However, the previous FTF research used a narrow modulation frequency range and was mainly conducted in a premixed combustor [36, 43, 44]. The present study employed a wide range of modulations (0–1,000 Hz), and the effects of τ_{conv} at the FTF were determined by varying the fuel composition, airflow rate, and the ϕ .

In summary, the objectives of this study are to investigate the characteristics of high harmonic combustion instability that occurs in a partially premixed combustor, accounting for fuel composition variations and measuring the FTF. For these purposes, the following studies were performed:

1. In Chapter 3, the dynamic characteristics of a partially premixed combustor were found based on the $\text{H}_2/\text{CH}_4/\text{CO}$ composition variation. Combustion instability phenomena mainly occurred in the H_2/CH_4 composed fuel, and the 3rd-, 4th-, and 6th-mode longitudinal instability were measured from dynamic pressure data analysis. The fuel compositions were reduced in terms of amount of H_2/CH_4 , and combustor length and heat input variation tests were also conducted. The high harmonic frequencies of the longitudinal fundamental mode were found iteratively, and these were selected as the key phenomena of this study.
2. In Chapter 4, the characteristics of high harmonic instabilities were investigated based on fuel composition, airflow rate, and equivalence ratio variation tests. The instability mode/frequency shifting phenomenon and the multi-mode characteristics were studied. First, OH-PLIF-based simplified convection time was calculated to determine the reasons for instability mode shifting and the relationship between the convection time reduction and the shifts in the instability mode to higher harmonic modes were found. The mechanism of instability mode shifting was explained based on the simplified Rayleigh criterion. Second, the multi-mode instability characteristics were categorized based on the time and frequency domain approach. In addition, continuous wavelet transform was applied to find how instability characteristics evolved over time. Multi-mode occurrence of instabilities was introduced based on the overlapping of instability-possible regions using the Rayleigh criterion, and multi-mode instability was

separated as a co-existing multi-mode instability and travelling multimode instability.

3. Predicting the occurrence of combustion instability was the key question of the combustion instability study. The most complex parameter used to forecast the combustion instability occurrence is the heat release, and it must be modeled in common research for instability prediction. The FTF is a well-known approach for heat release modeling. In Chapter 5, the FTF was measured and its characteristics analyzed. First, the parameter variation effects on the gain and phase of the FTF were analyzed and related with the previously found instability characteristics. Second, the FTF gain trend was compared with the trend shown in a previous study, with the purpose of investigating the reasons for the existence of similar characteristics. Finally, the measured FTF was used for instability prediction, and the results compared with the instability mode shifting phenomenon from the experimental results.

CHAPTER 2

EXPERIMENT AND MEASUREMENT SYSTEMS

2.1 Combustor and Nozzles

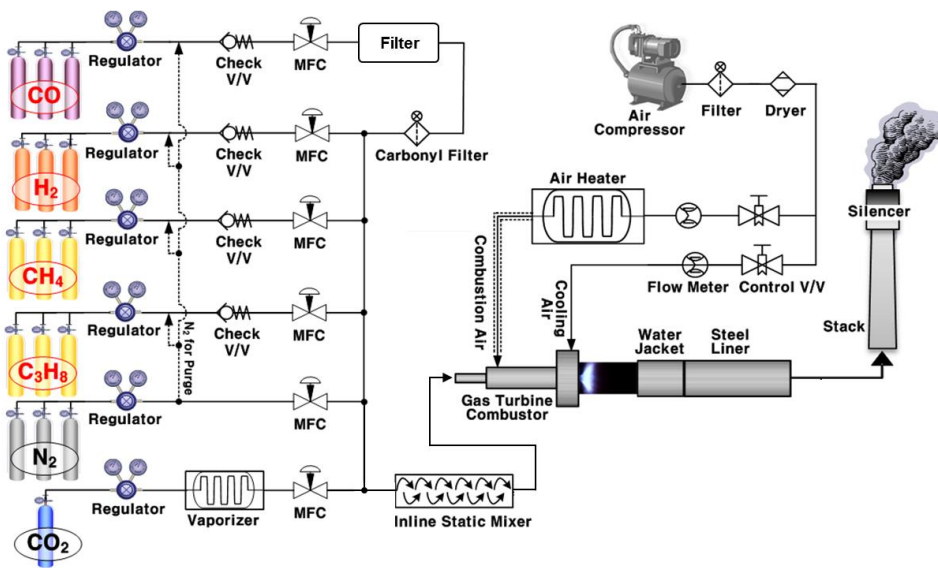


Fig. 2.1 Schematic diagram of the partially premixed gas turbine test facility.

For the purposes of this study, an atmospheric pressure high temperature combustion test facility for a 40 kW-scale gas turbine was installed. As shown in Fig 2.1 this facility consisted of an air compressor, an air heater, a cooling and combustion air feed line, an atmospheric pressure combustor, an external stack with silencer, and a fuel supplying system that can control the flow rate of H_2 , CO , CH_4 , N_2 and CO_2 respectively. Mass flow controller (MFC, Parker Porter 200, uncertainty: $\pm 1\%$ of full range) is used for the control of H_2 , CO , CH_4 , N_2 and CO_2 . The fuel gases were provided from each bottle of high-purity feedstock gases ($H_2 > 99.95$ mol%, $CO > 99.95$ mol%, $CH_4 > 99.9$ mol%). These gases were well mixed through the inline static mixer and injected to the combustor through 14

fuel injection holes within the inner side of swirl vanes at 2.7mm upstream of dump plane to satisfy the partially premixed flame condition. The reactivity of CO is very high and it can make carbonyl the reaction with the supply line and these carbonyl is directly influences the flame visualization quality, because it will be coated inside the quartz tube. Therefore, for CO supply, carbonyl trapping gas purifier (Entegris, 10MH) was installed upstream of inline mixer. To meet gas turbine relevant conditions, dry air at the temperature of 200 °C (± 5 °C) was supplied to the flame through a central annular swirling nozzle. The flow rate of combustion air was also controlled by a MFC (Bronkhorst F-206BI, uncertainty: $\pm 0.8\%$ of full range) and choke orifice is installed at the immediately upstream of the combustor to prevent the perturbation of supplying air by blocking the influence of pressure variation at the upstream flow. Combustion tests were conducted at slightly aviated pressure (1.1~1.2 bar) since 90% area of combustor outlet was blocked by water-cooled plug nozzle to form an acoustic boundary of combustion chamber outlet. The combustion air was supplied to the combustor at the rate of 1100 slpm in a dried condition and the quartz liner cooling air was also supplied at the 900 slpm. A fuel composition is varies according to the test subject.

To examine the combustion characteristics of the high H₂ composed fuel, a 1/3 scaled-down one can dump combustor of a GE7EA gas turbine was designed as model combustor. The partially premixed type combustor was used to minimize the hazard such as the flash back. Fig. 2.2 shows the schematic of the combustion test rig and details of the fuel nozzle. The combustion chamber consisted of two parts. The first part was made from optically accessible quartz, which was cooled by a high-pressure injection of the air. The second part was made from steel and it had water channel to protect the test facility. The cooling water flow rate was fixed as 4.4 slpm (= 73 g/s). The inner diameter and length of the combustion chamber was 130 mm and 1410 mm, respectively. As shown in Fig. 2.2 the fuel–air mixture was supplied through the annularly arranged fourteen swirl vanes of a 45 angle, and fuel was injected within the swirl vanes at 2.7 mm upstream of the dump plane to make a partially premixed flame. The detailed view of fuel-air mixing within the swirl vane is shown in Fig. 2.2b and the direct photo of fuel nozzle is Fig. 2.2c. The inner and outer

diameter of each swirl vane was 25.5 mm and 40 mm, respectively, and the swirl number was 0.832, which was calculated via the following Equation 2.1 [45]:

$$S_n = \frac{2}{3} \left[\frac{1 - (D_{swirl-in} / D_{swirl-out})^3}{1 - (D_{swirl-in} / D_{swirl-out})^2} \right] \tan \theta \quad (2.1)$$

Where $D_{swirl-in}$, $D_{swirl-out}$ and θ are inner diameter of swirler, outer diameter of swirler and swirl vane angle respectively.

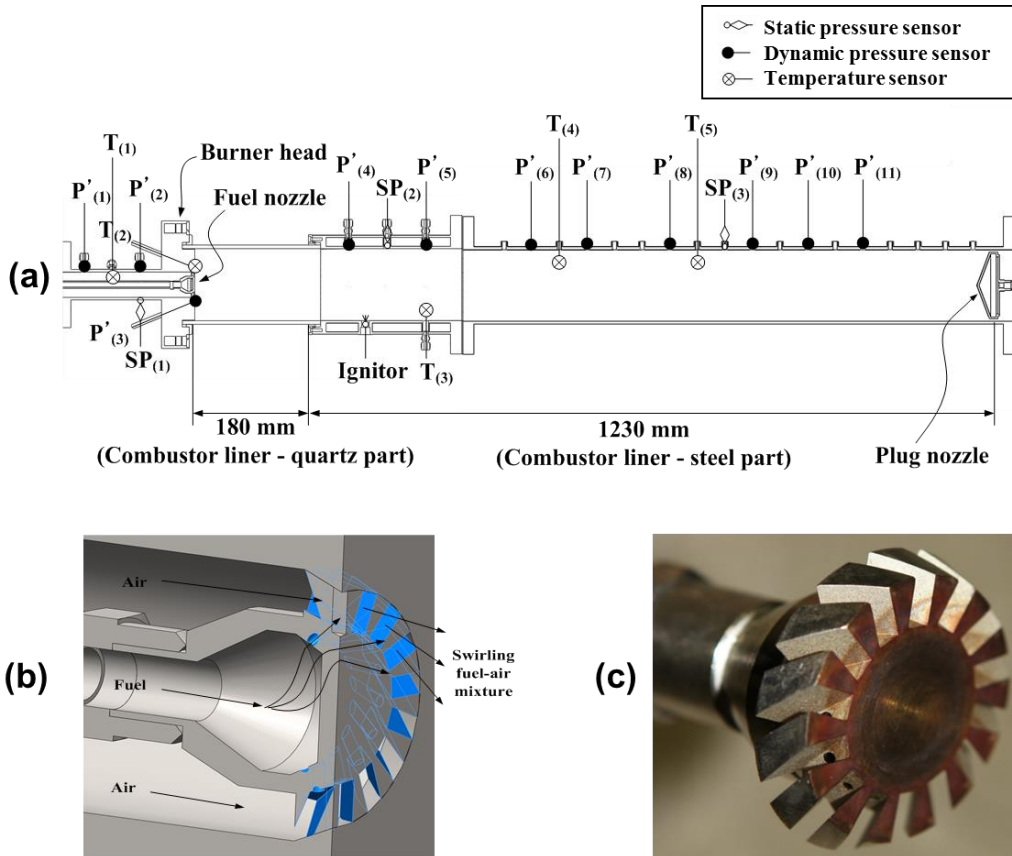


Fig. 2.2 Schematic diagram of measurements sensor location (a) model combustor (b) cross-sectional view of fuel nozzle (c) direct photo of tested fuel nozzle.

2.2 Flame Imaging

In this study, OH* chemiluminescence images were recorded to measure flame structure. Many other studies used direct photography to identify flame structure; however, images produced by this method are not good indicators of the reaction zone. The OH* chemiluminescence image should be used since OH radicals are good indicators of the reaction zone, which is a high temperature region. Thus, OH* chemiluminescence images were acquired using a ICCD camera (PI-MAX, Princeton Instruments, 512 × 512 pixel CCD) with a UV-Nikkor lens (f = 105 mm; f/4.5) and 307.1 ± 5 nm narrow bandpass filter. OH* chemiluminescence images were taken with 1 ms exposure time and 50 images were averaged for obtaining flame structure and observing flame behaviors in various fuel composition. The threshold value used to define the flame was 5% of the maximum intensity of the averaged image.

2.2.1. Chemiluminescence Spectroscopy

In chapter 3, OH* chemiluminescence measurements were conducted to obtain the reaction region. Chemiluminescence, like atomic emission spectroscopy (AES), uses quantitative measurements of the optical emission from excited chemical species to determine analyte concentration; however, unlike AES, chemiluminescence is usually defined as the emission from energized molecules instead of simply excited atoms. The bands of light determined by this technique emanate from molecular emissions and are therefore broader and more complex than bands originating from atomic spectra. Furthermore, chemiluminescence can take place in either the solution or gas phase, whereas AES is almost strictly as gas phase phenomenon. Like fluorescence spectroscopy, chemiluminescence strength lies in the detection of electromagnetic radiation produced in a system with very low background. On top of this, because the energy necessary to excite the analyte to higher electronic, vibrational, and rotational states (from which they can decay by emission) does not come from an external light source like a laser or lamp, the

problem of excitation source scattering is completely avoided. If the excitation energy for analyte in chemiluminescence is produced by a chemical reaction of the analyte and a reagent. An example of a reaction of this sort is shown below:



In gas phase chemiluminescence, the light emission (represented as $h\nu$) is produced by the reaction of an analyte (dimethyl sulfide in the above example) and a strongly oxidizing reagent gas such as fluorine (in the example above) or ozone, for instance. The reaction occurs on a time scale such that the production of light is essentially instantaneous; therefore, most analyte systems simply mix analytes and the reagent in a small volume chamber directly. If the analytes are eluting from a gas chromatographic column than the end of the column is often fed directly into the reaction chamber itself. Since as much of the energy released by the reaction should (in the analyst's eye) be used to excite as many of the analyte molecules as possible, loss of energy via gas phase collisions is undesirable, and therefore a final consideration is that the gas pressure in the reaction chamber be maintained at a low pressure (~ 1 torr) by a vacuum pump in order to minimize the effects of collisional deactivation. It must be stated that the ambiguous specification of "products" in the above reaction is often necessary because of the nature and complexity of the reaction. In some reactions, the chemiluminescent emitters are relatively well known. In the above reaction the major emitter is electronically and vibrationally excited HF; however, in the same reaction, other emitters have been determined whose identities are not known. To the analytical chemist the ambiguity about the actual products in the reaction is, in most case, not important. All the analyst cares about is the sensitivity of the instrument (read detection limits for target analytes), its selectivity-that is, response for an analyte as compared to an interfering compound, and the linear range of response.

2.2.2. Abel Transform

Abel convolution is one of optical diffraction tomography and integral transform, such as onion peeling method and back-projection algorithm. It is useful to transfer a 3-dimensional line-of-sight image to a 2-dimensional profile. The light emission measurement of chemiluminescence cannot capture the fine flame structure, because the signal is integrated through the depth of the flame. Therefore, each image was processed with Abel convolution. With Abel inverted images, the time-averaged flame structure profile can be reconstructed, if the flame shape is axisymmetric.

In mathematics, the Abel transformation, named for Niels Henrik Abel, is an integral transform often used in the analysis of spherically symmetric or axially symmetric functions. The Abel transform of a function $f(r)$ is given by:

$$F(y) = 2 \int_y^{\infty} \frac{f(r) r dr}{\sqrt{r^2 - y^2}} \quad (2.3)$$

Assuming $f(r)$ drops to zero more quickly than $1/r$, the inverse Abel transform is given by:

$$f(r) = -\frac{1}{\pi} \int_r^{\infty} \frac{dF}{dy} \frac{dy}{\sqrt{r^2 - y^2}} \quad (2.4)$$

In Chapter 3, the OH^* chemiluminescence signal was processed through inverse Abel transform to transfer a 3D line-of-sight image into a 2D flame profile and the OH radical is treated as a marker of heat release in a reaction zone.

2.3 Laser Diagnostics

2.3.1. OH PLIF Measurement

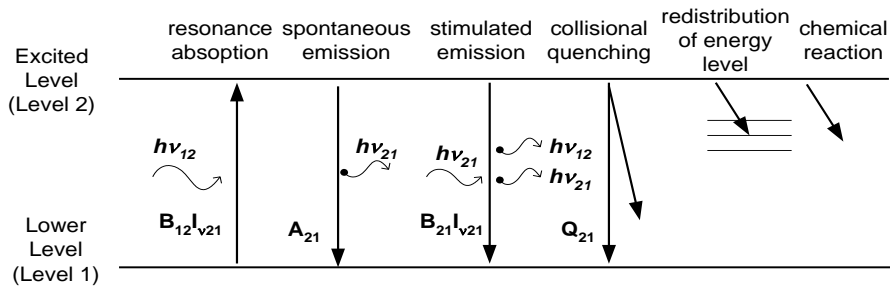


Fig. 2.3 Schematic of relaxation processes emission of photons.

Laser induced fluorescence (LIF) is described as the absorption of a photon by a molecule of radical, followed by an emission of a photon as the molecules undergoes the transition from a higher level energy state to a lower one. Figure 2.3 shows the schematic of energy transfer process. Some of the molecules will relax to the initial state by emission of photon. Several relaxation processes are possible including (a) spontaneous emission, (b) stimulated emission by exterior stimulus, (c) quenching by collision of molecules, (d) redistribution of energy level, and (e) change of molecular component by chemical reaction. However, the rapid or spontaneous emissions of photons are termed as LIF. The frequency of LIF signal can have different value from that of inducing laser beam.

Table 2.1 Formation and destruction of OH radical.

Fast OH formation by two-body reactions (1~5nsec)	
$H + O_2$	$\leftrightarrow OH + O$
$O + H_2$	$\leftrightarrow OH + H$
$H + HO_2$	$\leftrightarrow OH + OH$
Slow destruction by three-body recombination reactions (~20μsec)	
$H + OH + M$	$\leftrightarrow H_2O + M$

OH PLIF was used to obtain spatially and temporally resolved images of the reaction zone in various combustors. As described in Table 2.1, the OH radical concentration increases rapidly around the flame in about 20 μsec and then decomposes slowly in 1 to 5 ms by a 3-body recombination reaction [46]. Thus, near the flame front exists super-equilibrium OH. The OH radical, which is intermediate product of chemical reaction, has a concentration of more ten times than that of O or H radicals [47]. Therefore, the OH radical is found to emit more intensive fluorescence signal than other species when absorbing laser light. Hence, the fluorescence signal of OH radical is widely used as an indicator of flame front in reacting flows.

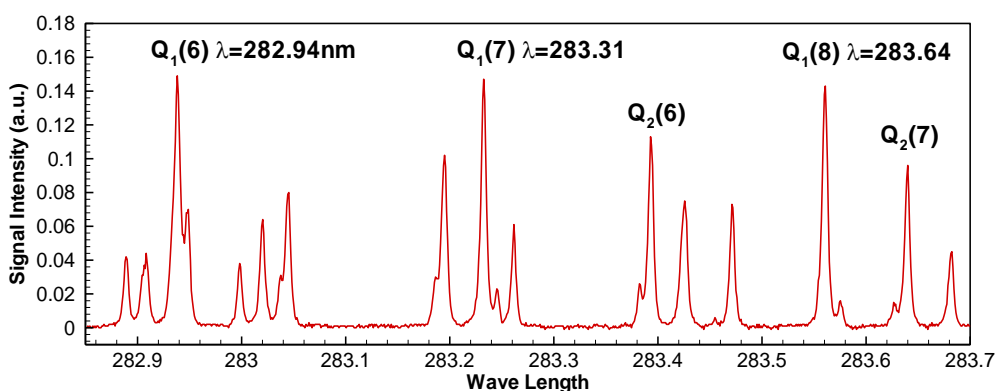


Fig. 2.4 OH excitation spectrum; In this study, $Q_1(6)$ was used for OH PLIF.

To observe the line positions for transition, we scanned the dye laser and recorded the signal at each step. We intended to use $Q_1(6)$ transition of the $A^2\Sigma^+ \leftarrow X^2\Pi$ ($v' = 1, v'' = 1$) band ($\lambda = 282.94$ nm) for the excitation wavelength and to collect the fluorescence signal from the $A-X$ (1, 0) and (0, 0) bands ($\lambda = 306 \sim 320$ nm). Using monochromator and photomultiplier tube (PMT), in conjunction with a test flame in laminar premixed condition, a laser excitation scan was performed over the range of interest from $\lambda = 282.5$ nm to $\lambda = 283.5$ nm with 0.001 nm step. The monochromator was fixed at 315 nm to collect the fluorescence. The signal was multiplied by PMT and recorded through the boxcar averager.

At every scanning step, 10 pulses of signal were recorded and averaged. After scanning the dye laser, the OH excitation spectrum can be obtained as shown in Fig 2.4. Among the peak values of excitation spectrum, we used $Q_1(6)$ as the excitation wavelength of OH radical.

When the location of $Q_1(6)$ line was detected, the fluorescence spectrum could be obtained by recording the LIF signal at each scanning step of the monochromator. Figure 2.5 is OH fluorescence spectrum graph for $Q_1(6)$. Peak value is found at 320nm.

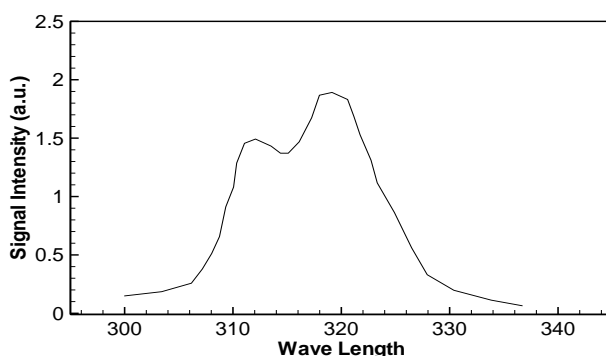


Fig. 2.5 OH fluorescence spectrum for $Q_1(6)$.

PLIF System

For OH PLIF, an Nd:YAG pumped dye laser was turned to $Q_1(6)$ transition of the $A^2\Sigma^+ \leftarrow X^2\Pi (v' = 1, v'' = 1)$ band ($\lambda = 282.94$ nm). $Q_1(6)$ transition line is generally used in the measurement of molecular concentration because it has large LIF signal and the dependency for temperature is low. Fluorescence from the $A-X (1, 0)$ and $(0, 0)$ bands ($\lambda = 306 \sim 320$ nm) were collected with a UV-Nikkor 105 mm/f 4.5 lens. Because UV light cannot penetrate the common glass, all the lenses should be made with quartz. The region of interest was focused onto the ICCD camera of Princeton Instrument (PI-MAX 1K). Two filters (WG-305 and UG-11) were used to block scattered signal lights. Transmittance of each filter is shown in Fig. 2.6. The schematic diagram of OH PLIF system which was used in this study is also shown in Fig. 2.7.

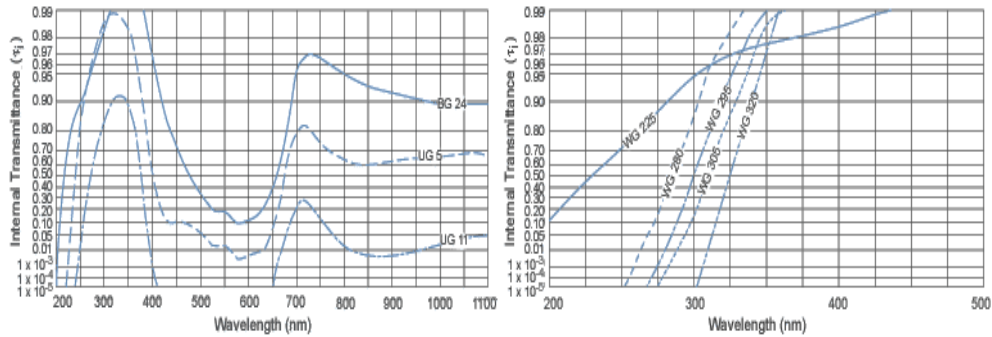


Fig. 2.6 Transmittance of filter (a) WG-305 (b) UG-11

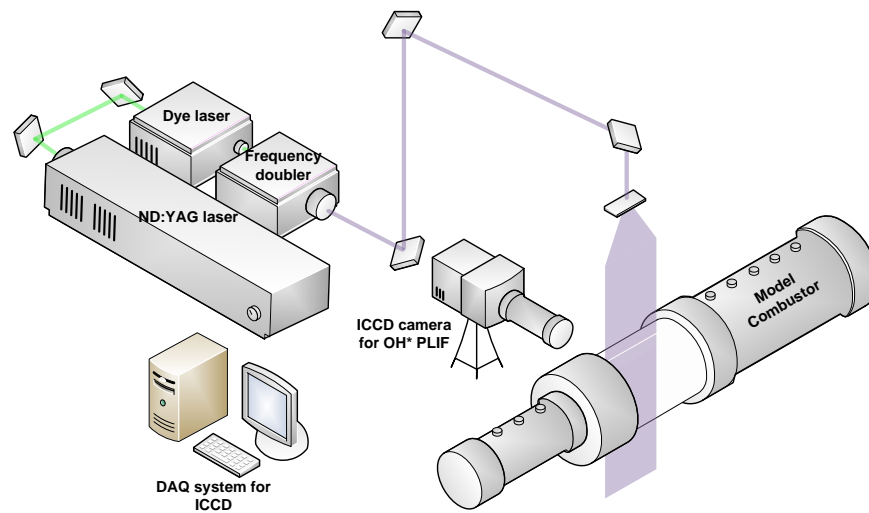


Fig. 2.7 Schematic diagram of OH-PLIF measurement system

High speed PLIF System

High speed laser measurement widely applied in various research field to find the unknown characteristics of high frequency phenomenon. Many research groups are conducting experimental approach about CH₄/Air flame, Liquid fuel flame and micro structure of the flame. The detailed information about the research are summarized in Table 2.2.

Table. 2.2 High-speed PLIF application research summary

Research Group	Year	Author	Contents	Rep. Rate
DLR	2013	M. Stohr	Simultaneous measurement of PIV & OH PLIF in CH ₄ swirling flame [48]	10kHz
DLR	2011	M. Stohr	Blow off characteristics of CH ₄ swirling flame [49]	5kHz
DLR	2010	I. Boxx	Simultaneous measurement of transient phenomena in a partially premixed swirl flame [16]	5kHz
CNRS	2012	P. Petersson	Simultaneous high-speed PIV & OH-PLIF about coaxial diffusion flame burner [50]	10kHz
CNRS	2014	P. Xavier	Cavity flame anchoring characteristics based on high-speed OH-PLIF [51]	10kHz
University of Cambridge	2011	J.R. Dawson	Near blow-off characteristics of bluff body stabilized CH ₄ flame [52]	5kHz
University of Cambridge	2012	N.A. Worth	Flame interaction of CH ₄ /air conical bluff-body stabilized flame [53]	5kHz
AFRL	2013	S. Hammack	Plasma-enhanced flame characteristics of turbulent non-premixed flame [54]	10kHz
Michigan University	2015	P.M. Allison	CH ₂ O-PLIF measurements in dual-swirl burner [20]	4kHz
Sydney University	2011	S. Meares	High-speed OH-PLIF imaging of extinction and re-ignition [55]	5kHz

In this study, the high harmonic instability frequencies were measured and the application of high-speed OH-PLIF is necessary to find the high frequency structural characteristics. High-speed OH-PLIF were set up at the rate of 7 kHz. The 7 kHz OH-PLIF used the laser beam from an Nd-YAG laser (Edgewave, IS-200-L) as the pumping source for the dye laser (Sirah, Credo-Dye-LG-24) and the OH fluorescence signal was measured by an intensifier (HS-IRO), a high speed camera (HSS8), a UV lens (f/2.8), and a bandpass filter (307±10 nm).

2.3.2. PIV Measurement

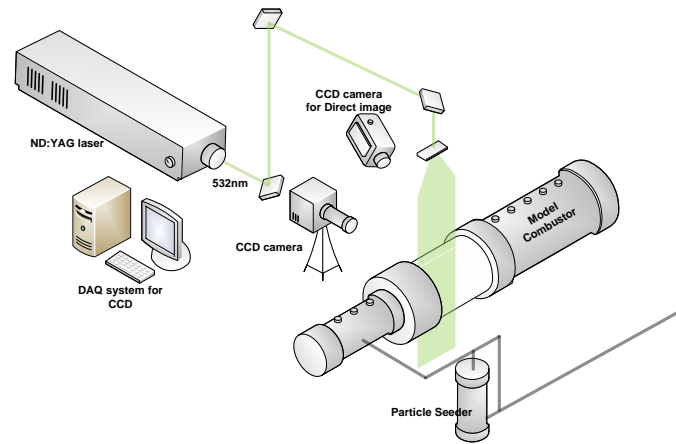


Fig. 2.8 Schematic diagram of PIV measurement system.

A particle image velocimetry (PIV) is the measurement technique, which obtains the velocity vector fields of a flow by comparing consecutive two images. The experimental set-up of PIV system consists of several sub-systems: light source system, detecting system, and particle seeding system as shown in Fig. 2.8. Small particles have to be seeded into flow to perform PIV technique because PIV measures only the velocity of particles by comparing the displacement of the particle images illuminated by the sequential light pulses, not the flow itself.

Generally, a double pulsed Nd-YAG laser is used as a light source and a high speed CCD camera is employed to obtain instantaneous particle images at a measurement plane. There are no specific rules for particle seeding system; however, the size of particle should be determined by considering whether particles can follow the flow well or not [56]. In most cases, it is necessary to add tracer particles into the flow. These particles are illuminated at the measurement plane of the flow at least twice times within a short interval. The light scattered or fluoresced by particle is recorded either on a single frame or on sequential frames. The displacement of the particle images recorded by the light pulses is calculated through evaluation of the PIV.

To calculate the displacement of the particles grabbed by a CCD camera, it is necessary to divide the image into a grid. The grid is called as an interrogation spot. After setting the interrogation spot size, one interrogation spot of the first images is picked and compared with all the interrogation spot of the second images. The displacement between the interrogation spot of the first image and the interrogation spot of the second image represents one vector of flow field. By conducting this work in all the interrogation spots, whole vectors of flow-field are obtained. This process is called as a correlation.

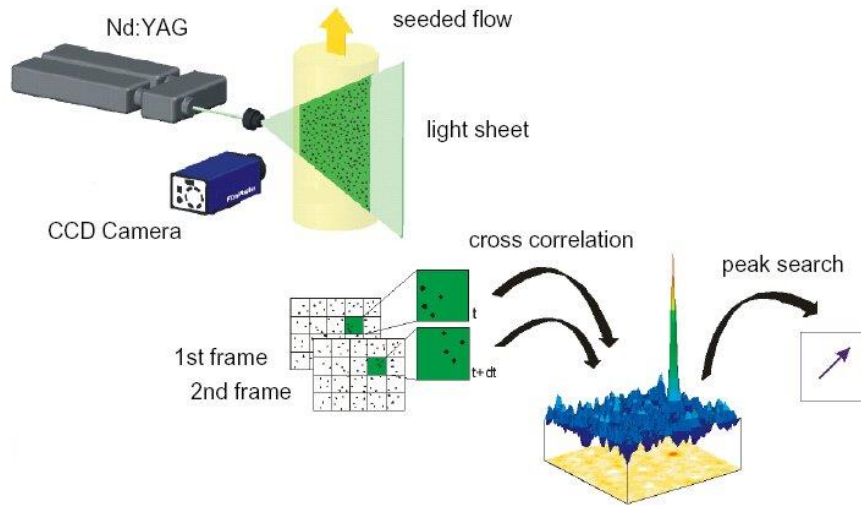


Fig. 2.9 Principle of typical PIV system.

The correlation function is expressed as follows:

$$h(s_x, s_y) = \int_0^{\infty} \int_0^{\infty} f(x, y)g(x + s_x, y + s_y)dx dy \quad (2.5)$$

The expression can become simple as conducting Fourier transformation for a convenience's sake in calculating. Here, F and G are Fourier transformed function of each

f and g , and they mean Fourier transform operator.

$$F(h) = F^*(f) \times F(g) \Rightarrow F^* \times F \quad (2.6)$$

$$h = F^{-1}(F^* \times G) \quad (2.7)$$

Equation 2.5 is the same expression of spatial masking in an image processing technique. Thus, it means that a correlation is a kind of masking concepts. According to this concept, the correlation can be called as a process to figure out distribution of the similarity by signal distribution in an image plane. Equation 2.7 makes us use fast Fourier transform (FFT) algorithm which reduces the calculation time drastically. The interrogation spot size of $2n \times 2n$ should be chosen to use FFT algorithm because FFT algorithm is a method by dividing even and odd terms. However, the calculation time becomes short by $\log_2 N/N$ times comparing with direct Fourier transform (DFT) algorithm.

A correlation method is separated into auto-correlation and cross-correlation by the number of functions. Mathematically, auto-correlation is the case; $f(x; y) = g(x; y)$ in Eq. 2.5 and cross-correlation is the case; $f(x; y) \neq g(x; y)$. Experimentally, an auto-correlation is used for the case where the first image at $t = t_1$ and the second image at $t = t_2$ are recorded in one frame (called as a single frame/double exposure mode) and cross-correlation is used for the case where the first image at $t = t_1$ and the second image at $t = t_2$ are recorded in separated frames (called as a double frame/single exposure mode). Comparing with an auto-correlation method, a cross-correlation method has some merits as follows:

1. Directional ambiguity problem can be avoided easily.
2. The algorithm is simple because there is only one peak as a result of correlation.
3. Dynamic range is relatively large.

However, it was difficult to satisfy hardware requirements for cross-correlation.

Specially, a time interval was a problem in most cases because the device, which satisfied both high resolution condition and short time interval (microsecond), was very expensive. Nowadays, it becomes relatively inexpensive and popular. Thus, most PIV systems use a cross-correlation method.

In this study, the scattering signal of seeding particles (ZrO_2 , $1\ \mu\text{m}$) from a sheet beam of the Nd-YAG laser (Continuum, Surelite-II) was measured using a CCD camera (Viewworks, VH-2MC-M42) mounted with a lens ($f/2.8$) and a band pass filter ($532\pm 10\ \text{nm}$). The field of view of the PIV and OH-PLIF was $65\text{mm}\times 75\text{mm}$. The time interval of the PIV was $3\ \mu\text{s}$, and 100 pairs of the instantaneous images were used to calculate the average velocity field. The interrogation spot size was 64×64 pixel, the overlap ratio was 50%, and Fast Fourier Transform-based cross correlation was applied for post-processing. Fig. 2.10 shows the field of view of PIV and OH-PLIF measurement.

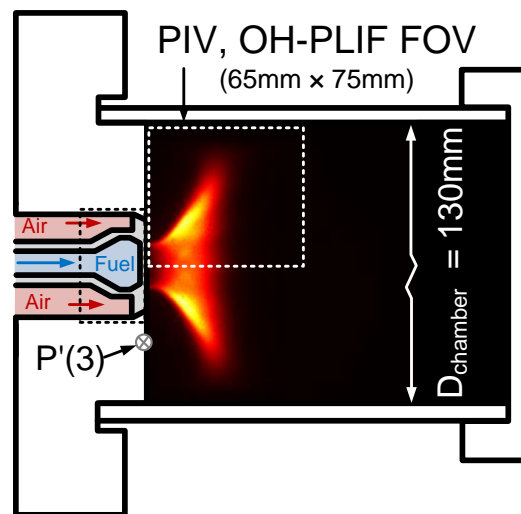


Fig. 2.10 Field of view of PIV and OH-PLIF measurement.

2.4 Continuous Wavelet Transform

The continuous wavelet transform was applied for dynamic pressure data analysis, which reveals the time and frequency domain characteristics. Most of the signals in experiments are time-domain signals in their raw format, meaning that the signals measured are a function of time. In many cases, particularly in combustion instability analysis, the most distinguished information is hidden in the frequency content of the signal.

There are many other transforms that are used quite often by engineers and mathematicians: Hilbert transform, short-time Fourier transform, radon transform, and wavelet transform. Every transformation technique has its own area of application with advantages and disadvantages. Fourier transform is probably the most popular transform for frequency domain analysis. In the 19th century, the French mathematician J. Fourier showed that any periodic function can be expressed as an infinite sum of periodic complex exponential functions. The Fourier transform gives the spectral content of the signal, but it gives no information regarding where those spectral components appear in time. Short-time Fourier transform is a method that can be applied to non-stationary signals. In short-time Fourier transform, the signal is divided into small enough segments, where these segments (portions) of the signal can be assumed to be stationary. For this purpose, a window function w is chosen. Narrow windows give good time resolution, but poor frequency resolution; for wide windows, the opposite is true. If the frequency components are well separated from each other in the original signal, some frequency resolution may then be sacrificed to obtain good time resolution, since the spectral components are already well separated from each other.

The wavelet transform solves to a certain extent the dilemma of resolution. The continuous wavelet transform was developed as an alternative approach to the short-time Fourier transform to overcome the resolution problem. The wavelet analysis is done in a similar way to the short-time Fourier transform analysis, in the sense that the signal is multiplied with a wavelet function that resembles the window function in the short-time Fourier transform. The transform is computed separately for different segments of the time

domain signal.

$$CWT_x^\psi(\tau, s) = \frac{1}{\sqrt{s}} \int x(t) \psi^* \left(\frac{t-\tau}{s} \right) dt \quad (2.8)$$

As seen in the above equation, the transformed signal is a function of two variables, τ and s , which represent the translation and scale parameters, respectively. $\psi(t)$ is the transforming function and is called the *mother wavelet*. If the signal has a spectral component that corresponds to the value of s , the product of the wavelet with the signal at the location where this spectral component exists gives a relatively large value. Continuous wavelet transform applied research examples include the understanding of the vibration occurrence in rotating device [57] and instability analysis during combustion [58]. In summary, it is widely applied in combustion research field in recent year [59-62].

Especially, combustion instability contains not only the frequency characteristics but also time-varying characteristics. Therefore, the application of continuous wavelet transform is an appropriate approach to understanding the instability characteristics that occurred in the model combustor. With the application of the continuous wavelet transform, selection of the proper wavelet is the most important factor for achieving accurate results.

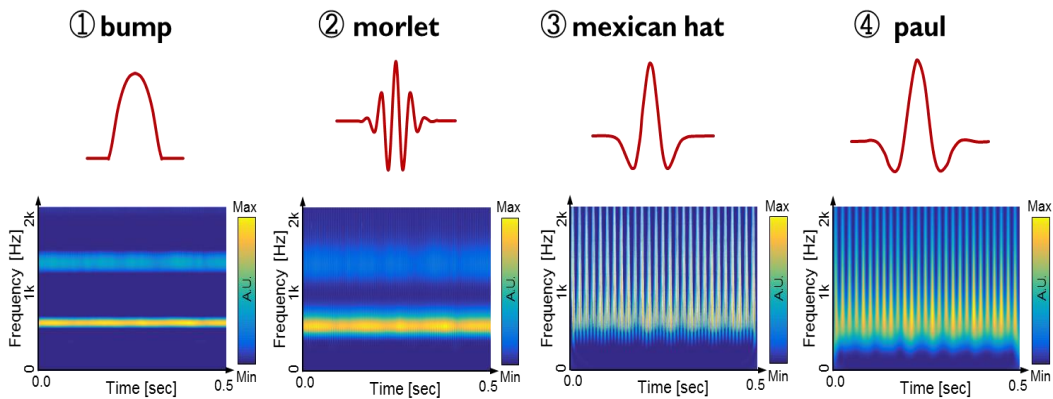


Fig. 2.11 Change of continuous wavelet transform results according to wavelet changes.

The 'bump', 'morlet', 'mexican hat' and 'paul' wavelet were compared by the same input data and the frequency analysis accuracies were compared as shown in the Fig. 2.11. The 'bump' wavelet shows the best frequency analysis resolution and it was selected as the wavelet of continuous wavelet transform application of this study.

2.5 Flame Transfer Function Measurement

A fuel flow rate modulation device (Siren), a PMT (Hamamatsu, H7732-10), and a hot wire anemometer (Dantec, MiniCTA) were used to measure the FTF. During FTF measurements, the input fluctuation was limited to up to 10% of the mean velocity. A plug nozzle was used to achieve the closed acoustic boundary in the instability tests. However, during the FTF measurements, the plug nozzle was removed to reduce the combustor geometry effects and make the combustor exit as an open boundary condition. Commonly, three kinds of modulation devices have been used during flame-transfer function measurement experiments: acoustic devices, the solenoid valve, and the siren. Previously modulation research (and the devices used) are summarized in Table 2.3.

Table 2.3 Summary of flow modulation device and application

Modulation device	Author	Contents
Speaker	C.O. Paschereit	Transfer matrices: 2002 [63]
Solenoid valve	A.X. Sengissen	LES: 2007 [64]
	S. Peter	Syngas FFT and CFD: 2007 [65]
Siren	K.T. Kim	FTF measurement, 2010 [37, 39, 40]
	W.S. Cheung	FTF measurement: 2003 [66]
	T. Sattelmayer	FTF measurement: 2004 [67]

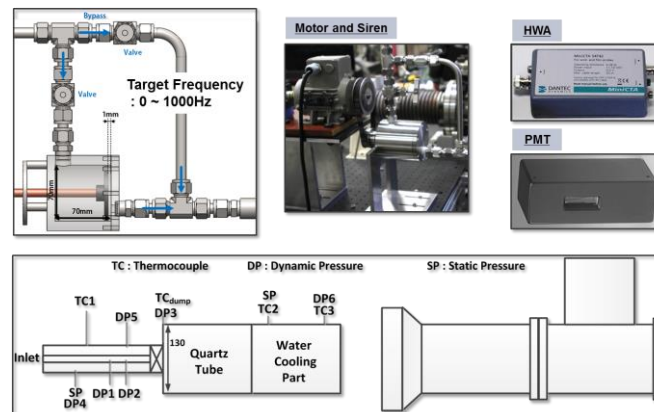


Fig. 2.12 Schematic diagram of the FTF measurement system.

The siren is a modulating device that rotates the disk; the area change of the flow path results in flow-rate modulation. The potential modulation frequency range of a solenoid valve is narrower than we expected and using a speaker at the increased inlet air temperature conditions under which our test was conducted is difficult. Therefore, the siren-type fuel modulation device was selected for this study. Additionally, in contrast with most previous research the fuel line was separately modulated to find the effect of the fuel flow-rate modulation effects on the flame characteristics. Therefore, for the fuel modulation tests, a siren-type fuel modulation device was installed upstream of the fuel inlet line. The modulation frequency of the siren can be varied up to 1100 Hz. Fig. 2.12 shows the FTF measurement system

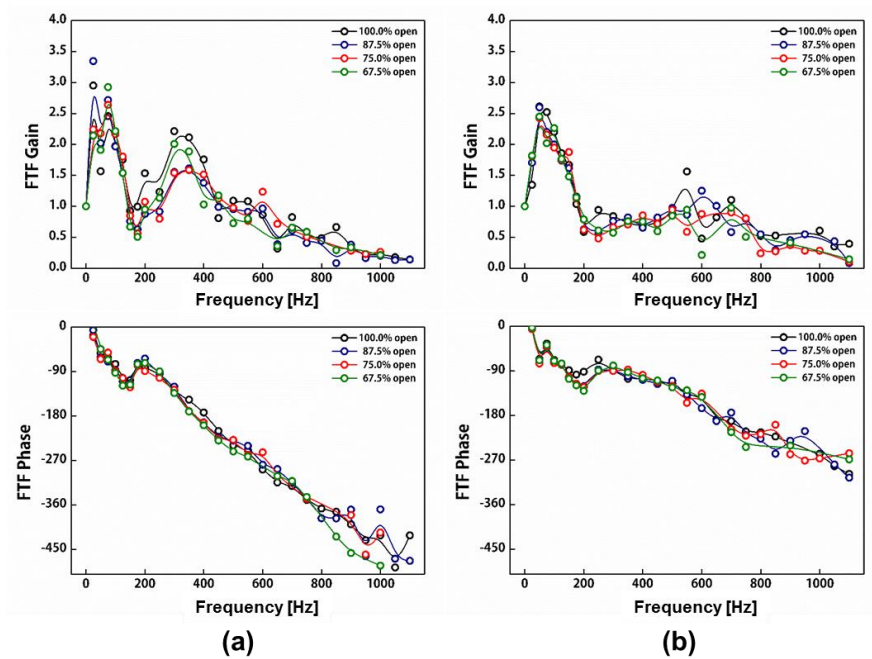


Fig. 2.13 Modulation amplitude effects on FTF characteristics (a) H₂ : CH₄ = 25 : 75, (b) H₂ : CH₄ = 50 : 50.

The fuel-modulation amplitude effects on the FTF characteristics were confirmed by the bypass ratio variation in Fig. 2.13. The bypass (shown in Fig. 2.12) was made to control the fuel fluctuation's amplitude. The bypass ratio, which is defined as the bypass flow rate divided by the siren incoming flow rate, was varied from 0% to 75%. Similar FTF gain and phase results occurred with variations of the bypass ratio; in our test condition, therefore, the effects of fuel-modulation amplitude were negligible.

In addition, Hot-wire anemometry was applied to measure the input variable (fuel-velocity fluctuation and heat release); the output variable was measured by PMT. Measurement data were recorded by the Labview-based data acquisition system, with a sampling rate was 25,000 samples/s.

2.6 Instability Prediction by 1D Lumped Network Model

In the case of a gas turbine, unstable combustion will adversely affect not only the combustor failure but also the downstream part [68], resulting in a disruption of the power supply system. Therefore, it is important to understand combustion instability characteristics in gas turbine combustor development. In particular, if the combustion instability phenomenon can be analyzed and predicted, it is possible to design a combustor that avoids the conditions in which the combustion instability phenomenon occurs in advance, or to effectively avoid the combustion instability condition that occurs during operation. In order to predict the combustion instability, various attempts have been made. The lower order model [69], the direct method (RANS, LES) [70], the linearized equations in time domain [71] and the Helmholtz solver [72] have been studied to predict the combustion instability. One example of the lower order model is the open source code, OSCILOS, based on the 1D lumped network method.

OSCILOS is a code developed by the A.S. Morgans in Imperial University to predict combustion instability in the frequency domain and time domain. The OSCILOS analysis was carried out through the CFD based flame transfer function and the combustor geometry information, and it was confirmed that the frequency prediction was successful [69].

OSCILOS analyzes the combustion instability by using combustor geometry information, thermal properties, flame location, and boundary conditions of the combustor. The flame transfer functions were measured by the experiments and the flame locations were also defined based on the flame visualization results. For the boundary condition, the analysis was performed by setting the inlet to the open boundary and the outlet to the closed boundary. Only the longitudinal acoustic waves of the 1D plane are considered, assuming that the radial perturbation is negligibly smaller than that of the acoustic waves. The combustion chamber is divided into modules and the continuity of each module boundary is considered as governing equation.

CHAPTER 3

COMBUSTION CHARACTERISTICS IN VARIOUS FUEL COMPOSITION

3.1 Objectives and Test Conditions

This study focused on the dynamic characteristic variations of fuel composition. Experiments, that investigate the effects of the fuel composition, were conducted using a partially premixed model gas turbine combustor, which is 1/3 scaled down from the GE7EA gas turbine. Fuel composition, heat input, inlet temperature and combustor length were selected as experimental variables and flame visualization was also conducted.

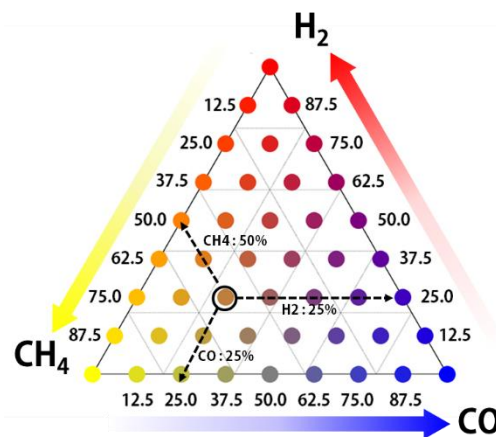


Fig. 3.1 Fuel composition sets for each load and inlet temperature test.

At first, the fuel composition tests were conducted under heated inlet air conditions to simulate the gas turbine inlet condition. The air mass flow rate was fixed at 1100 slpm and H₂, CH₄, and CO were selected as variables to study fuel flexibility. Fig. 3.1 shows 45 test conditions as a ternary diagram and each of the points shows a different fuel composition. For example, the black circled point in Fig. 3.1 shows the type of fuel that is composed of

25% H₂, 50% CH₄, and 25% CO. During the fuel composition tests, 40 kW heat input conditions were selected and the inlet air temperature also varied from 473K to 629K. The effect of combustor length variation on the combustion characteristics were also studied in 35, 40 and 45 kW heat input condition. The detailed test conditions of this chapter were summarized in the Table 3.1.

Table 3.1 Summary of the test conditions.

Parameters	Fuel composition variation	Combustor geometry variation	unit
Combustion chamber pressure	1.1 ~ 1.2		atm
Air flow rate	23.5		g/s
Air inlet temperature	473, 629	473	K
Air velocity (nozzle exit)	48		m/s
Fuel	H ₂ /CH ₄ /CO (45cases)	H ₂ /CH ₄ (9cases)	-
Reynolds number (air)	54,700		-
Lewis number	0.372 ~ 1.018		-
Heat input	40, 50	35, 40, 45	kW _{th}
Overall equivalence ratio	0.48 ~ 0.58		-
Combustor length	1410	1170 ~ 1410	mm
Swirl number	0.832		-

The purpose of this study was to investigate the effect of various test conditions on combustion instability characteristics in the combustion process. Fuel composition, air flow rate, and equivalence ratio were the main parameters during the combustion tests. The laminar flame velocity and the flame temperature used in the analysis of the experimental results were also calculated using an open source ‘Cantera’ program based on GRI3.0. Calculation of the Lewis number was performed for quantitative confirmation of test conditions. The Lewis number is defined as the ratio of thermal diffusivity to mass

diffusivity as shown in the following Equation 3.1, and it is a criterion for distinguishing combustion characteristics when the value of it is larger or smaller than 1.

$$Le = \frac{\alpha}{D} \quad (3.1)$$

Thermal diffusivity can be expressed as thermal conductivity (k), density (ρ) and specific heat capacity (C_p) as shown in Equation 3.2. The calculation of each parameters were performed based on GRI3.0 mechanism.

$$\alpha = \frac{k}{\rho C_p} \quad (3.2)$$

In the case of mass diffusivity, the hydrogen and methane diffusivity when they are respectively transferred to air was used. In addition, a literature survey was conducted to calculate the Lewis number for mixed fuel composition. The calculation of the effective Lewis number was performed through the linear proportional relation according to the fuel composition ratio as shown in Equation 3.3 [73].

$$Le_{eff} = x_1 Le_1 + x_2 Le_2 \quad (3.3)$$

The x_1 and x_2 are molar ratios for the each compositions, and Le_1 and Le_2 represent individually calculated Lewis number. In this experiment, the test was carried out during the variation of the H₂ to CH₄ ratio, and the effective Lewis number was calculated from the Lewis number of H₂ and CH₄.

Figure 3.2 reveals the calculated effective Lewis number of each test conditions. The Lewis number gradually decreases from 1 to 0.35 as the H₂ ratio increases in the fuel composition. In addition, for most test conditions, the Lewis number is less than 1, which

means that the mass diffusivity is relatively larger than the thermal diffusivity under the total test conditions.

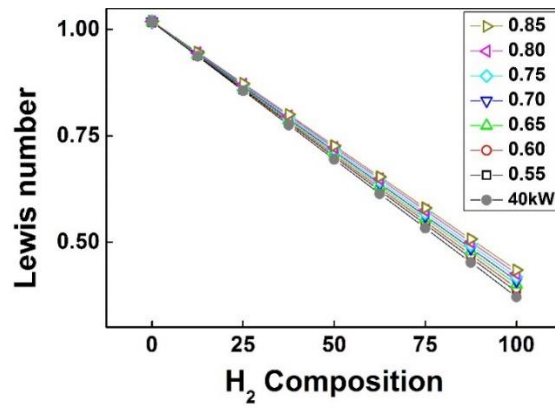


Fig. 3.2 Calculated Lewis number variation based on fuel composition change.

3.2 Combustion Instability Characteristics

3.2.1 Effects of heat input and inlet temperature variations

First, heat input, which can represent the power output variation of the gas turbine, was regarded as a variable and it was varied by two values, 40 kW and 50 kW. Fig. 3.3 shows the root mean square (RMS) amplitude of the 3rd dynamic pressure sensor that was measured during 1 second of each of the test conditions. Typically, in a land based gas turbine combustor, the combustion instability is defined as higher fluctuation of static pressure in the combustor that is greater than 5%; however, in this study 0.15 psi ($\approx 1\%$ of combustor pressure) was selected as the severe combustion instability criterion.

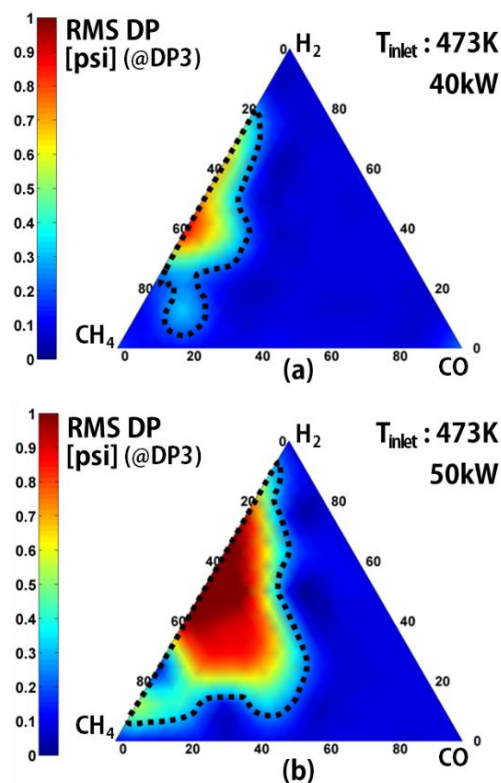


Fig. 3.3 Ternary diagram of the RMS dynamic pressure amplitude at the dump plane (a) 40 kW heat input, 473K inlet air temperature (b) 50 kW heat input, 473K inlet air temperature.

The instability region was mainly formed when the fuel composition consisted of H_2 and CH_4 and the increase in the CO concentration in the fuel has an effect on the decrease in the RMS dynamic pressure amplitude. In addition, at 50 kW, the heat input condition instability region and its amplitude increases, but the overall trend related to the fuel composition in the 50 kW heat input test was similar to the 40 kW heat input test result.

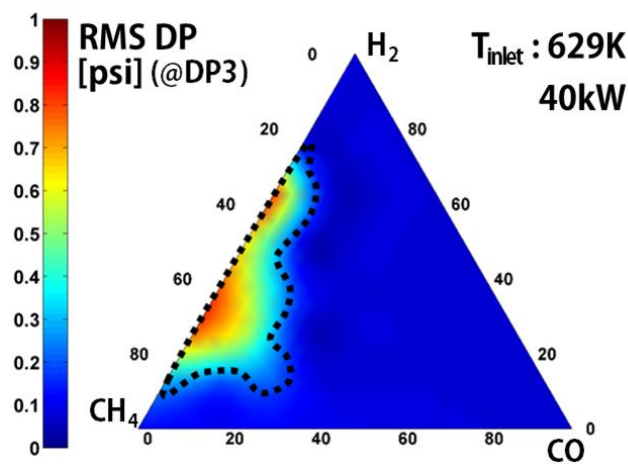


Fig. 3.4 Ternary diagram of the RMS dynamic pressure amplitude at the dump plane, 40 kW heat input, 629K inlet air temperature condition.

Second, the inlet temperature of the combustor, which can vary depending upon the chemical characteristics of the combustion, was selected as an experimental variable. Fig. 3.4 shows the RMS amplitude results of the 3rd dynamic pressure ($P'(3)$) sensor that was measured at the same point in both of the heat input variation tests. The 3rd dynamic pressure sensor located at the dump plane of the combustor. The inlet temperature variation does not have a significant effect on the instability region. However, the fuel composition of the instability region shifted to a higher CH_4 composition, which means that the inlet temperature affects the chemical properties of the combustion, such as the flame speed, the chemical reaction time, and the ignition delay. Consequently, this kind of variation affects the delay time of the combustion instability and it results in the instability region shifting

phenomenon.

From these experiments, the effects of variables, such as fuel composition, heat input, and inlet temperature, were found. In a practical approach, the fuel transfer process from CH_4 to syngas must exist at a commercial IGCC power plant. During the first step of the IGCC power plant operations, the fuel composition fluctuates and under that condition CH_4 is used to sustain the pilot flame. The fuel transition procedure must be performed in the low load condition because the increase of heat input results in the increase of instability possible region as shown in Fig. 3.3. In addition, the fuel transition procedure passes rapidly through the low CO composed gas to high CO composed gas, which is especially advantageous for suppressing combustion instability. In other words, the fuel transfer process must be considered in order to avoid the occurrence of combustion instability.

3.2.2 Classification of the instability conditions

To further study the combustion instability characteristics of various fuel compositions, the combustion instability frequency was classified into three regions. As mentioned above, the combustion instability criteria were selected based on the FFT magnitude of the dynamic pressure that was located at the dump plane (the 3rd dynamic pressure sensor). Fig. 3.5 shows the categorized instability regions at 473K and 627K and the inlet air temperature during the 40 kW heat input condition, as well as the RMS instability amplitude. Three kinds of instabilities were categorized and each of them was near 750 Hz, 1000 Hz, and 1500 Hz at the 40 kW, 473K inlet air temperature condition. However, 750 Hz instability was not found at the 629K inlet air temperature condition. This phenomenon can be related to the information presented in Fig. 3.3 and Fig. 3.4, which shows that the fuel composition of the instability region shifted to a higher composition of CH_4 . In summary, both the instability region and the instability frequency shifted based on the increase in the inlet temperature.

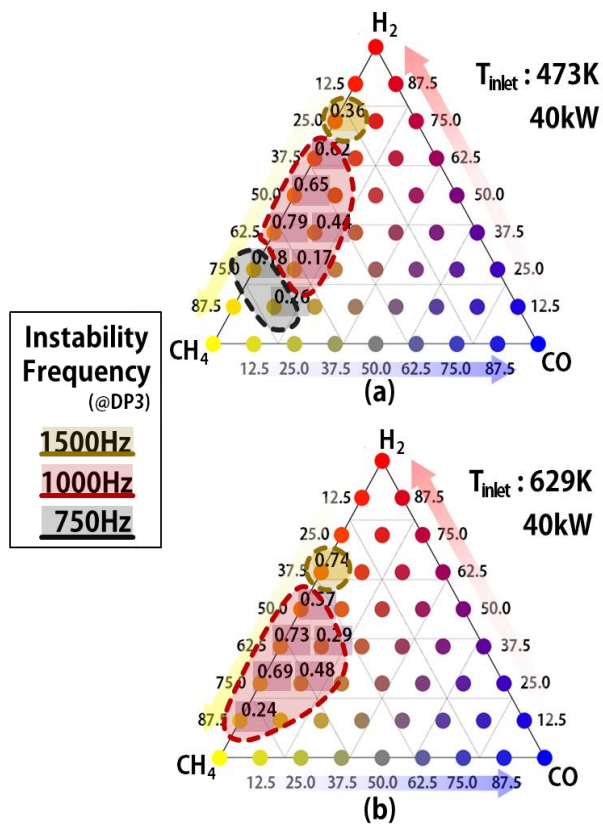


Fig. 3.5 Combustion instability frequency classification of the ternary stability map (a) 40 kW heat input, 473K inlet air temperature (b) 40 kW heat input, 629K inlet air temperature.

3.3 Instability analysis

3.3.1 Instability mode analysis

The general results of the instability frequency of the model gas turbine combustion test was lower than 500 Hz, which means it is associated with the first longitudinal mode of the combustor [74]. However, in this study, higher frequencies were measured and to determine the specific instability mode of the combustor, dynamic pressure-based mode analysis was conducted for three cases that are representatives of each of the instability regions. The selected conditions are summarized in Table 3.2.

Table 3.2. Representative conditions for classification of the mode analysis at 40 kW heat input, 473K inlet air temperature.

	Fuel composition [%]	Instability frequency [Hz]	Pressure amplitude [psi]	Temperature [K]
Case 1	H ₂ : 12.5 CH ₄ : 75.0 CO: 12.5	741	0.26	1195
Case 2	H ₂ : 37.5 CH ₄ : 62.0 CO: 0.0	1015	0.79	1178
Case 3	H ₂ : 75.0 CH ₄ : 25.0 CO: 0.0	1497	0.36	1188

For the mode analysis, the measured RMS dynamic pressure amplitude values are plotted based on the dynamic pressure sensor location. The estimated combustion instability modes were also plotted. The estimated combustion instability modes were calculated based on the boundary condition and the length of the combustor. As shown in Fig. 3.6, the measured RMS amplitude, which is depicted as dots, is located near the estimated mode. The result shows that Case 1 is the 3rd harmonic longitudinal mode, Case 2 is the 4th harmonic longitudinal mode, and Case 3 is the 6th harmonic longitudinal mode standing wave [75, 76].

In addition, the measured frequency and calculated frequency were compared for each

of the cases. The estimated frequency was also calculated based on the measured temperature, combustor length, estimated mode of each case, and acoustic theory. Table 3.3 shows the summarized results and it can be concluded that, in this combustor, higher mode instabilities occurred and the mode shifting phenomenon was also found in the H₂ concentration increasing condition.

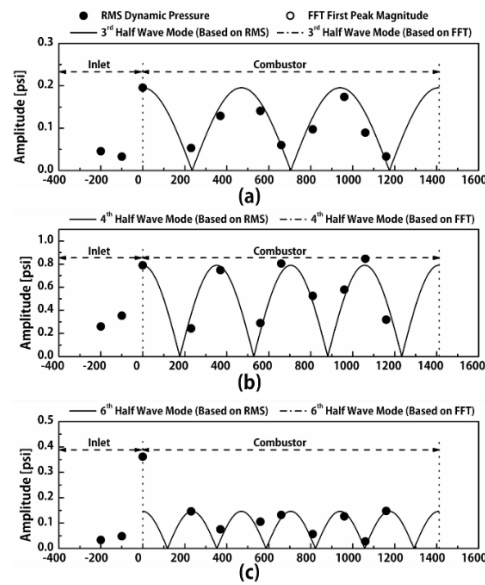


Fig. 3.6 Mode analysis based on the RMS pressure amplitude of each dynamic sensor location (a) case 1, 750 Hz instability (b) case 2, 1000 Hz instability (c) case 3, 1500 Hz instability.

Table 3.3 Measured and calculated frequency comparison of each representative instability case.

	Measured Frequency [Hz]	Calculated Frequency [Hz]	Estimated Mode
Case 1	741	737	3rd harmonic longitudinal mode
Case 2	1015	1038	4th harmonic longitudinal mode
Case 3	1497	1470	6th harmonic longitudinal mode

3.3.2 Flame structure analysis based on H₂ composition

Fig. 3.7 shows the direct OH-chemiluminescence images of the 40 kW heat input conditions for each fuel composition. The increase in the H₂ concentration of the fuel affects the flame speed of the combustor and it can be directly related to the length of the flame [19, 77]. Furthermore, flame distribution (flame length) can also affect the local intensity of the flame. This can be clearly seen by comparing the 100% CH₄ image and the 100% H₂ image. A similar tendency for the flame length variation was also found during all of the test conditions. In addition, the length of the flame increased as the equivalence ratio increased. The reason for this phenomenon is the increased fuel injection velocity. In other words, the flame forms at the stabilization point of the injection velocity and the flame speed, so the increased injection velocity results in an enlarged flame shape. However, the effect of the fuel flow rate is less than the effect of the fuel composition variation.

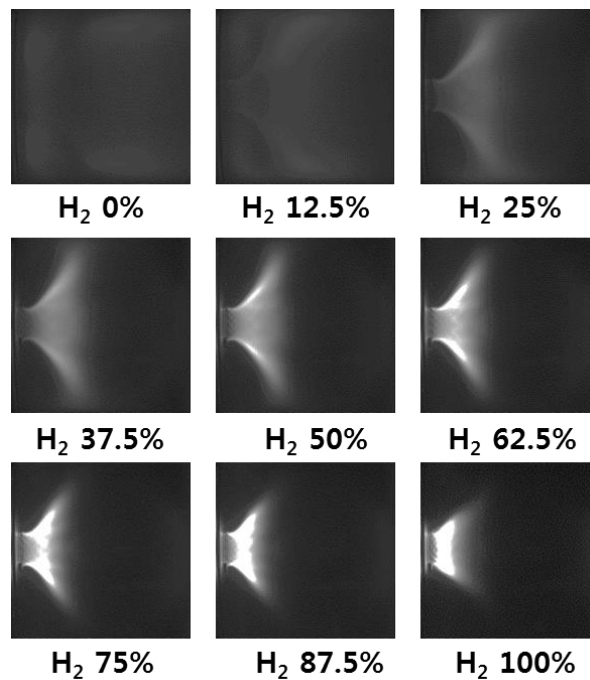


Fig 3.7 Averaged OH chemiluminescence images of each fuel composition at the 40 kW heat input and 473k inlet air temperature condition.

As mentioned experiment and measurement systems, the Abel inversion technique was applied to all of the test condition and Fig. 3.8 presents information on part of the results. Unlike the direct image obtained from the OH-chemiluminescence, the Abel inverted image shows that the OH radical signals are well-concentrated around the flame front. The length of the flame directly affects the convection time, which is important at the feedback loop of the combustion instability, and it was analyzed based on time-lag theory. The detailed analysis of the convection time will be concerned in the chapter 4.

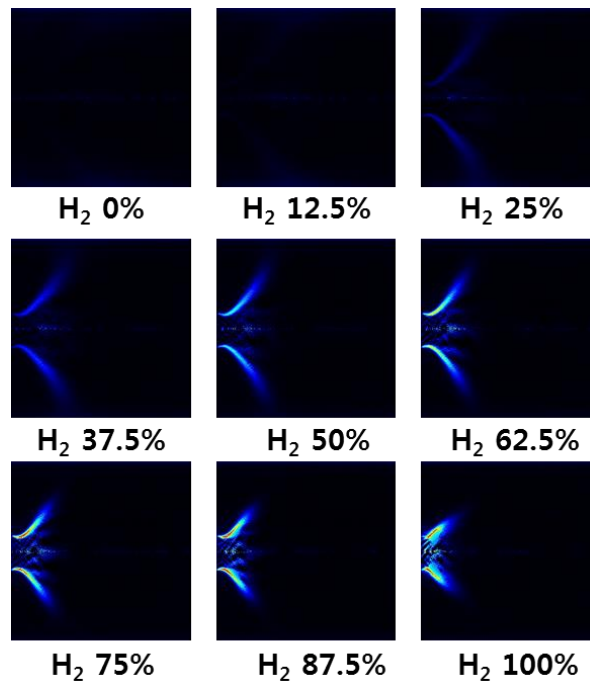


Fig 3.8 Abel inverted images of each fuel composition at the 40 kW heat input and 473k inlet air temperature condition.

The detail structure of the flame in some fuel compositions were investigated based on high speed OH-PLIF measurements. The CI characteristics of a fuel mixture with a composition that varied from pure CH₄ to pure H₂ by span of 12.5 vol% were examined at a constant heat input of 40 kW. As determined from a previous study [21], the main CI

frequencies were the 3rd ($\approx 750\text{Hz}$) and 4th ($\approx 1,000\text{Hz}$) harmonic mode; therefore a 7 kHz OH-PLIF was applied to investigate the flame characteristics and a 7 kHz repetition rate was selected to obtain approximately 10 images per CI cycle in the full resolution (1024×1024) of the CCD.

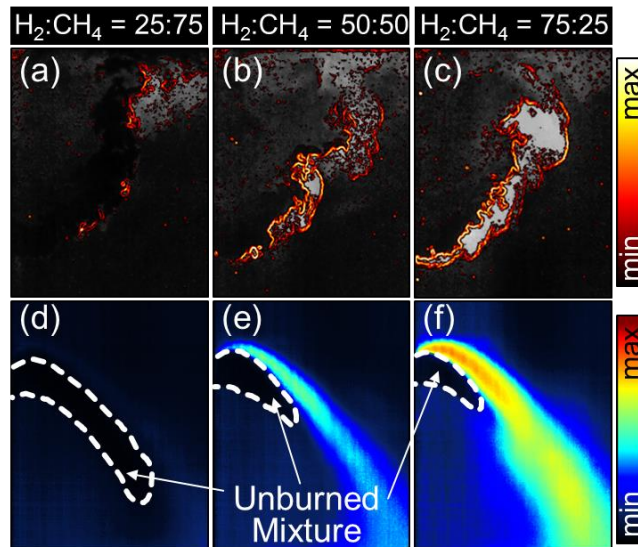


Fig. 3.9 Instantaneous flame edge (a) $\text{H}_2:\text{CH}_4 = 25:75$, (b) $\text{H}_2:\text{CH}_4 = 50:50$, (c) $\text{H}_2:\text{CH}_4 = 75:25$ and averaged flame (d) $\text{H}_2:\text{CH}_4 = 25:75$, (e) $\text{H}_2:\text{CH}_4 = 50:50$, (f) $\text{H}_2:\text{CH}_4 = 75:25$ measured by 7 kHz OH-PLIF.

Continuous time series images of the unstable flame were obtained and used to determine the flame boundary by calculating the gradients of the OH-radical distributions using the Sobel edge detection algorithm. Fig. 3.9(a)-(c) show the calculated instantaneous flame edge for H_2 percentages of 25%, 50%, and 75%. At the dump plane, the local blowout (also known as flame discontinuity) decreased during the increase in the H_2 composition of the fuel. Fig. 3.9d-f show the averaged OH-PLIF images of 7,000 instantaneous images, which indicate a tendency toward an increase in the intensity of the OH-radical as the H_2 fuel composition increased. The partially premixed model combustor characteristics

resulted in an unburned mixture region located just before the flame zone, and this region was defined as the no-radical region of the OH-PLIF image.

3.3.3 Dump plane temperature analysis based on the flame structure

The dump plane temperature was measured throughout the entire testing procedure and it is summarized in Fig. 3.10. The dump plane temperature of 40 kW, 473K inlet air temperature condition (Test 1) were plotted in Fig. 3.10a and 40 kW, 629K inlet air temperature condition (Test 2) were plotted in Fig. 3.10b. The x axis shows the experimental number, which means that each point is related with 45 ternary test conditions. For the stable condition, the dump temperature was almost constant for both Test 1 and Test 2. However, in the unstable condition, a dump plane temperature increasing tendency was found and the amount of the temperature variation amplitude was directly related to the dynamic pressure magnitude of the instability. To determine the reason for the dump plane temperature increasing tendency in the unstable condition, the flame structure was measured using a visualization technique, such as OH-chemiluminescence and OH-PLIF.

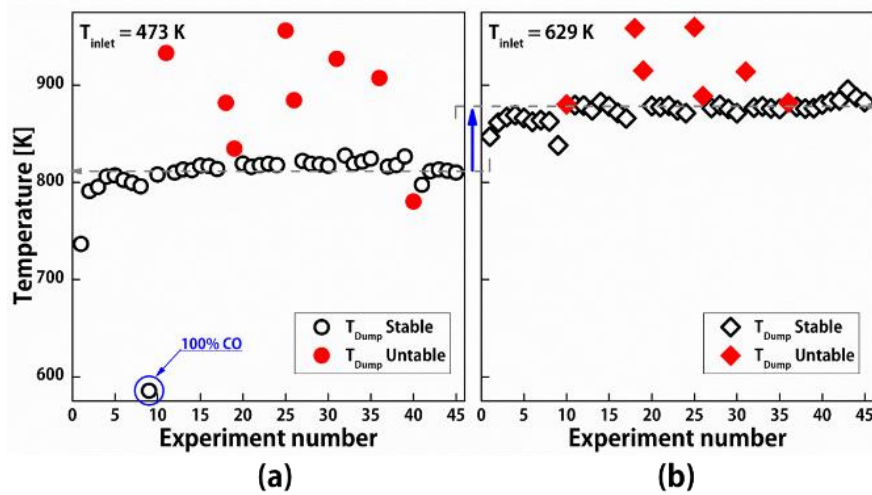


Fig. 3.10 Dump pane temperature fluctuation based on the combustion stability (a) 40 kW, 473K inlet air temperature (b) 40 kW, 629K inlet air temperature.

During the first step of this study, OH-chemiluminescence was recorded using a high speed ICCD camera at 12,500 frames per second to obtain more than 10 images at one cycle during the 1000 Hz instability condition. The tests were conducted under stable and unstable conditions. In the stable condition, the flame structure was steady. In addition, 100% H₂ showed a short flame and 100% CH₄ showed a broad flame, which can be explained based on the laminar flame speed of the fuel composition.

Fig. 3.11 shows the phase-averaged and the Abel-inverted unstable flame (= 1,000Hz) in the 40 kW, 473K inlet temperature condition. The measured dynamic pressure was used for the phase-resolved analysis and an Abel-inversion was applied to obtain a 2D cross section images from the OH-chemiluminescence images. Fig. 3.11 shows the structural variations of the flame during one cycle of the unstable condition, but the specific structures, such as the corner recirculation zone or vortex shedding, are difficult to figure out in the Abel-inverted OH-chemiluminescence images.

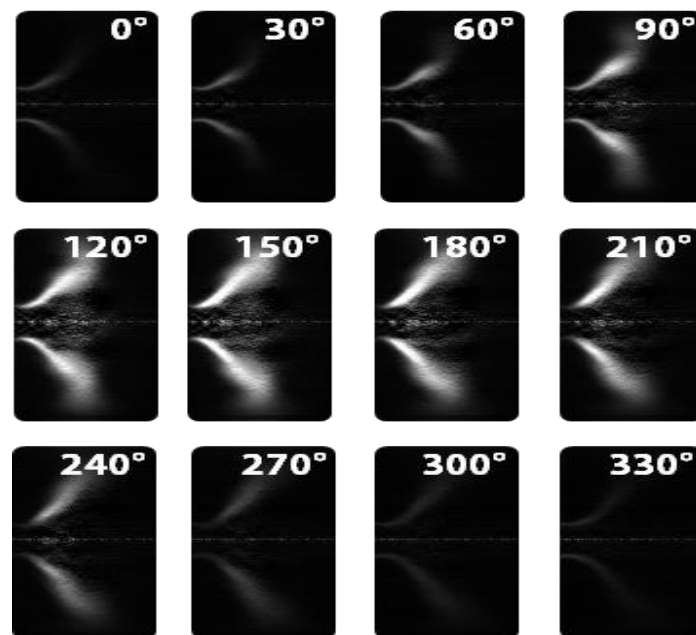


Fig. 3.11 Phase-averaged and Abel-inverted OH chemiluminescence image for the unstable condition near 1,000 Hz.

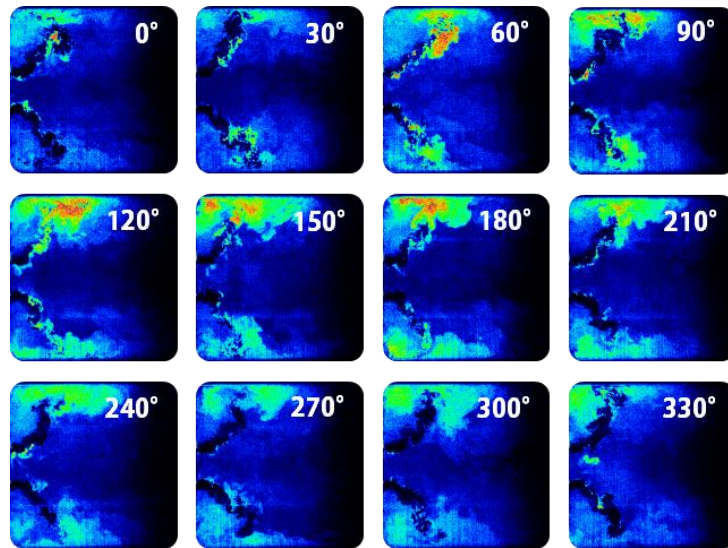


Fig. 3.12 Phase-resolved instantaneous OH-PLIF images, measured in the unstable condition.

To study the specific flame structures, OH-PLIF was conducted under the same unstable conditions and the phase-resolved analysis was also applied using the signal process of dynamic pressure, delay generator, and oscilloscope. Fig. 3.12 shows the instantaneous image of each of the phases, which were determined based on the 3rd dynamic pressure sensor ($P'(3)$) data that was located in the dump plane of the combustor. During the instability cycle, the size variation of the corner recirculation zone was obvious and ranged between 120–180 degrees. A large amount of the OH radical was formed at the dump plane.

From the structural analysis sequence of the unstable flame, which was conducted in this study, the increase in the dump plane temperature was the result of radical formations near the dump plane. It demonstrate that the relation between the dump plane temperature of the combustor and the dynamic pressure fluctuation can be used to indicate the structural variation of the flame.

3.3.4 Effects of combustor length on combustion instability

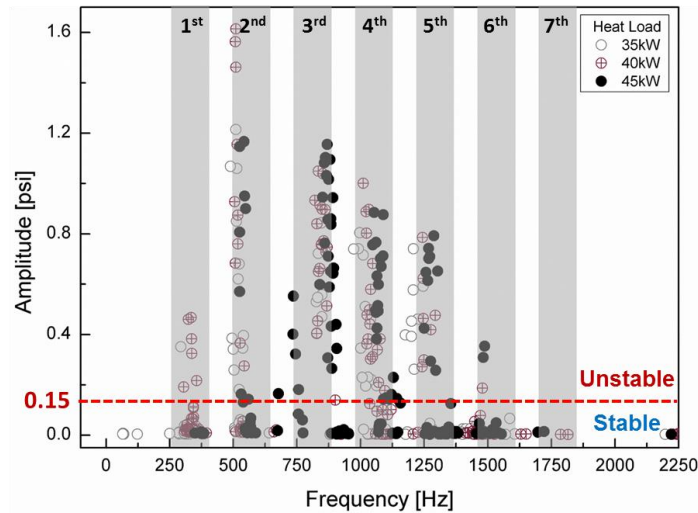


Fig. 3.13 Dynamic pressure amplitude and frequency plots in various fuel composition, heat load and combustor length.

The measured instability frequencies were found from 250 Hz to 1500 Hz; the diversity of the instability frequencies increased during the various test conditions as shown in Fig. 3.13. From these results, the occurrence of high harmonic combustion instabilities, which were found in mode analysis, was confirmed in the partially premixed model combustor. The occurrence of high harmonic instability is not the special event that can be found in various testing conditions. In addition, the increase or decrease of heat input is not directly related to the increasing or decreasing linear combustion instability trend, as can be seen by comparing the results of 40 kW with 35 kW and 45 kW. The increase of heat input is directly related to the increase of heat release fluctuation; however, the more important factor behind the occurrence or amplitude of instabilities is the degree of in-phase present between the heat release and the acoustic wave. To summarize, the instability phenomenon is a very complex event, and therefore cannot be easily correlated with one parameters (e.g., the increase in heat input). In other words, the phenomenon is not simply related to the possibility of instability with the equivalence ratio function.

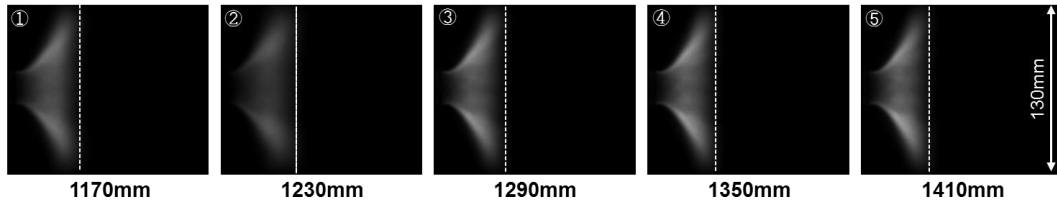


Fig. 3.14 Flame structure variation based on OH chemiluminescence during the combustor length variation at fixed $H_2:CH_4 = 37.5:62.5$ fuel composition and 40kW heat input.

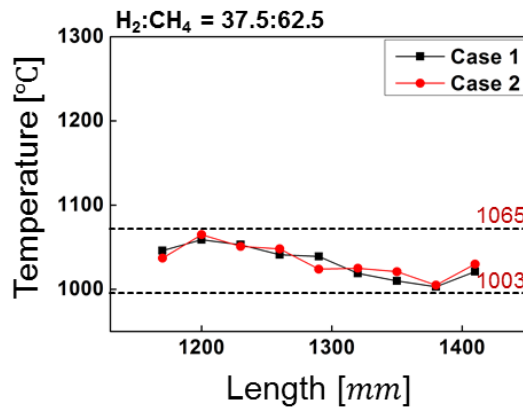


Fig. 3.15 Measured combustor temperature variation during the combustor length variation at fixed $H_2:CH_4 = 37.5:62.5$ fuel composition and 40kW heat input.

Fig. 3.14 reveals the OH-chemiluminescence flame images which were captured during the combustor length variation tests by ICCD camera. The flame structure did not affected by the combustor length variation. In addition, combustor temperature was also measured by thermocouple, which is located 470mm from the dump plane, during the combustor length variation. The temperature decreasing trend was found while the increase of the combustor length. The increased combustion volume results in the decrease of combustor temperature and the measured temperature range was from 1003 to 1065 °C. Based on the simplified acoustic equation, and measured combustor temperature

longitudinal fundamental mode frequency was calculated. The temperature variation of 62 °C results in the 5Hz variation of the fundamental frequency. But the 240mm length variation results in the frequency variation from 280 Hz to 347 Hz. In other words, the frequency variation of the instability is mainly influenced by the combustor geometry. The detailed research about the frequency during the combustor length variation was revealed in the Fig. 3.15.

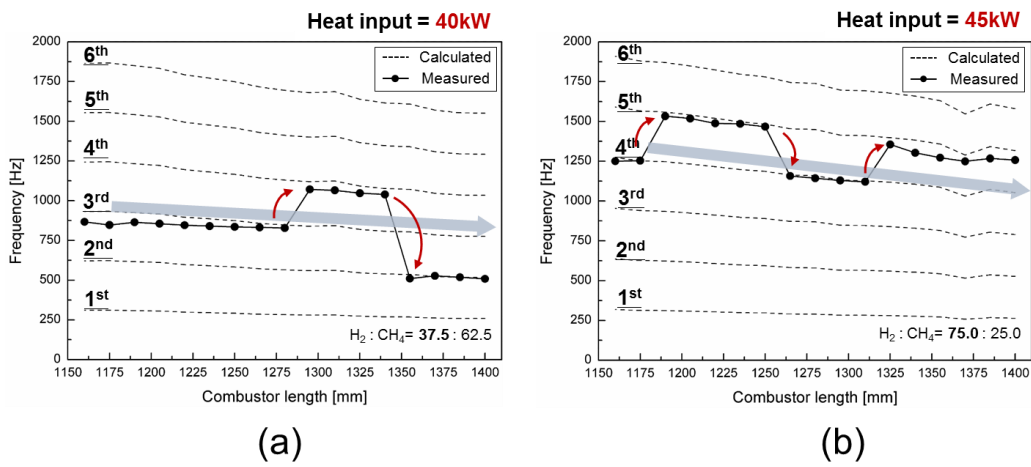


Fig. 3.16 Instability frequency and mode shifting results while the variation of the combustor length from 1170mm to 1410mm (a) 40kW, $H_2:CH_4 = 37.5:62.5$, (b) 45kW, $H_2:CH_4 = 75.0:25.0$.

Fig. 3.16 shows the effects of the combustor length variation in the combustion instability peak frequency variation. The dump plane–located dynamic pressure data were analyzed in the frequency domain and the peak amplitude occurring frequencies shown as the black dots in Fig. 3.16. The dotted line shows the estimated instability frequencies based on the measured combustor temperature.

$$f = \frac{c \cdot n}{2L_c} \quad (3.4)$$

As shown in Equation 3.4, the calculated instability frequencies were calculated based on the L_c (= combustor length), c (= speed of sound) and n (= mode number). The speed of sound was calculated based on the measured combustor temperature based on thermocouple which located in the 470mm apart from dump plane. The increase of combustor length directly affects the fundamental frequency (as was mentioned in the previous paragraph). The fundamental instability frequency gradually decreased as shown in Fig. 16. With a heat input of 40 W and $H_2:CH_4 = 37.5:62.5$, as shown in Fig. 3.16(a), 3rd mode instability mainly occurred with a combustor length of 1170 mm, but the instability mode shifts from the 3rd to the 4th mode with increases of the combustor length. In the detailed view shown by Fig. 3.16(a), the instability mode starts from the 3rd mode and shifts to the 4th mode before decreasing to the 2nd mode with variable combustor lengths. Instability frequency variation trends were also found with the 45-kW heat input and $H_2:CH_4 = 75.0:25.0$ test condition results (see Fig. 3.16(b)). The instability mode occurs in the 4th mode, shifting to the 5th mode before returning to the original mode, then reaching the 5th mode again with increases in the length of the combustor.

From the various tests results, the instability mode shifting phenomenon was not a unique event (or a set of unique events) occurring under special conditions, but rather occurred with variations in fuel composition, heat input, and combustor length. Therefore, the reasons for instability mode shifting were selected as the main topic of this study and will be discussed in the upcoming chapters. Additionally, the reasons for the occurrence of multi-mode instability which can be easily found in higher harmonic instability condition were also analyzed in Chapter 4.

CHAPTER 4

HIGH HARMONIC INSTABILITY CHARACTERISTICS

4.1 Objectives and Test Conditions

The reason of the instability mode shifting and multi-mode instability occurrence was investigated in this chapter. The new aspects of the work presented in this part are outlined below. First, the fuel composition, airflow rate, and equivalence ratio (ϕ), variables that can change the convection time (τ_{conv}), were selected, and the relationship between FMS was verified in a partially premixed model combustor. The global convection time ($\tau_{\text{conv_global}}$) was calculated based on the OH-PLIF and the fuel injection velocity. The flame length or center is normally used for the τ_{conv} calculation [21, 78]; however, the unburned mixture length was used in this research to satisfy the definition of the τ_{conv} in partially premixed combustor. The real convection time ($\tau_{\text{conv_real}}$) was also calculated from the particle-image velocimetry (PIV) measurement, and it was well matched with the $\tau_{\text{conv_global}}$ variation trend. Second, the time and frequency domain based quantitative analysis was conducted to determine the characteristics of multi-mode instability. In addition, the continuous wavelet transform was applied to obtain the frequency varying information. From the analysis, two kinds of multi-mode instability were identified: co-existence instability and intermittent instability. Finally, the cause of multi-mode instability was deduced based on the τ_{conv} calculation.

Table 4.1 shows the summarized test conditions which were conducted in this chapter. The combustor length was fixed at 1,410 mm during the tests to simplify the instability analysis process. The fuel composition (H_2 and CH_4 , 0–100% by volume flow rate, span = 12.5% at the fixed heat input of 40 kW), air volume flow rate (825–1,375 slpm, span = 137.5 slpm at a fixed equivalence ratio = 0.56), and equivalence ratio (0.55–0.80, span = 0.05 at a fixed air volume flow rate = 1,100 slpm) was selected as the variable. The dynamic

pressure data of previously mentioned test conditions were also used for the categorization and analysis of multi-mode instability characteristics.

Table 4.1 High harmonic instability test conditions.

Parameters	Basic condition	Airflow rate	Equivalence ratio	unit
Combustion chamber pressure	1.1 ~ 1.2			atm
Air flow rate	23.5	17.8 ~ 29.6	23.5	g/s
Air inlet temperature	200			°C
Air velocity (nozzle exit)	48	35 ~ 60	48	m/s
Fuel	H ₂ /CH ₄ (9 cases)			-
Reynolds number (air)	54,700	39,800 ~ 68,300	54,700	-
Lewis number	0.372 ~ 1.018			-
Heat input	40	30 ~ 50	38 ~ 71	kW _{th}
Overall equivalence ratio	0.48 ~ 0.58	0.56	0.55 ~ 0.85	-
Combustor length	1410			mm
Swirl number	0.832			-

The laminar flame velocity and the adiabatic flame temperature for all test conditions were calculated by ‘Cantera’ program which based on GRI3.0 mechanism. The equivalence ratio was changed from 0.55 to 0.85 at 0.05 intervals and the fuel composition was changed from pure CH₄ to pure H₂ to 12.5% intervals. The calculation of the adiabatic flame temperature for each condition was performed as shown in Fig. 4.1 As shown in Fig. 4.1(a), it can be seen that the adiabatic flame temperature increases linearly with the increase of the equivalence ratio in the same fuel composition. In addition, when the H₂ ratio increases at the same equivalent ratio, the adiabatic flame temperature nonlinearly increases and it can be confirmed that the increase in the H₂ content rapidly increases the adiabatic flame temperature. Fig. 4.1(b) summarize the changes in laminar flame velocity over the entire test conditions. The increase of the equivalence ratio under the same fuel composition

results in a linear increase of laminar flame velocity, and the change in the fuel composition at the same equivalent ratio causes a change in the nonlinear laminar flame speed. The calculated chemical properties were used to find the characteristics of test conditions and it will be also applied to understand the high harmonic instability characteristics.

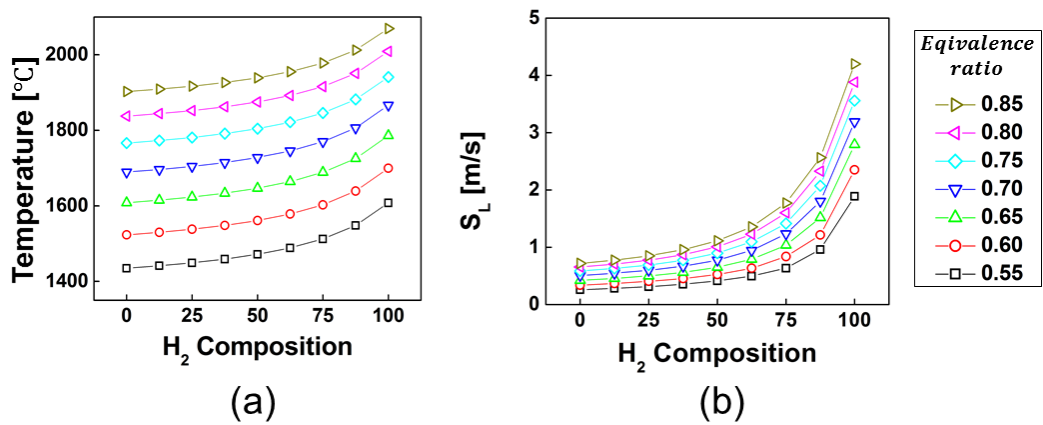


Fig. 4.1 Calculated chemical properties based on GRI 3.0 mechanism (a) adiabatic flame temperature (b) laminar flame speed.

4.2 Instability Mode Shifting

The combustion instability characteristics of a fuel mixture with a composition that varied from pure CH₄ to pure H₂ by a span of 12.5 vol% were examined at a constant heat input of 40 kW. The combustion instability characteristics were examined by measuring P'(3) while varying the H₂ composition. The eigenfrequencies of the longitudinal modes were calculated as 250 Hz at the fundamental mode and n-multiples of 250 Hz at the nth modes, by assuming that the tested combustion chamber was filled with hot gas at 1,000 °C and acoustically bounded with the dump plane at the upstream and the plug nozzle at the downstream.

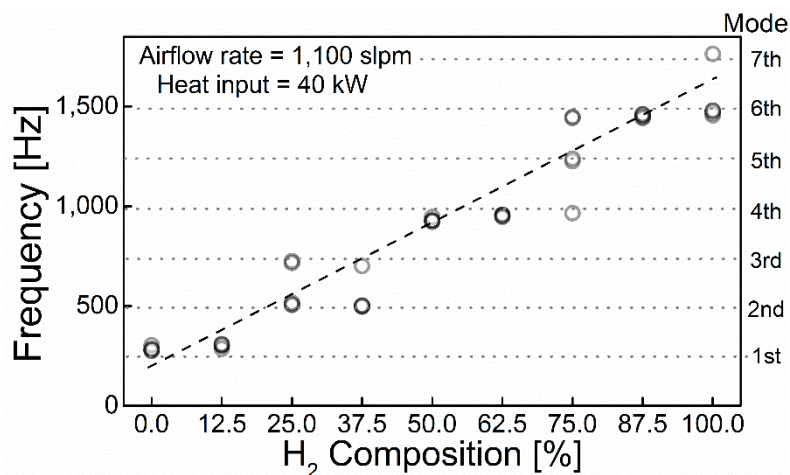


Fig. 4.2 FMS tendency during fuel composition variations.

As clearly shown in Fig. 4.2, the frequency and mode shifted from 250 Hz at the 1st mode to 1,750 Hz at the 7th mode as H₂ increased from 0% to 100%. This FMS has also been observed in a premixed combustor by Lieuwen [7], who reported that the inlet mixture velocity is the key parameter in determining the occurrence of FMS. In contrast to that previous study, FMS was observed in the present study when adjusting the fuel composition, and especially H₂, where the composition was linearly proportional to the combustion

instability mode as well as the frequency. This H_2 dependency on the combustion instability frequency has been previously investigated by Lee [21], who indicated that the τ_{conv} of the mixture flow from the fuel injector to the flame is the most vital factor and that the skewness time also becomes more significant as the intensity of the high harmonic mode increases.

The present study expanded upon Lee's study by conducting a τ_{conv} variation test to verify whether τ_{conv} is the main triggering source of FMS and to clarify the detailed mechanism underlying FMS.

4.2.1. Variable Effects in Instability Mode Shifting

The airflow rate at a constant ϕ and the ϕ modulated by the fuel flow rate at a constant airflow rate were selected as test parameters to understand the τ_{conv} effect on FMS. The airflow rate was varied from 825 slpm to 1,375 slpm (span=137.5 slpm) at a constant ϕ of 0.56, and 10 Hz OH-PLIF were applied for experimental measurement of the flame shapes.

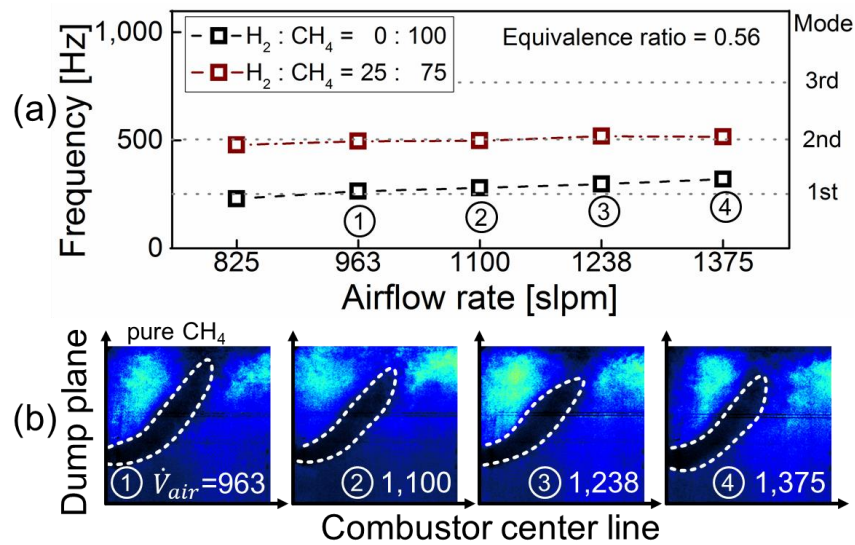


Fig. 4.3 (a) Instability frequency and (b) Averaged OH-PLIF images according to the airflow rate at $\phi=0.56$.

Fig. 4.3 shows the peak frequency of the $P'(3)$ depicted in Fig. 2.2 and the corresponding averaged OH-PLIF images. Both flames show a slight increase in the combustion instability frequency with an increasing airflow rate, whereas the combustion instability mode remained constant at the 1st and 2nd modes. Thus, the increased airflow rate and fixed ϕ will result in an increase in the heat input, so that the reason for the slightly increasing tendency of the combustion instability frequency was the increase in the combustor temperature. However, even a 43% increase in airflow rate was not sufficient to trigger the mode shift for both flames, whereas only a 25% increase in H_2 in the CH_4 based fuel shifted the combustion instability mode from the 1st to the 2nd mode. As shown in Fig. 4.3(b), the flame shapes do not vary significantly in response to airflow rate variations, so the τ_{conv} is considered to be almost the same.

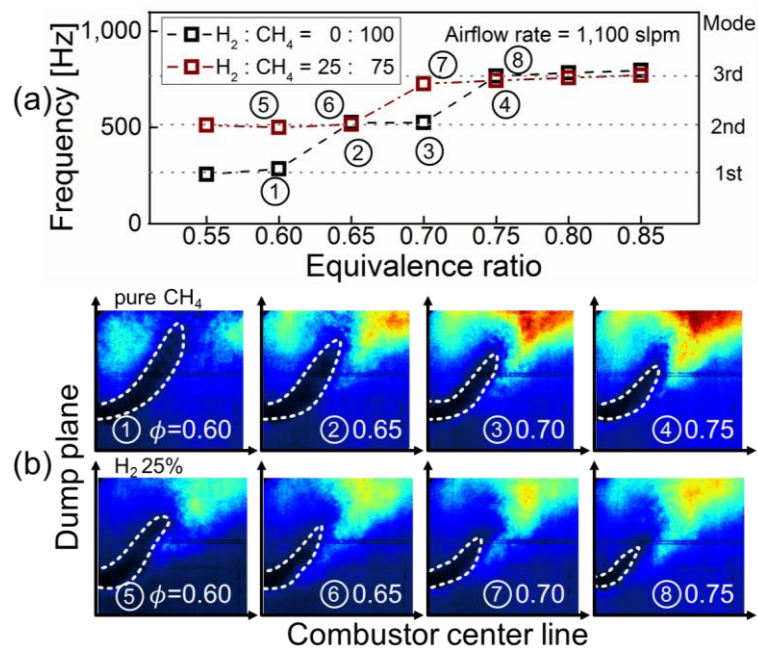


Fig. 4.4 (a) Instability frequency and (b) Averaged OH-PLIF images according to ϕ at a $\dot{V}_{air}=1,100$ slpm.

The effects of ϕ on the FMS characteristics were also investigated at a constant airflow rate of 1,100 slpm. In contrast to the test results of airflow rate variation, the variation of ϕ considerably changed the flame shape, as well as the mode and frequency of CI. An increase in ϕ at the same airflow rate resulted in a decrease in the flame length, as the increased ϕ attracted the flame closer to the dump plane due to the large increase in the burning velocity compared to the small increase in the unburned mixture velocity. In addition, the τ_{conv} that the unburned mixture delivered to the flame is mainly influenced by the fuel flow rate rather than airflow rate in the partially premixed combustor. Since the fuel injected from the same area nozzle and the increase of the fuel volume flow rate result in an increased injection velocity, a drastic reduction in the τ_{conv} is expected during the increase of the ϕ , which affects the FMS from the fundamental mode to the 3rd mode in the pure CH₄ condition, as shown at Fig. 4.4. A similar FMS from the 2nd mode to the 3rd mode was also found for the 25% H₂ fuel composition, shown as a red line in Fig. 4.4(a). Similar to this study, the ϕ dependency on the FMS has been previously reported by Shanbhogue [24].

Based on these results obtained by varying airflow rate and the ϕ , which affected the τ_{conv} in different ways, the conclusion can be drawn that the reduction in the τ_{conv} , which is mostly influenced by the fuel composition and ϕ , resulted in a shift in the combustion instability mode to a higher harmonic order of the longitudinal mode.

4.2.2. Convection Time Approach

As shown in Fig. 4.5(a), for conventional premixed type gas turbine combustors, variations in the length of the flame do not have a large effect on the τ_{conv} . However, when the mixing length is 2.7 mm, such as in the partially premixed type combustor used in the present experiment shown in Fig. 4.5(b), the change in the flame length has a major effect on the τ_{conv} . Therefore, the flame structure is changed by the combination of the fuel injection velocity and flame speed. When the flame length is shortened, the increase in the proportion of H₂ reduces the τ_{conv} . That is, in partially premixed type of combustors, the

flame length has a major influence on changes in the τ_{conv} caused by a short mixing length; due to that influence, a shorter feedback loop is built. Therefore, the τ_{conv} is mainly influenced by flame structure in partially premixed combustor, because of the ratio of mixing length and flame structure. Therefore we are trying to calculate the convection time and analyze its trend in relation to the instability FMS phenomenon.

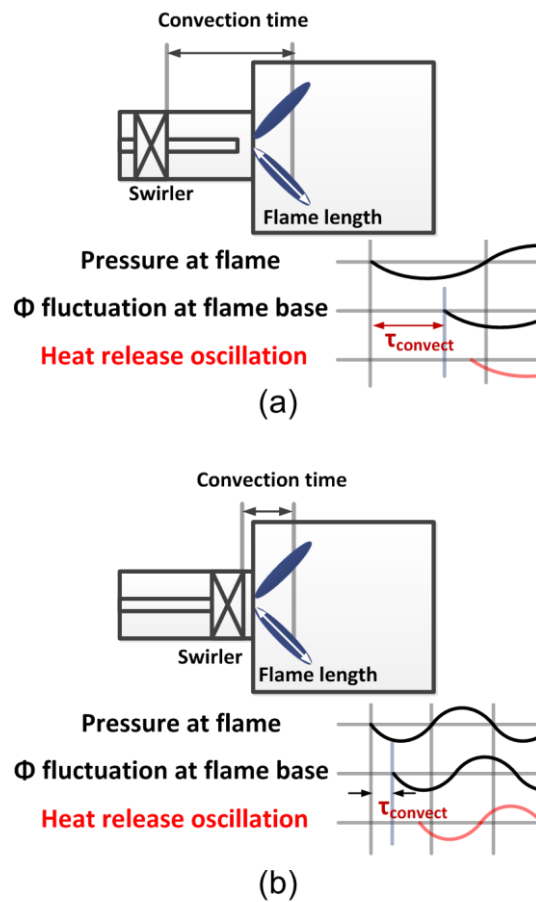


Fig. 4.5 Mixing length and convection time differences for the mixing type of the combustor based on time-lag analysis: (a) premixed combustor and (b) partially premixed combustor.

The effect of τ_{conv} was investigated quantitatively by calculating the real value of the τ_{conv_global} based on the flame images of OH-PLIF and using equation 4.1.

$$\tau_{conv_global} = \frac{L_{ub}}{U_e} \quad (4.1)$$

The L_{ub} [m] is the length of the convective path in the unburned mixture region where the no OH radical appeared in the OH-PLIF images, as displayed in Fig. 3.9(d)–(f), whereas U_e [m/s] is the simplified mean exit velocity at the fuel nozzle, calculated from the fuel flow rate divided by the nozzle exit area.

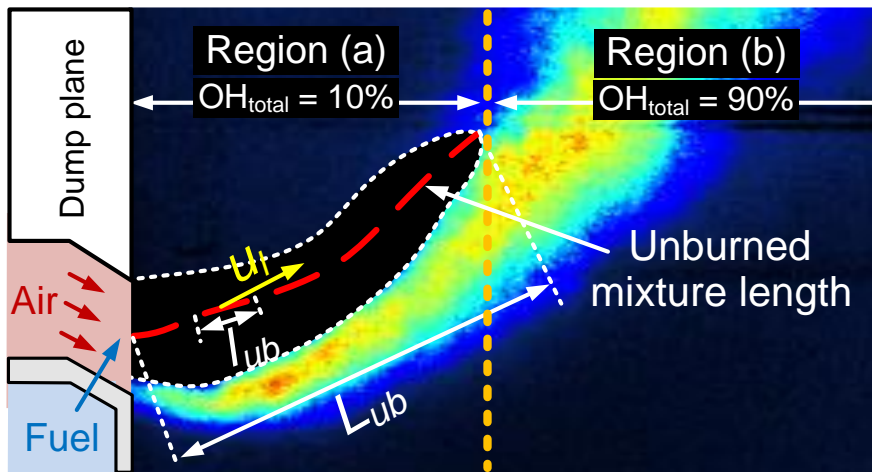


Fig. 4.6 Schematic flame structure and the unburned mixture length.

While determining the unburned mixture length, the intense OH radical area was measured between the dump plane and the end of the unburned mixture region shown in Fig. 4.6. The ratio of the 3D-integrated OH signal between region (a) and region (b) in Fig. 4.6 was 10%:90%. In other words, the majority of the OH radical formed at region (b). In Fig. 4.6, the fuel injection concept of this study was similar to the jet in cross-type combustion. By comparing the flame structures with the previous study of jet in cross-type

combustion [79, 80], the increased H₂ composition in the fuel makes the flame propagate to the injection points and the unburned mixture region beside the flame, as shown at Fig. 4.6. Therefore, the simplified flame structure was defined, as shown in Fig. 4.6, and it is similar with previous findings [80]. Based on the flame structure, the L_{ub} was defined from the dump plane to the end of the unburned mixture length based on the OH-radical intensity.

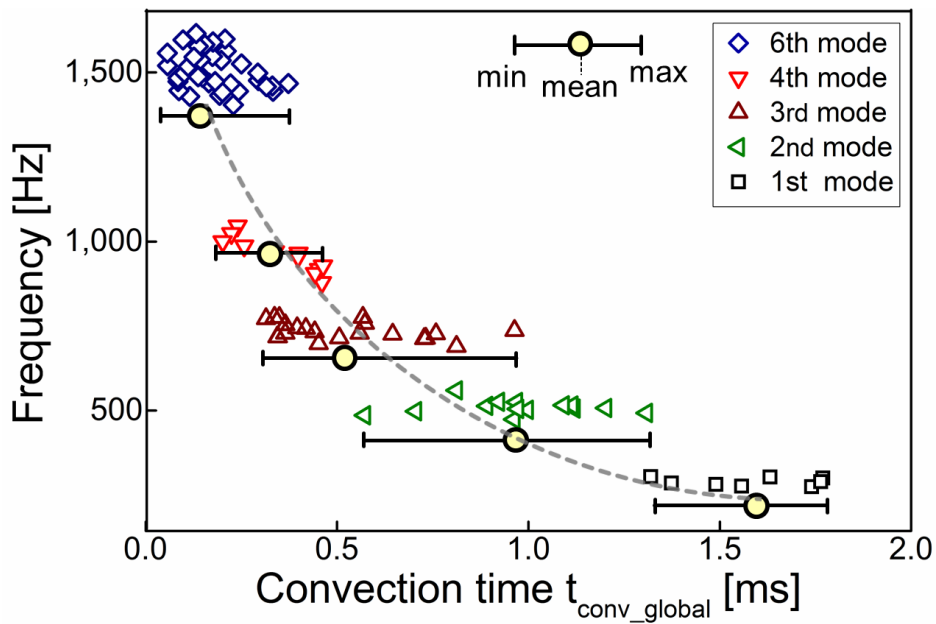


Fig. 4.7 Calculated τ_{conv_global} and combustion instability frequency.

Fig. 4.7 illustrates the relationship between the combustion instability frequency and τ_{conv_global} obtained from all the test cases of variations in fuel composition, airflow rate, and ϕ . The inverse relationship between the combustion instability frequency and the τ_{conv_global} can be clearly seen, and this relationship provides a key clue to explain the FMS described in previous section, as the reduction in the τ_{conv} due to the increase in airflow rate from 825 slpm to 1,375 slpm was merely 27%, significantly lower than the τ_{conv} 72% reduction due to the ϕ increase from 0.55 to 0.85. Note also that the different modes can occur at the same

τ_{conv} (i.e., an overlap of τ_{conv} interval for other modes), and the overlapping increased with decreasing τ_{conv} , (i.e., higher modes). The instability-triggering τ_{conv} exists as a range, not a specific value because, as mentioned by the Lieuwen [7], the possible condition of combustion instability occurrence exists as the range based on time-lag analysis. Thus, the criterion of τ_{conv_global} for judging the onset of FMS cannot be precisely determined, which explains the scattered data in Fig. 4.7. The calculated τ_{conv} overlapping phenomenon will be concerned in the Chapter 4.3 multi-mode instability characteristics.

Since the τ_{conv_global} cannot be represented as the exact value of the unburned mixture velocity, the τ_{conv_real} , which is calculated from the real velocity field by applying PIV, is introduced:

$$\tau_{conv_real} = \sum_{i=1}^n \frac{(l_{ub})_i}{(u_l)_i} \quad (4.2)$$

As shown in Fig. 4.6, where l_{ub} [m] is the equally divided local length along the mixture trajectory, and u_l [m/s] is the local velocity at each local distance, the fuel compositions containing 25, 50, and 75% H₂ (airflow rate = 1,100 slpm), which feature the 2nd, 4th, and 6th combustion instability modes, respectively, were selected as the representative conditions for the calculation of τ_{conv_real} .

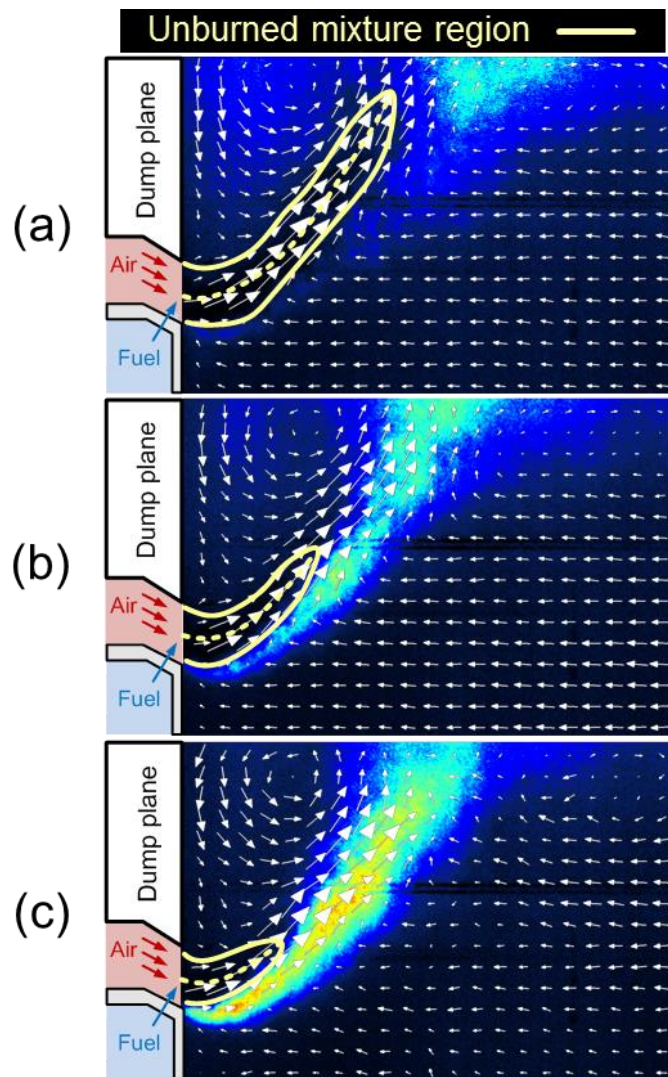


Fig. 4.8 Velocity field mapped with OH-PLIF images at (a) $H_2:CH_4 = 25:75$, (b) $H_2:CH_4 = 50:50$, and (c) $H_2:CH_4 = 75:25$. The unburned mixture region is shown as yellow lines, and the velocity field is depicted as white arrows.

Figure. 4.8 shows an overlap of the PIV and the OH-PLIF images. The flame surface formed at the vicinity of the lower velocity region in the shear layer and the increase in the H_2 composition resulted in the enlarged outer recirculation.

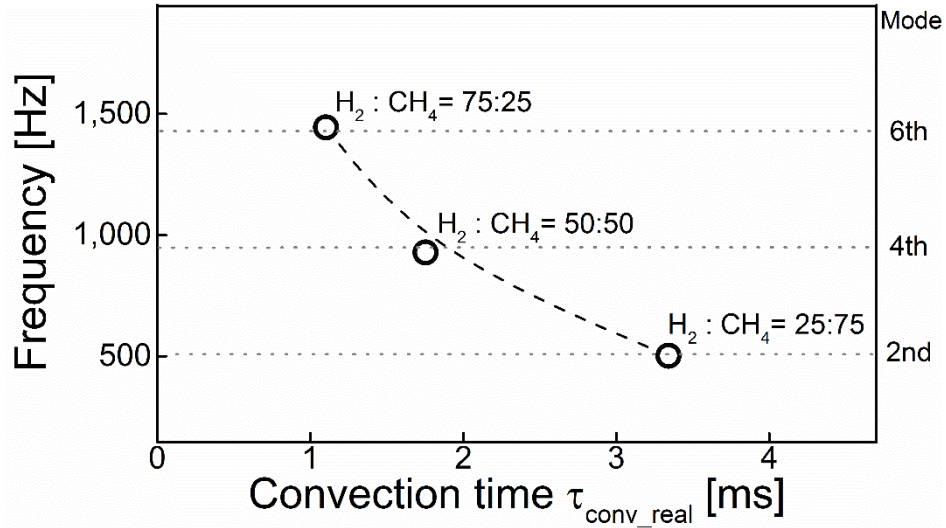


Fig. 4.9 Calculated τ_{conv_real} and combustion instability frequency.

The calculated τ_{conv_real} values are summarized in Fig. 4.9. The comparison of these values to the information presented in Fig. 4.7 shows that the values are not identical. For example, the τ_{conv_real} of the 2nd mode combustion instability conditions is 1.9 times longer than the averaged τ_{conv_global} value. The simplified mean exit velocity (U_e) was overestimated compared to the real velocity field because of fuel-air mixing, shown as a shorter τ_{conv_global} . However, the inverse correlation between the length of the τ_{conv} and FMS was clear in both calculations. In previous research, the τ_{conv} occupies more than 75% of the total time delay in the same partially premixed combustor [21]. Therefore, the reduction of the τ_{conv} must result in a drastic reduction in the total time delay and will appear as the combustion instability FMS phenomenon. The schematic prediction of the FMS phenomenon based on the τ_{conv} variation will be discussed in the following paragraphs.

4.2.3. Detailed Instability Mode Shifting Mechanism

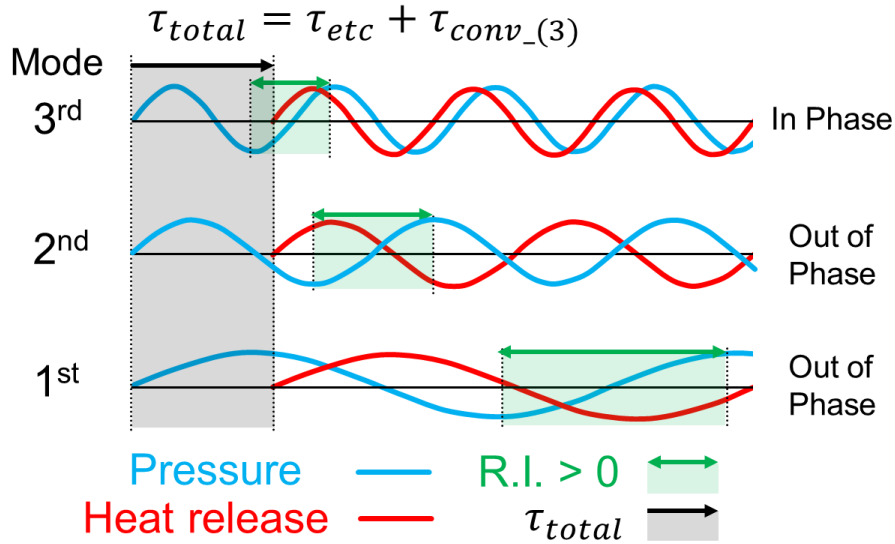


Fig. 4.10 Schematic prediction of the 3rd mode occurrence process based on the time-lag approach in a short $\tau_{conv_ (3)}$ condition. ($\tau_{etc} = \tau_{acoustic} + \tau_{chemical} + \tau_{ignition}$)

Fig. 4.10 shows the schematics of the relationship between the pressure fluctuation and heat release for certain combustion instability modes. All the longitudinal combustion instability modes freely exist in each test condition. The specific range of the total time delay (τ_{total}) (the green area in Fig. 4.10), which can satisfy a positive Rayleigh's index (R.I.), is a necessary condition for the appearance of the combustion instability.

$$R.I. = \int_0^T p'(t) \cdot q'(t) dt \quad (4.3)$$

The R.I.-satisfying region of the 2nd and 3rd modes overlaps and is similar to the overlap of the calculated $\tau_{conv_ global}$ in Fig. 4.7. Fig. 4.10 represents that each mode has a range of the τ_{total} to satisfy the necessary condition for the combustion instability triggering.

As previously mentioned, the τ_{total} is mainly affected by the τ_{conv} , and τ_{total} is presented as a black arrow. As shown in Fig. 4.10, when the τ_{total} satisfies the positive R.I region in the 3rd mode, the in-phase of the heat release and pressure fluctuation occurs and the combustion instability occurs in the 3rd mode frequency. If the τ_{conv} changes to a large value, it might be in-phased at the 2nd or fundamental mode time delay and the 2nd or fundamental mode instability might be triggered. In other words, this schematic shows that a reduction in the τ_{conv} causes the FMS to shift to a higher mode and the value of the τ_{conv} determines the occurrence of the FMS phenomenon.

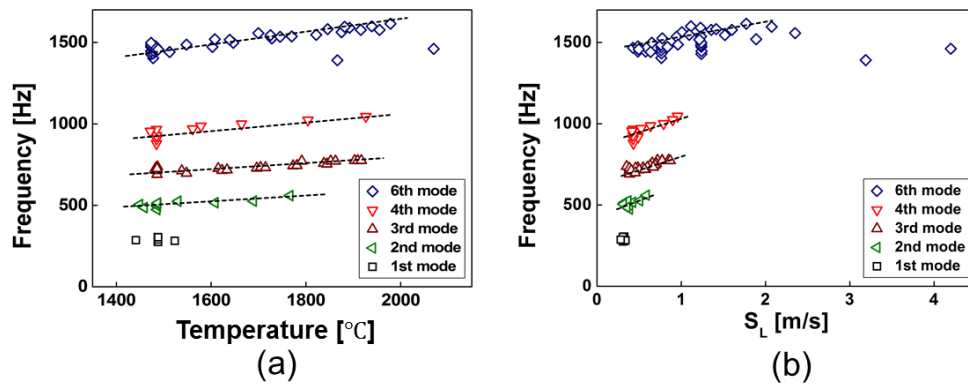


Fig. 4.11 Calculated parameters and instability FMS (a) adiabatic flame temperature (b) laminar flame speed.

The relation between combustion instability FMS and, the adiabatic flame temperature or laminar flame speed, which were already calculated in the test conditions, were also analyzed to compare with the results based on convection time. Fig. 4.11 reveals that the instability frequency in same mode linearly increased with the increase of adiabatic flame temperature and calculated laminar flame speed. However, the FMS trend is difficult to figure out in previous mentioned figure. Therefore, the similar approach, which like the convection time analysis, was derived as the application of inverse of the adiabatic flame speed and the laminar flame speed.

The Fig. 4.12 shows the inverse relation between FMS and each parameters: invers of adiabatic flame temperature, invers of laminar flame speed and calculated global convection time. The laminar flame speed directly influences the flame structure. Also, the structural change of the flame was closely related with the instability FMS phenomenon in the convection time analysis. Therefore, the effect of laminar flame velocity changes is already reflected in the convection time analysis. In other words, it can be confirmed that the convection time is the parameter that best represents the combustion instability FMS phenomenon by comparing the three parameter analysis results.

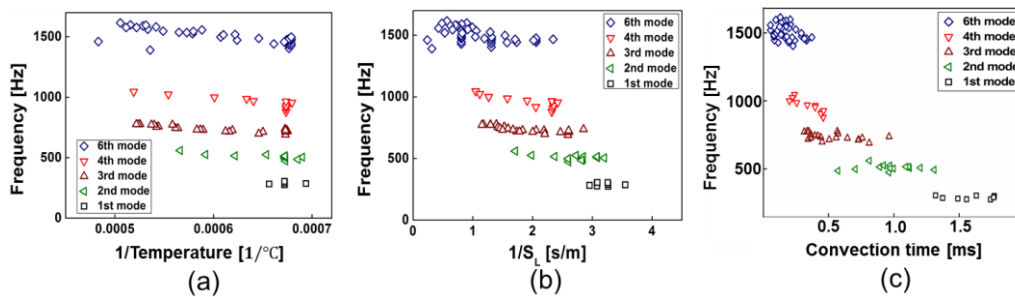


Fig. 4.12 Inverse relation between calculated parameters and FMS (a) invers of adiabatic flame temperature (b) invers of laminar flame speed (c) global convection time.

In addition, the previous research about the instability mode shifting phenomenon results were analyzed in the Fig. 4.13. First, the results from T. Liewwen was conducted in the premixed combustor and the mixing length was much longer than our study [7]. Therefore, the convection time was mainly influenced by the inlet velocity. In other words, the increase of inlet velocity reduces the τ_{conv} and it results in the increase of instability modes as shown in Fig. 4.13(a). In opposite, the equivalence ratio variation was the trigger of the instability mode shifts at the results of Balachandran [22] and Shanbhogue [24] as shown in Fig. 4.13(b) and (c). Especially, the drastic flame structure variation was reported during the equivalence ratio variation at the study of the Shanbhogue [24]. These structural variation must varies the τ_{conv} , which was confirmed in our hypothesis and it must be the triggering source of the instability FMS phenomenon.

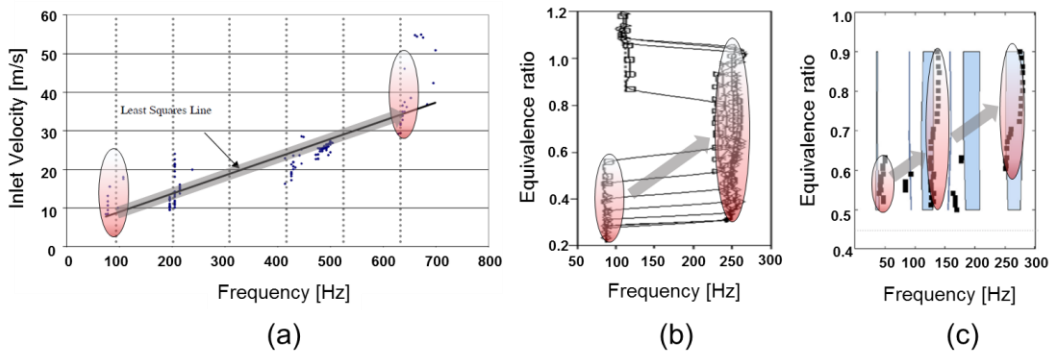


Fig. 4.13 Application τ_{conv} approach in the previous research related with the instability FMS phenomenon. (a) T. Lieuwen, (b) R. Balachandran, (c) S.J. Shanbhogue

The inverse relation between the calculated global convection time and the instability frequency were already revealed in chapter 4.3.2. However, the combustion instability amplitude is the other main parameter and that information was shown as the size of the circle in Fig. 4.14. The strong instabilities were mainly occurred in the longitudinal 2nd, 3rd and 6th mode conditions. Especially, in the 2nd and 6th mode condition, the maximum instability amplitude cases were mainly located in the middle of the calculated convection time range. The middle part of the convection time is the part that is not influenced by the other modes, this kind of convection time characteristics is the cause of strong instability.

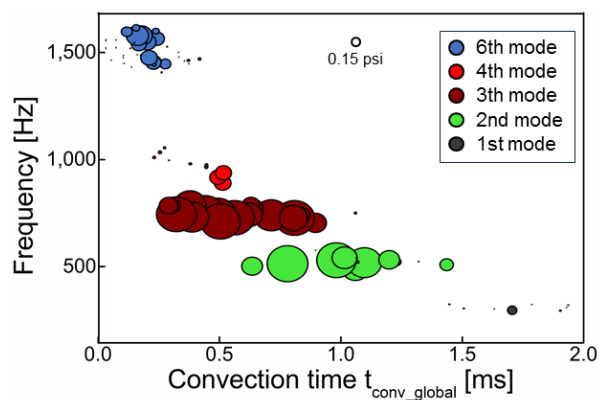


Fig. 4.14 Convection time, instability frequency and instability amplitude relation.

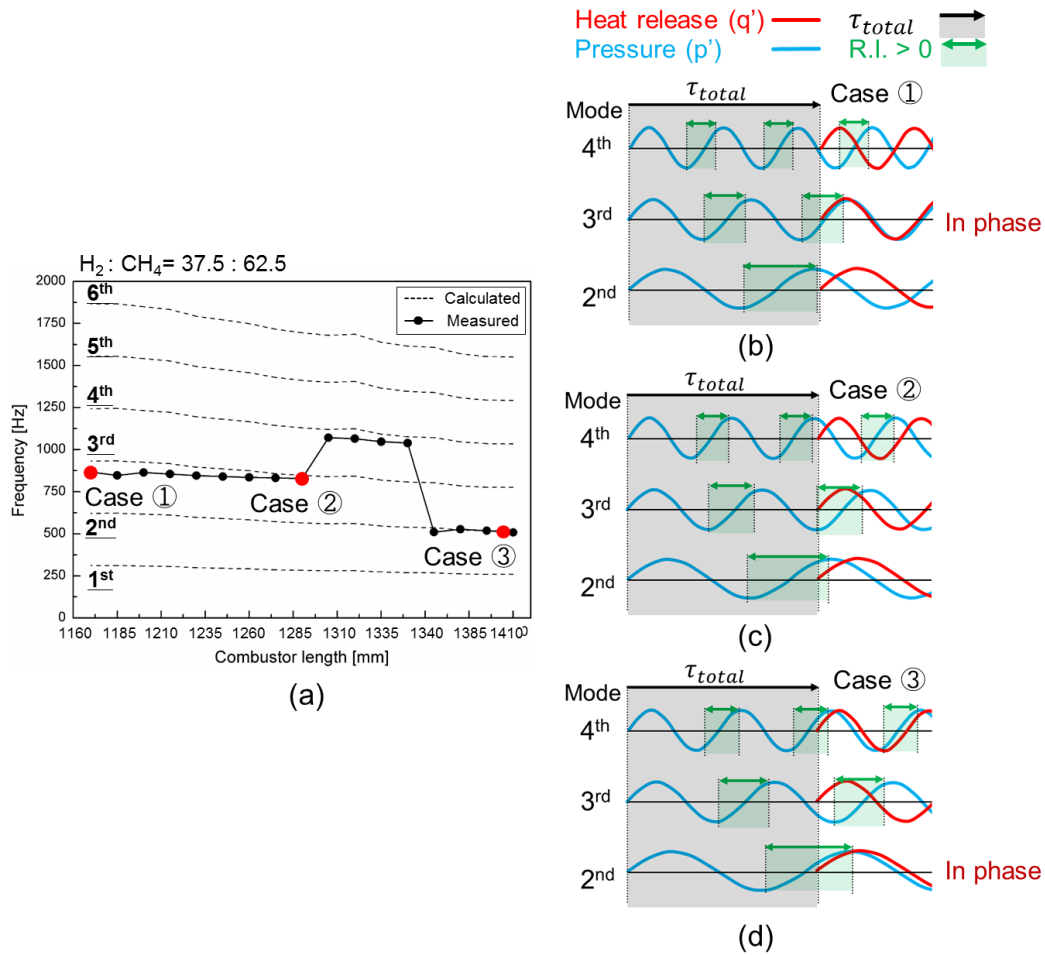


Fig. 4.15 Schematic analysis of instability FMS during the combustor length variation (a) Major instability frequency trends during the combustor length variation, Simplified time-lag analysis (b) case 1 (c) case 2 and (d) case 3.

The reason of instability FMS phenomenon during the combustor length variation also discussed in this part. As the burner length changed from 1170 mm to 1410 mm in the $H_2:CH_4 = 37.5:62.5$ fuel composition, the combustion instability frequency tended to change from the 3rd mode to the 4th mode and again to the 2nd mode. As shown in Fig 3.14, the flame structure did not reveals the considerable change, therefore, the calculated convection time of the combustor was almost uniform during the combustor length

variation. However the combustor length variation directly influences the acoustic field of the combustion chamber. The increase of combustor length results in the increase of the fundamental frequency and the time period of instability cycle is also increased. The increased instability period deforms the instability possible region (green area in Fig. 4.15) in time-lag analysis and it was suspected as the reason of instability FMS during the combustor length variation. Fig. 4.15(b) case, total time delay matches 3rd mode instability possible region and it shows 3rd mode instability in the experiments also. However, when the combustor length increased from 1170 mm to 1410 mm, total time delay remains constantly and it satisfies the 2nd and 4th mode instability. In that case, the measured instability frequency also shifts to 2nd mode frequency. This is because the instability possible region has changed to the 2nd and 4th modes due to the change in the length of the combustor.

In summary, the test condition variation, in fixed combustor geometry, affects the convection time and total time delay. Conversely, changes in the length of the combustor act in the direction of changing the region of combustion instability possible region in the time-lag analysis. Although the two factors as mentioned before are influenced different combustion instability related variables, however, both cause combustion instability FMS phenomenon.

4.3 Multi-mode Instability Characteristics

4.3.1. Instability Categorization

The instability frequency shifted from the fundamental mode (≈ 250 Hz) to the 6th harmonic frequency of the longitudinal mode (≈ 1500 Hz) during the fuel composition and equivalence ratio variation in the partially premixed combustor. The cause of the instability mode shifting phenomenon was discussed in previous work [27]. The convection time was believed to be the key parameter of the instability mode shifting phenomenon and it was defined as shown in the Fig. 4.16. The simplified global convection time was calculated as the fuel travelling distance divide by the fuel injection velocity at the nozzle exit in the previous paragraph. The inverse correlation between the calculated convection time and instability frequency was found as shown in Fig. 4.17(a). In research by Lee et al., the convection time occupied more than 75% of the total time delay in the partially premixed combustor [21]. Therefore, the reduction of convection time should have resulted in a drastic decrease in the total time delay. It caused the instability frequency and mode shifting.

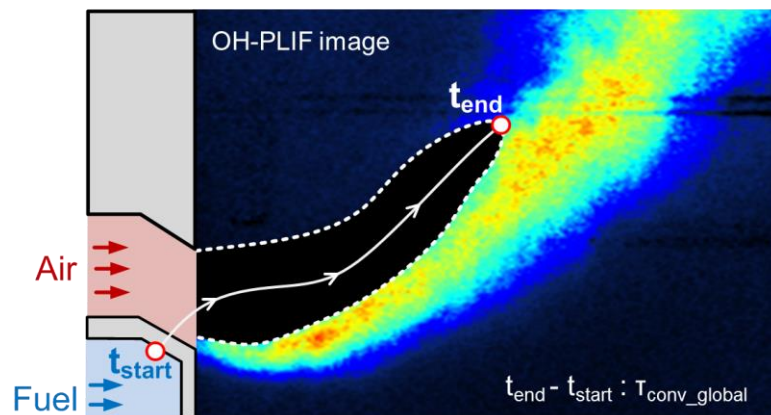


Fig. 4.16 Definition of convection time based on OH PLIF.

The detailed mechanism of mode shifting could be described as the simplified time-lag analysis based on Rayleigh's criteria. The convection time was regarded as the

triggering parameter of the instability frequency mode shifting phenomenon. However, the calculated convection time of each instability mode broadly overlapped, as depicted in the Fig. 4.17(a). In particular, the overlapped range of the 2nd and 3rd modes was more than half of the total convection time range.

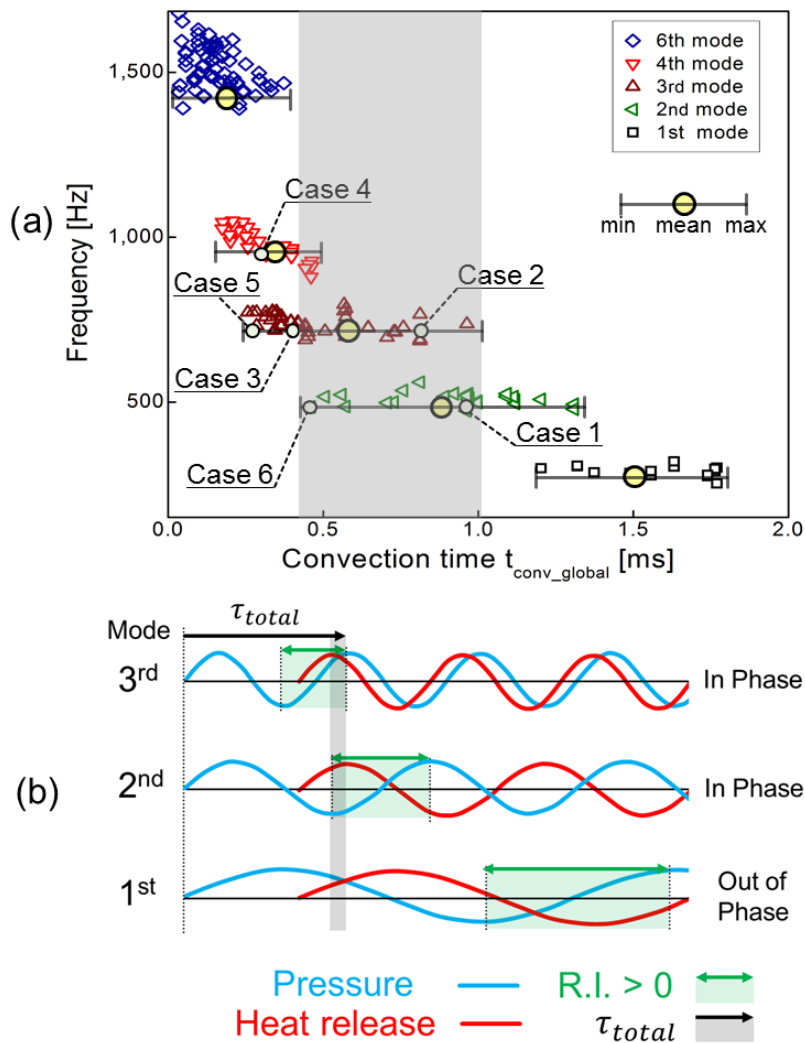


Fig. 4.17 Instability mode shifting characteristics of various test conditions. (a) Relation between the calculated convection time and instability frequency. (b) Instability of the possible region base in a simplified time-lag analysis.

The cause was assumed to have been based on simplified Rayleigh's criteria. As shown in Fig. 4.17(b), the instability possible range of the 2nd and 3rd modes was the overlapping on account of the time-lag based analysis. It showed a 10~20% overlap. The overall trend of overlapping was same; however, the degree was different in between calculated range and estimate range. The reasons for the difference were as follows. The calculated values were the simplified convection time and part of the total time delay, which was applied at the time-lag analysis. However, the similar overlapping trend of the calculated convection time and possible instability region showed the unique characteristics of instability that occurred in this study. In other words, the co-existing or intermittent characteristics of the instability mode in the specific time delay simultaneously satisfied the 2nd and 3rd modes of the possible instability region.

Therefore, for the first step, we categorized the instability characteristics that occurred during the various conditions of the tests, such as the variation of fuel composition, airflow rate, and equivalence ratio tests. All test conditions were employed twice for the reproducibility of the unique instability characteristics. The combustor length and inlet temperature, which mainly affected the instability frequency, were fixed during the experimental approach. In conclusion, the cause of multi-mode instability or instability mode intermittency was identified based on the time domain, frequency domain, and continuous wavelet transform.

In other words, the instability characteristics were directly influenced by not only the time domain information, but also the frequency domain information. Therefore, all test conditions were categorized in two approaches: the time domain and frequency domain. Fig. 4.18(a) and (b) depict a schematic graph of periodic and dynamic instability pressure oscillation based on the time domain approach. The periodic instability was defined as the case where the pressure perturbation intensity and frequency were kept constant over time. On the contrary, dynamic instability is defined as the frequency and perturbation intensity varying with time. In addition, in terms of the frequency domain, the measured pressure data were analyzed by FFT. Their shapes were used as categorizing criteria of the frequency domain approach. Based on the analysis of the combustion instability phenomenon, the

instability frequency revealed significant information about the characteristics of the instability, specifically the frequency that is important in that facility, and a clue for the combustion instability suppression. Fig. 4.18(c) depicts the single frequency case, and (d) illustrates the dual frequency case. In other words, the latter case shows the integer multiplied frequencies. Fig. 4.18(e) illustrates the multiple frequency case. For example, it shows that the 2nd, 3rd and 4th mode instability frequencies exist as similar amplitudes or various frequencies that co-exist.

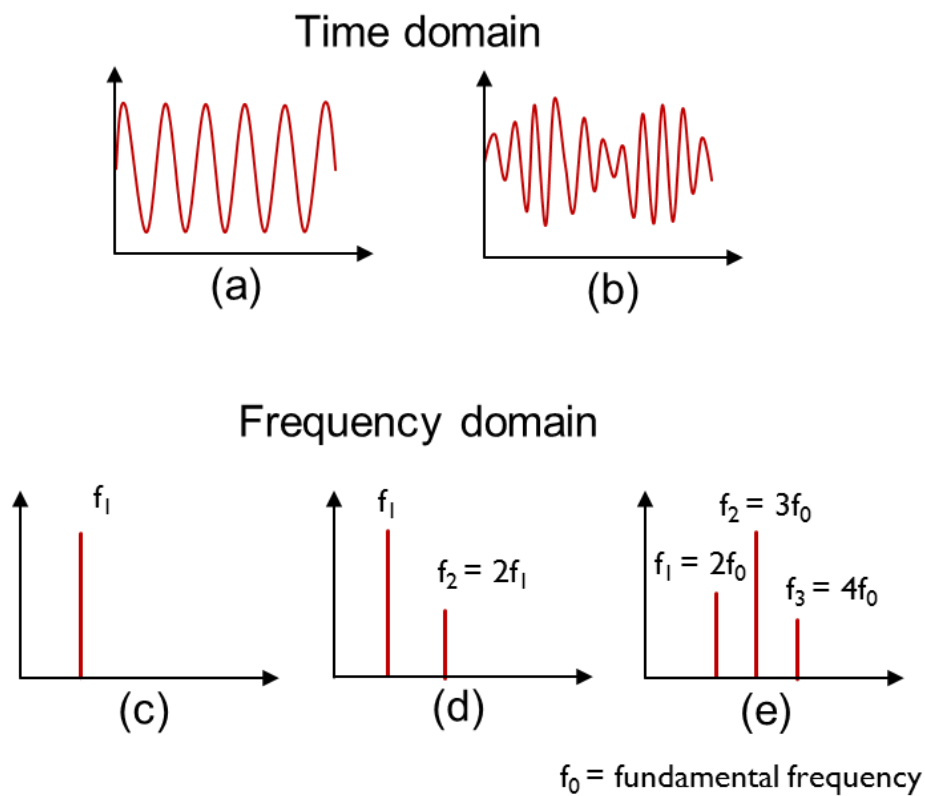


Fig. 4.18 Combustion instability categorization based on the time and frequency domain. (a) Time domain: periodic. (b) Time domain: dynamic. (c) Frequency domain: single instability. (d) Frequency domain: dual instability. (e) Frequency domain: multiple frequency instability.

Consequently, the instability characteristics were categorized in six cases. The two cases of the time domain and three cases of the frequency domain categorization, as shown in Fig. 4.18, were combined as follows: Case 1: periodic and single frequency; Case 2: periodic and dual frequency; Case 3: periodic and multiple frequency; Case 4: dynamic and single frequency; Case 5: dynamic and dual frequency; and Case 6: dynamic and multiple frequency. In addition, the appropriate test conditions of each instability case were selected, as shown in Table 4.2, for detailed evaluation of each case. The convection time and major instability frequency of each selected case was shown in the Fig. 4.17(a). Subsequent studies will be conducted based on the six categorized cases and selected test conditions.

Table 4.2 Selected test conditions for each of the six categorized cases.

Periodic instability		Dynamic instability	
Case 1 (single)	H ₂ : 0.0% ϕ : 0.70 V _{air} : 1100	Case 4 (single)	H ₂ : 37.5% ϕ : 0.75 V _{air} : 1100
Case 2 (dual)	H ₂ : 37.5% ϕ : 0.56 V _{air} : 963	Case 5 (dual)	H ₂ : 12.5% ϕ : 0.80 V _{air} : 1100
Case 3 (multiple)	H ₂ : 50.0% ϕ : 0.56 V _{air} : 963	Case 6 (multiple)	H ₂ : 50.0% ϕ : 0.56 V _{air} : 825

Firstly, the time domain analysis of the periodic instability, such as Cases 1, 2 and 3, are summarized in Fig. 4.19. The dynamic pressure sensor, which were located at the dump plane, were used for the time domain analysis. The 0.25 s continuous trend of pressure data are shown in the upper part of the figure. The pressure trends of the selected times, which can represent the characteristics of each case, are shown in the lower side of the figure. Each case shows that the amplitude and shape of the fluctuating limit cycle are consistent over the time domain. In addition, the one cycle shape in lower part of Fig. 4.19(a) shows a sine-wave-like structure, while (b) and (c) show a deformed wave shape on account of the complex instability frequency.

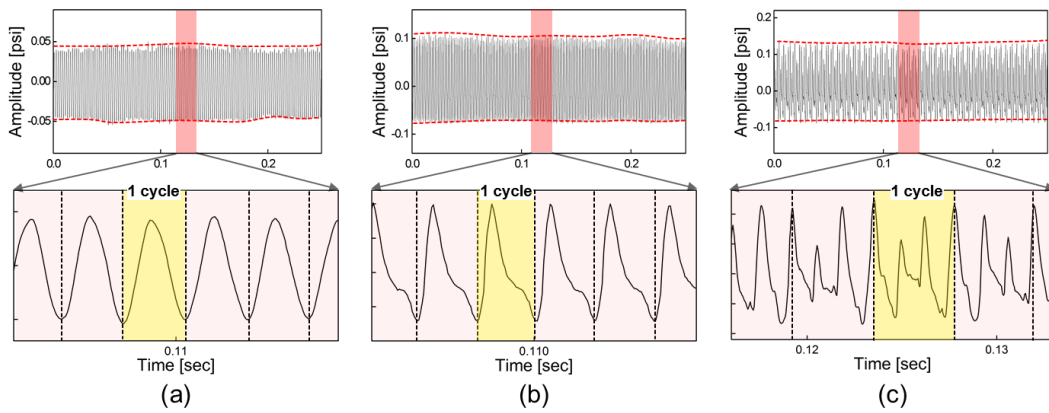


Fig. 4.19 Overall trend and specific cycle of the steady unstable condition characteristics based on the time domain pressure signal: (a) Case 1 (periodic: single instability), (b) Case 2 (periodic: dual instability), (c) Case 3 (periodic: multiple instability).

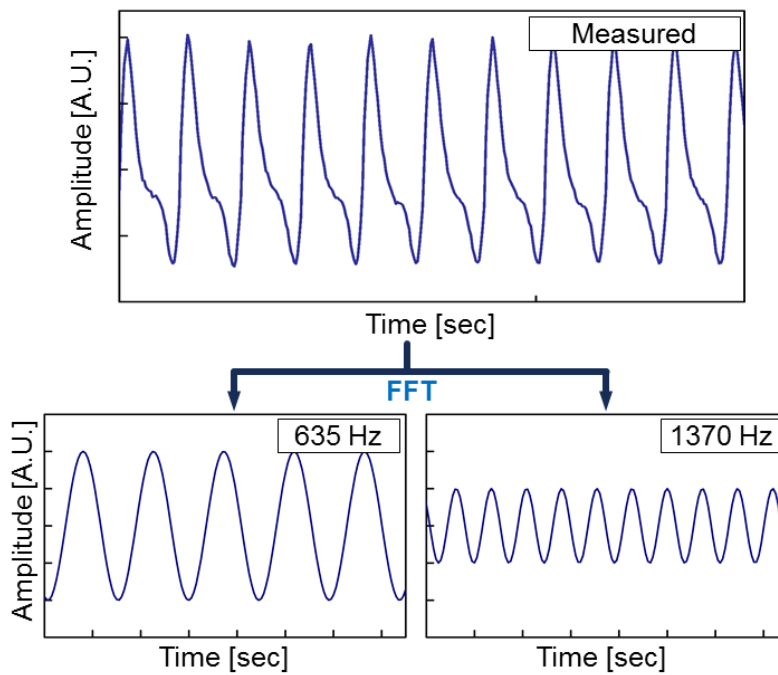


Fig. 4.20 Comparison of the measured time domain signal and reconstructed signal, Case 2 (periodic: dual instability)

Research on the time domain wave shape of the multi-mode instability was conducted by Lee et al., who suggested that the skewness time be used to improve the accuracy of the time-lag analysis [21]. In this study, the one cycle shape of the dynamic pressure could successfully reconstruct the sine wave summation. The frequency and amplitude of case 2 were calculated based on the FFT analysis data, which are presented in Fig. 4.22(b). Fig 4.20 shows a comparison of the measured and reconstructed time domain pressure signals. It can be mainly decomposed as the two major sine waves as 635 Hz and 1370 Hz, which were measured by FFT. As mentioned above, the cause of the limit cycle deformation was confirmed by the reconstruction of the time domain signal.

Fig. 4.21 shows the unsteady time history of the pressure, which represents Cases 4 to 6. The 1 s time trend represents the drastic variation of the limit cycle amplitude in the upper figure. The lower figure shows specific variation of the dynamic pressure signal in each case. Fig. 4.21(a) shows the small amplitude instability and the peak-to-peak amplitude varies, but Figs. 4.21(b) and (c) show the developing instability; therefore, the gradual variation of limit cycle amplitude can be found in both overall view and specified selected time.

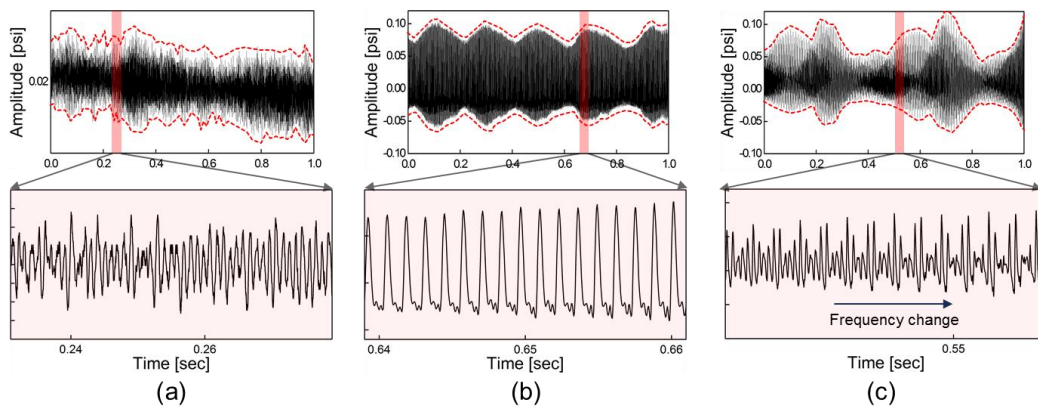


Fig. 4.21 Overall trend and specific cycle of unsteady unstable condition characteristics based on the time domain pressure signal: (a) Case 4 (dynamic: single instability), (b) Case 5 (dynamic: dual instability), (c) Case 6 (dynamic: multiple instability).

From the time domain analysis of the categorized cases, the difference of periodic and dynamic instability characteristics can be deduced from Figs. 4.19 and 4.21. However, the information that was important for analyzing the combustion instability was the dynamic pressure frequency characteristics. However, the time domain analysis could not represent the frequency characteristics of instability. Consequently, the FFT analysis method was applied to identify the frequency information for each instability condition.

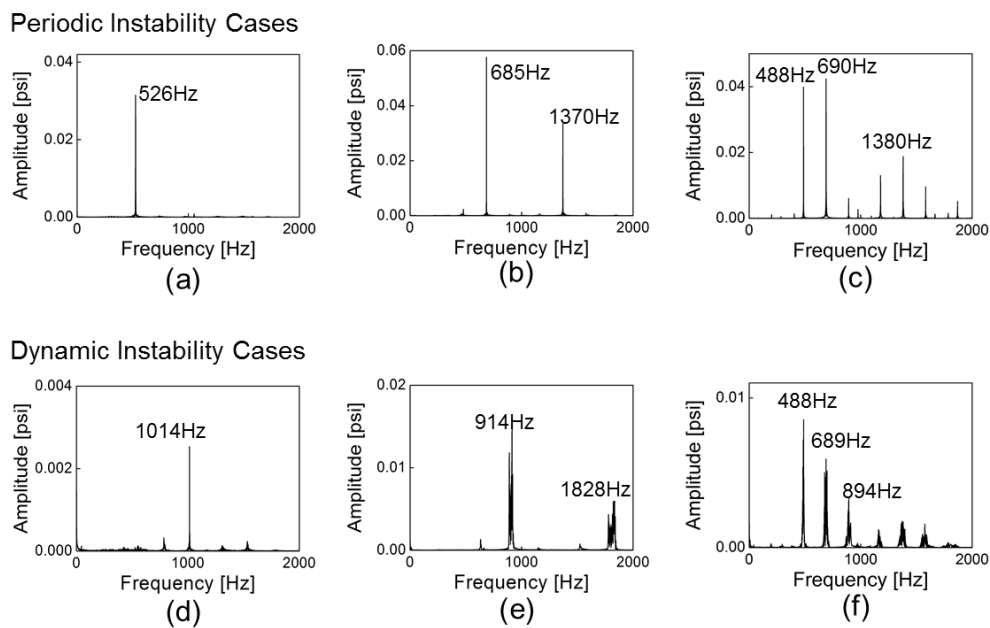


Fig. 4.22 Frequency domain characteristics comparison between periodic and dynamic instability conditions. Cases: (a) 1, (b) 2, (c) 3, (d) 4, (e) 5, (f) 6.

Fig. 4.22 shows the summarized FFT that applied the results of all six cases. Although the frequencies were not identical, the distinct obvious frequency is evident in (a) and (d), where it is defined as “single frequency instability.” In the cases of (b) and (e), a step-like two harmonic frequency was calculated. It is defined as “dual frequency instability” in this study. Meanwhile, Figs. 4.22(c) and (f) show that the integer multiplied fundamental frequencies were calculated, unlike the cases of (b) and (e). This kind of applied FFT

instability result is defined as “multiple frequency instability.” The instability characteristics could be easily retained by application of the FFT.

However, the time domain information on each instability, such as the periodic and dynamic instability (Figs. 4.19 and 4.21), could not be determined with the frequency domain approach based on FFT. In other words, in the time domain, Fig. 4.19(c) and Fig. 4.21(c) show a considerable difference; however, in the frequency domain analysis, the difference is negligible. Thus, the combined merit of the time domain approach and frequency domain approach is essential for the instability analysis, especially in the time varying multi-mode instability case. Therefore, the continuous wavelet transform was applied in the six categorized cases.

4.3.2. Reason of Multi-mode Instability

Fourier transform provides the spectral content of the signal. However, it provides no information on the places in time in which those spectral components appear. The continuous wavelet analysis was performed such that the time domain signal was compared with a wavelet function. The transform was separately computed for different segments of the time domain signal. In this analysis, the “bump wavelet” was used as the wavelet of the continuous wavelet transform. The 1 s duration data were applied in the continuous wavelet transform.

In Fig. 4.23, the y-axis represents the instability frequency; the x-axis denotes the time history of the instability frequency variation. In addition, the color of the contour means the relative amplitude of each frequency. In addition, the figure illustrates the periodic cases that show a constant instability frequency and amplitude during the total time length. In a detailed view, multi-mode instability characteristics can be captured as the co-existence of frequency in the full time range from 0 s to 1 s, as shown in Figs. 4.23(b) and (c). As mentioned earlier, the dual frequency instability and multiple frequency instability characteristics of all cases, which were derived from the frequency domain approach and are shown in Figs. 4.22(b) and (c), are also readily apparent.

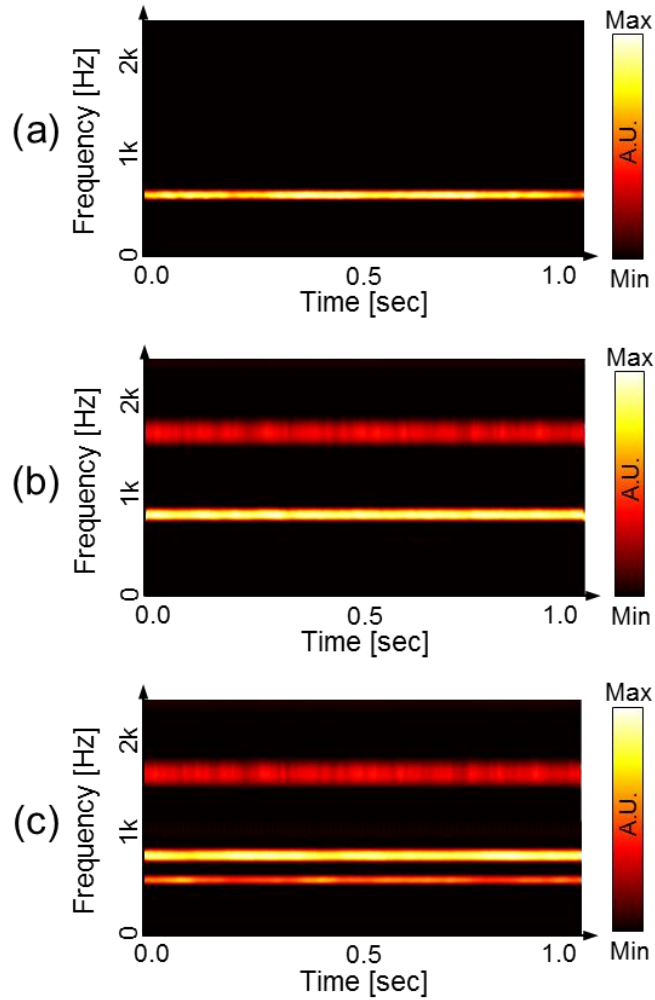


Fig. 4.23 Applied results in the continuous wavelet transform in the periodic instability condition. (a) Case 1, (b) Case 2, (c) Case 3.

Fig. 4.24 shows the three cases of instabilities, specifically the dynamic instability condition that was categorized by the time domain analysis. In contrast to the periodic instability analysis shown in Fig. 4.23, the instability amplitude and frequency trend shows a drastic variation during the time history. In a detailed view of each case, Fig. 4.24(a) shows that the instability fluctuation energy was mainly concentrated in a specific

frequency band, and the instability amplitude obviously varied in the passage of time. Similarly, as shown in Fig. 4.24(b), the instability fluctuation energy was mainly located near regions of 750 Hz and 1500 Hz and during the passage of time. In addition, only the 750 Hz energy concentration varied, and the maximum instability amplitude was found near 1 s from the start of the measurement.

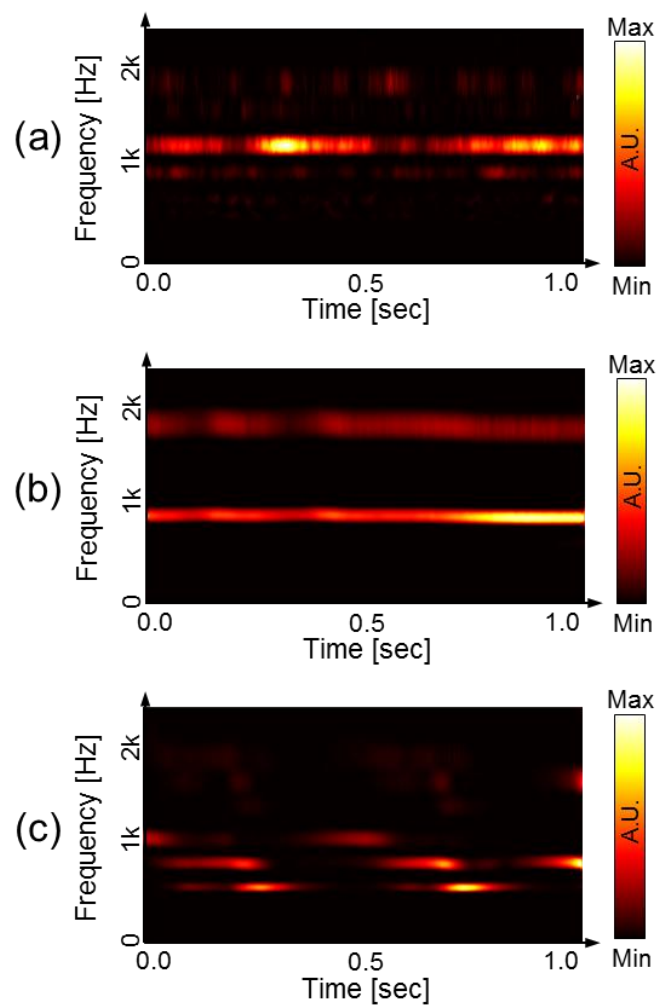


Fig. 4.24 Applied results of the continuous wavelet transform in a dynamic instability condition. (a) Case 4, (b) Case 5, (c) Case 6.

However, the last case shown in Fig. 4.24(c) reveals unique characteristics; i.e., the instability frequency traveling from 500 Hz to 1,000 Hz during the passage of time. Cases 3 and 6 show FFT analysis results that are similar to those in Figs. 4.22(c) and (f). However, in continuous wavelet transform analysis, the instability trend shows a drastic difference when Figs. 4.23(c) and 4.24(c) are compared. In other words, case 3 (periodic-multiple instability), such as in Fig. 4.23(c), shows co-existence of various instability frequencies. However, Fig. 4.24(c) shows the instability frequency traveling phenomenon.

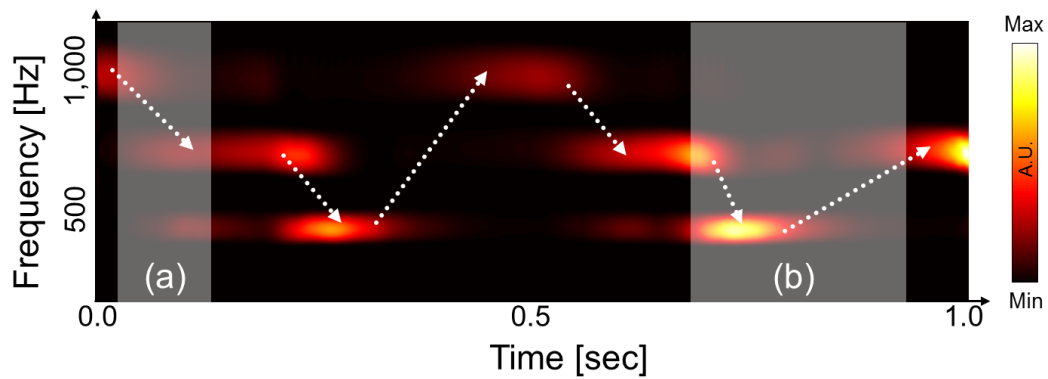


Fig. 4.25 Continuous wavelet transform application in the intermittency condition of instability. (a) High-frequency to low-frequency shifting region (b) Low-frequency to high-frequency shifting and drastic amplitude fluctuating region.

A detailed analysis of Case 6 is now presented. The applied result of the continuous wavelet transform of the dynamic-complex instability is summarized in Fig. 4.25. As briefly mentioned above, the instability mode travels between 1000 Hz (4th harmonic instability of the fundamental frequency), 750 Hz (3rd harmonic instability of the fundamental frequency), and 500 Hz (2nd harmonic instability of the fundamental frequency) while time proceeds from the start to 0.2 s. The frequency varies from 500 Hz to 750 Hz, while the time passages from 0.7 s to 0.9 s.

Through the analysis of the multi-mode instability, two types of multiple frequency

instability could be found. In the first case, when the multi-mode instability occurred, the various frequencies co-existed, as in Fig. 4.22(c). This is reflected as a complex wave form of each cycle as shown in Fig. 4.19(c). In contrast to the first condition, Case 6 shows sequentially traveling frequencies, and each frequency exists in a very short time period. Owing to this rapid variation, the FFT results from this type of instability show results similar to those of Case 3, as shown in Figs. 4.22(c) and (f). In short, the multi-mode instability appears in two ways: the co-existence of various acoustic mode frequencies, and the instability mode traveling between various acoustic mode frequencies.

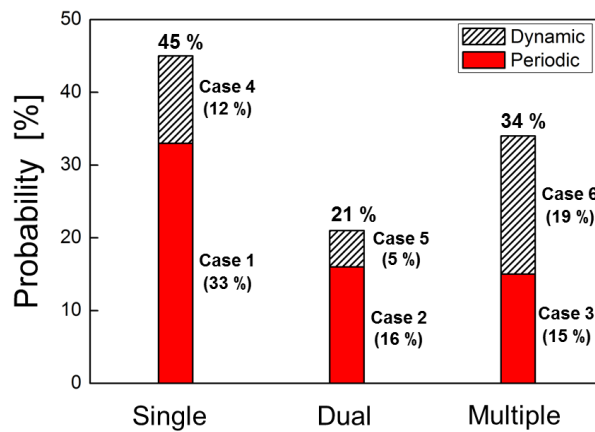


Fig. 4.26 Instability occurrence possibility of each type based on categorized test condition.

For further study, all test conditions were analyzed based on the time and frequency domain. They were categorized based on the six cases, as defined in Table 4.2. The categorized instability occurrence possibility of each test conditions is summarized in Fig. 4.26. The ratio of the periodic instability to the dynamic instability was 64:36; in other words, almost 2/3 of the test condition shows the fully developed periodic limit cycle instability. The single frequency instability occupies 45% and multi-mode instability (dual and multiple frequency instability) shows 55% of the instability possibility based on total tested cases. In addition, the ratio of the co-existing multi-mode instability to the travelling multi-mode instability was 45:55.

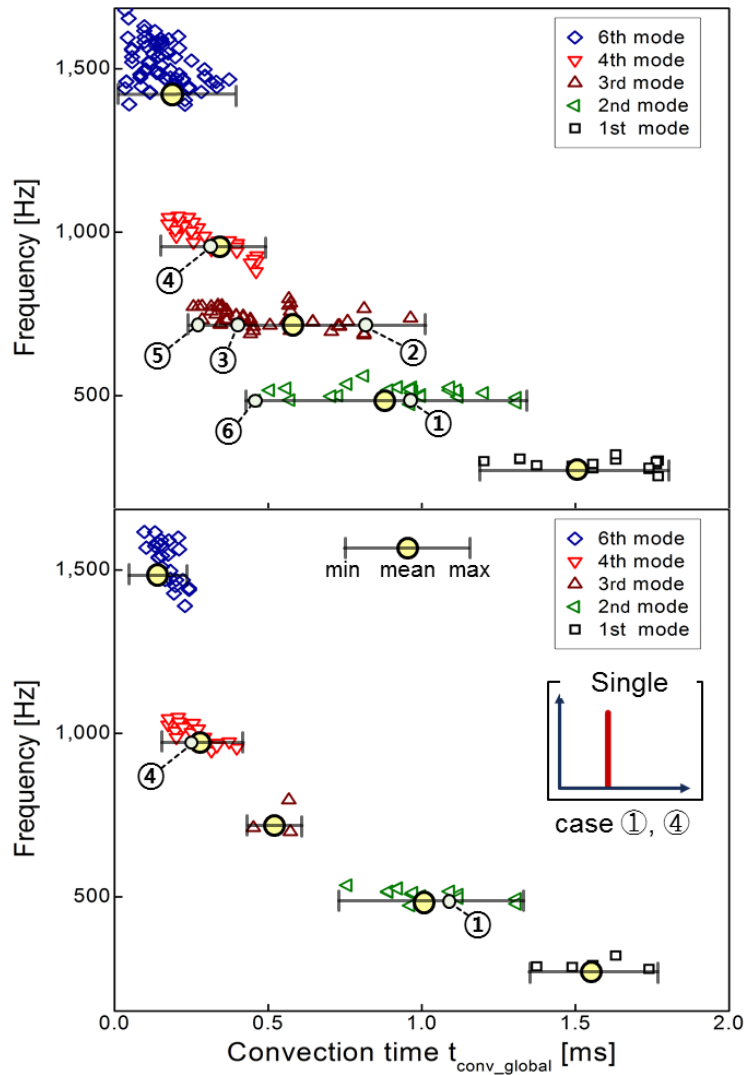


Fig. 4.27 Simplified calculated convection time and frequency based on categorized test conditions (upper) and the removal of the multi-mode instability occurrence condition (lower).

As mentioned in the first part of the study, Rayleigh's criteria based on the instability possible region overlapping was suspected to be the main cause of the multi-mode instability occurrence. The categorized six cases are overlaid in Fig. 4.17(a). Fig. 4.27

presents further analysis of the cause of the multi-mode instability occurrence. For each test case, the representative instability frequency was selected based on the FFT analysis. In the multi-mode instability case, the major peak frequency was selected. As shown in the upper part of Fig. 4.27, the single instability conditions, such as in Cases 1 and 4, were located in the middle of the calculated convection time range in each instability mode. However, the dual frequency instability conditions (Cases 2 and 5) and multiple frequency instability conditions (Cases 3 and 6) were located at the edge of the calculated convection time range of each mode. This region of convection time was already overlapping with the lower or higher instability mode.

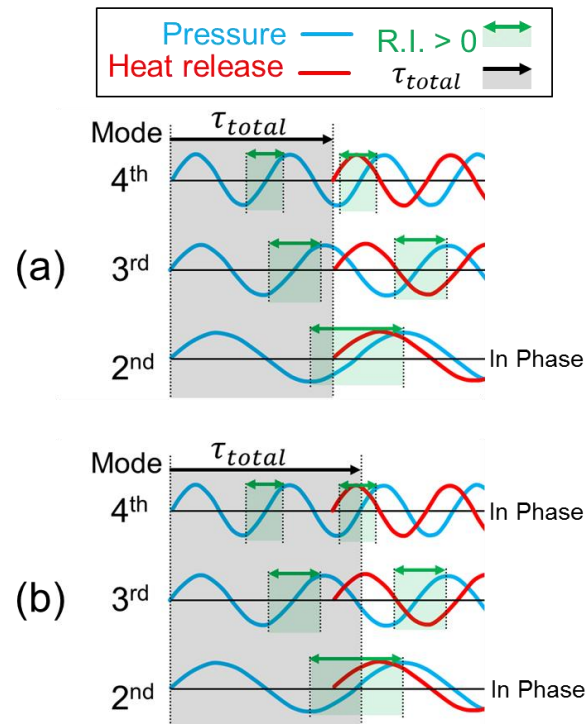


Fig. 4.28 Simplified Rayleigh's criteria of each instability case (a) single mode instability (b) multi-mode instability (green area indicates the positive Rayleigh index (instability possible region) and black area indicates the total time delay between pressure wave and heat release).

In summary, the specific convection time could satisfy several of Rayleigh's criteria of instability possible condition. In this condition, multi-mode instability could occur. On the other hand, the test results were located near the central value of the convection time in each mode and were separated from the other instability frequencies. The distinct instability frequency predominantly occurred. The example of the simplified Rayleigh's criteria shown in Fig. 4.28 can be used to assist the hypothesis of the multi-mode occurrence. Fig. 4.28(a) shows the schematic time-lag analysis of single frequency instability case, which satisfies only the 2nd mode. In contrast, Fig. 4.28(b) shows the multi-mode occurrence case schematic and the time delay satisfies the 2nd and 4th mode instability possible region (green area). This type of instability possible region overlapping is the suspected reason of the occurrence of multi-mode instability.

To confirm the hypothesis about the multi-mode instability occurrence, Cases 1 and 2, in other words, the single frequency instability cases (45% of total test conditions), remained as shown in the lower part of Fig. 4.27. The other cases (multi-mode) were removed from the data points of the graph shown in Fig. 4.17(a). The broad convection times of overlapping regions were almost eliminated. The small remaining range was only in the 4th and 6th modes. Of course, the convection time used in this study was not the exact value. It was calculated based on the measured flame structure based on OH-PLIF and the velocity that was assumed to be the simplified nozzle exit velocity. Therefore, the lower graph in Fig. 4.27 shows the trend of the convection time, not the exact value. Nevertheless, the combination of the categorized instability and assumed convection time showed an obvious relationship, especially with the remaining distinct mode condition, such as in Cases 1 and 4.

In addition, the dual frequency instability cases remained results and multiple frequency instability cases remained results were separately summarized in Fig. 4.29. In contrast to the single frequency instability remained results, the convection time overlapping phenomenon still remains. In addition, the multiple frequency instability cases were mainly occurred in the 6th mode and the reason for this phenomenon is that the short convection time easily satisfies various combustion instability possible region.

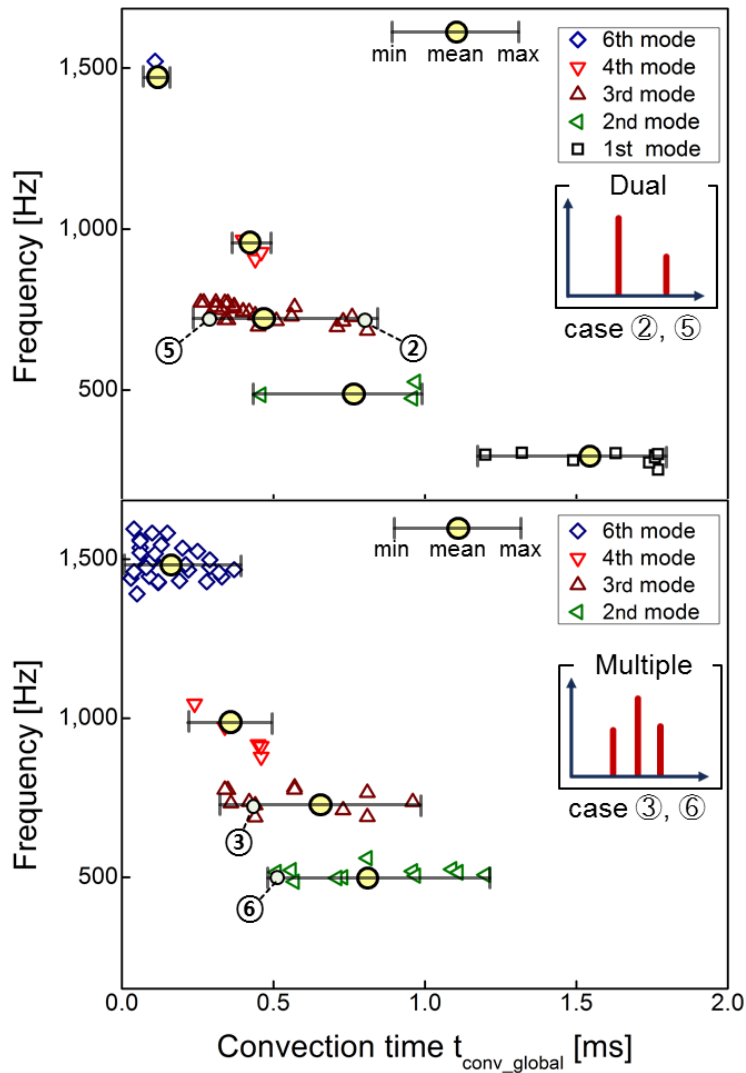


Fig. 4.29 Simplified calculated convection time and frequency based on dual frequency instability cases (upper) and multiple frequency instability cases (lower).

In this study, the importance of convection time variation in the occurrence of multi-mode instability was also confirmed; In conclusion, the combined instability mode categorization, based on both the time and frequency domain and the calculated convection time, demonstrated the cause of the multi-mode instability occurrence. The Rayleigh's

criteria co-satisfaction of two or more instability mode conditions could be suspected as the main cause of the multi-mode existence, which was confirmed based on the analysis of various test conditions. In addition, the multi-mode instability can also be classified as co-existing multi-mode and travelling multi-mode base on continuous wavelet transform.

CHAPTER 5

FLAME TRANSFER FUNCTION

5.1 Objectives and Test Conditions

The objective of this section was to measure the FTF ($G(f)$) under varied fuel composition, airflow rate, and ϕ conditions and to identify the flame characteristics by comparing the FTF with FMS. The FTF ($G(f)$) is a kind of transfer function that represents the relationship between the input variable (velocity fluctuation measured by HWA) and the output variables (heat release fluctuation measured by PMT with the OH* filter). Equation 5.1 was used for the FTF calculation.

$$G(f) = \frac{\dot{q}/q_{mean}}{\dot{u}/u_{mean}}, \quad Gain = |G(f)|, \quad Phase = \tan^{-1} \left[\frac{G(f)_{im}}{G(f)_{real}} \right] \quad (5.1)$$

Table 5.1 Flame transfer function test conditions

Parameters	Basic condition	Airflow rate	Equivalence ratio	unit
Combustion chamber pressure	1.1 ~ 1.2			atm
Air flow rate	23.5	17.8 ~ 29.6	23.5	g/s
Air inlet temperature	200			°C
Air velocity (nozzle exit)	48	35 ~ 60	48	m/s
Fuel (H ₂ composition)	25.0, 37.5, 50.0, 62.5, 75.0, 87.5			-
Reynolds number (air)	54,700	39,800 ~ 68,300	54,700	-
Lewis number	0.372 ~ 1.018			-
Modulation frequency	0 ~ 1,100			Hz
Swirl number	0.832			-

The FTF characteristics were found for various test conditions to research the causes of these characteristics. In addition, the periodic increase and decrease trend of the FTF gain was compared with the other groups and analyzed. Finally, combustion instabilities were predicted based on a 1-D lumped network model. The test conditions in which the flame transfer function were measured are summarized in the following Table. 5.1.

5.2 Flame Transfer Function Characteristics

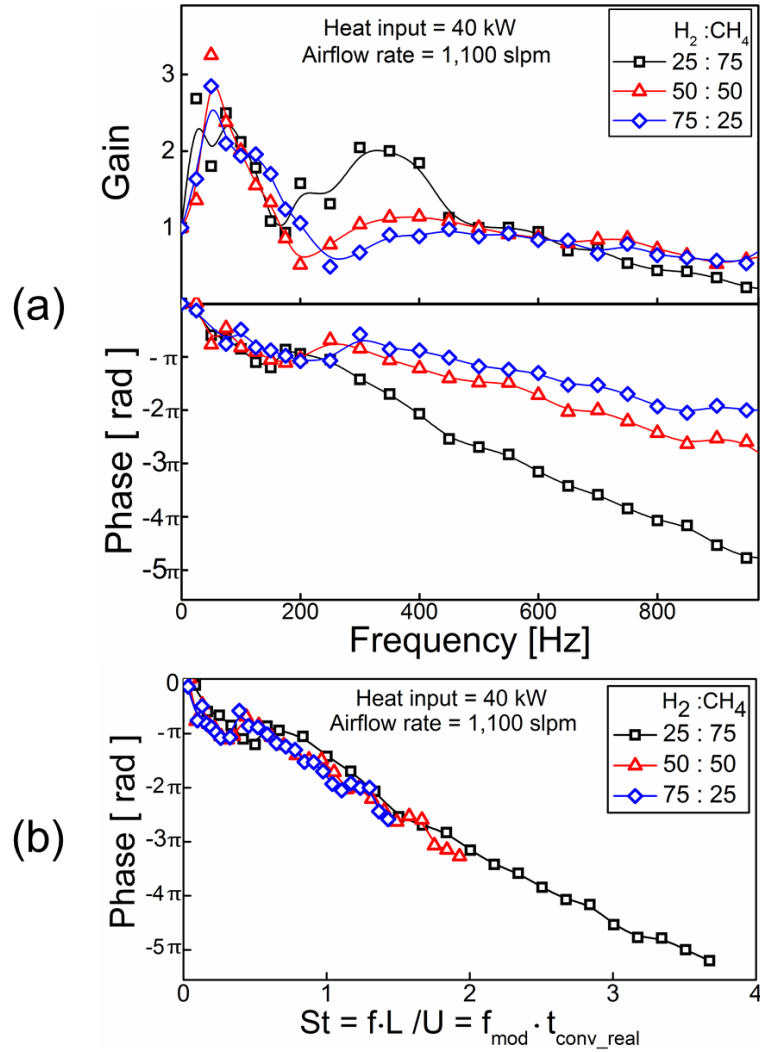


Fig. 5.1 Measured FTF under varying fuel compositions; (a) FTF gain and phase (b) phase normalized by the Strouhal number (St).

As shown in Fig. 5.1(a), increasing the H₂ composition of the fuel caused a reduction in the decreasing gradient of the FTF phase. Satisfying the heat input of 40 kW for each

fuel composition required that the total volume flow rate increased with an increasing H₂; thus, the fuel delivery velocity was also increased (H₂, LHV = 12.12 MJ/m³, CH₄, LHV = 37.71 MJ/m³). Therefore, the reduction in the FTF phase decreasing gradient is due to the reduction in the input perturbation delivery time as the H₂ composition increased. A repeating increase and decrease in the FTF gain was found during the modulation frequency increase, and a similar trend in the FTF gain was found in both the experimental measurements [44] and the theoretical approach [43]. Preetham et al. [42] found different responses theoretically for conical and V-shape flames. The V-shape flame response shows a periodic behavior that reflects the increase and decrease in the FTF gain. These previous studies were conducted on premixed combustors, unlike the present research, but the flame shape was same; thus, the flame shape (V-shape) was the main factor for the FTF gain characteristics.

In addition, as seen in the upper part of Fig. 5.1(a), the increased H₂ composition reduced the value of the FTF gain. The gain is the ratio between the output fluctuation and the input modulation amplitude, so its low value demonstrates the insensitivity of the system at that frequency. Increases in the H₂ composition resulted in changes in the fuel chemical properties, such as the higher reaction rate and the faster flame speed, which gave a robust flame, and this was reflected in the reduction in the FTF gain value.

$$St = \frac{f \cdot L}{U} \quad (5.2)$$

Fig. 5.1(b) shows the FTF phase normalization by the St . Based on the definition of St which shown in Equation 5.2, the modulation frequency and $\tau_{\text{conv_real}}$ were used (these calculations were discussed in Section 4.2.2). Based on the definition of St , the characteristic length (L) divided by velocity (U) was replaced by the $t_{\text{conv_real}}$. In other words, the L was replaced by the unburned mixture length. The normalized phase converged into one line, and this demonstrates that the St based on $\tau_{\text{conv_real}}$ is a key parameter for understanding the FTF characteristics seen in response to fuel composition variations.

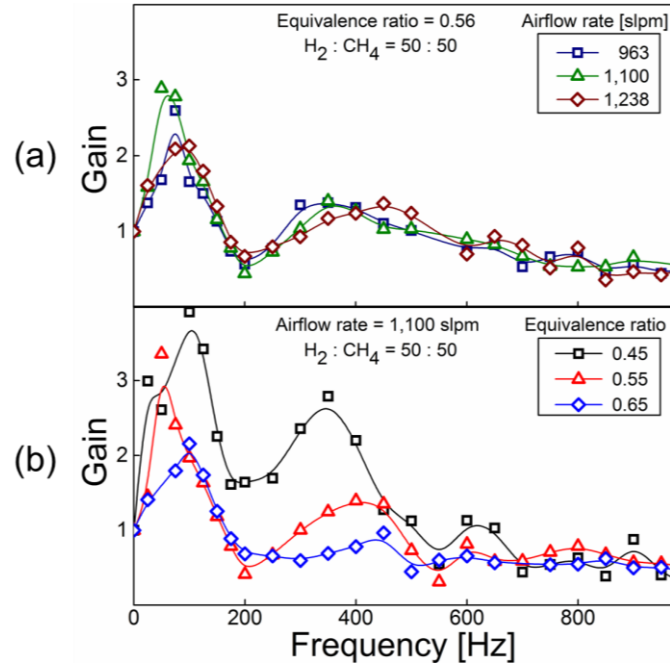


Fig. 5.2 Measured FTF gain for (a) airflow rate and (b) ϕ variations.

Fig. 5.2 shows the FTF gain acquired by two tests and conducted using the fixed 50% H_2 fuel composition condition. One test varied the airflow rate at a fixed ϕ of 0.56, and the other varied the ϕ at a fixed airflow rate of 1100 slpm. As shown in Fig. 5.2(a), the airflow rate variation did not significantly affect the FTF gain variation, while Fig. 5.2(b) shows that the ϕ change causes a significant variation in the FTF gain, which was very similar to the variations in the H_2 composition shown in Fig. 5.1(a). In conclusion, the FTF, which reflects the flame characteristics, is mainly affected by variables such as the fuel composition or the ϕ , which can drastically modulate the flame shape and τ_{conv} . This conclusion is well matched with the findings from the FMS tests shown in Fig. 4.3 and Fig. 4.4. The airflow rate variation in the fixed ϕ condition, which results in little variation of the τ_{conv} , and shows no difference in the instability mode and the FTF gain characteristics. In contrast, changes in variables such as the fuel composition and the ϕ , which can control the τ_{conv} , were shown to significantly change FMS and the FTF.

5.3 Gain Trend Analysis

Figs. 5.1 and 5.2 depict the interesting characteristics of the FTF gain trend during modulation frequency variations. The local maximum and local minimum variation trends for the gain were found, and the characteristics for the gain in this study were compared with those in previous research.

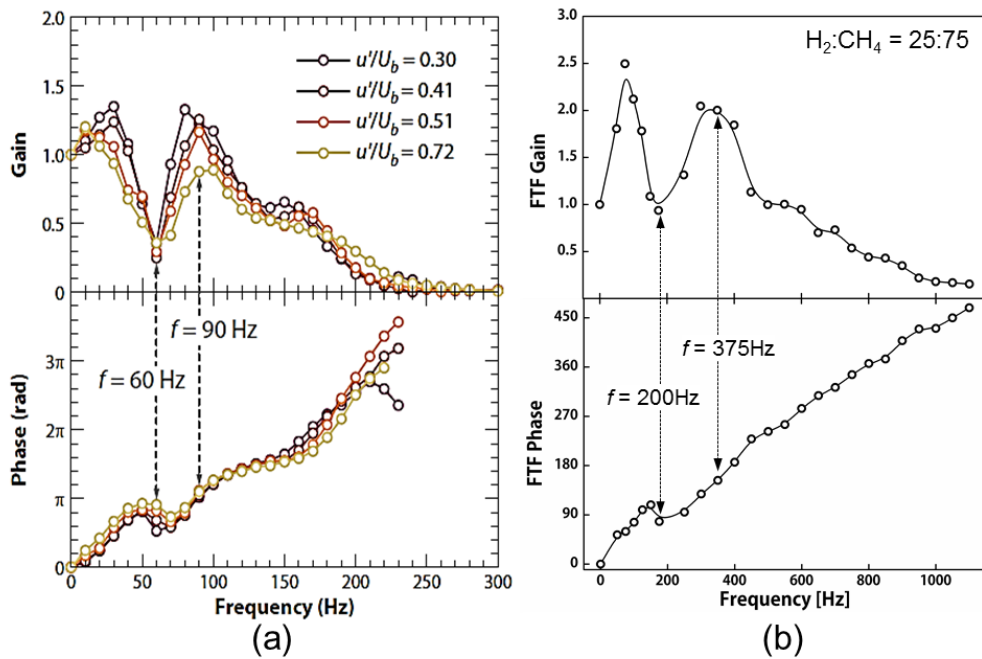


Fig. 5.3 Measured FTF gain trend comparison between premixed and partially premixed combustor (a) CNRS, (b) present study

Fig. 5.3(a) shows the measured FTF gain and phase trends obtained in the fully premixed combustor from Candel et al [43]. Fig. 5.3(b) shows the H₂ 25% FTF results of this study. Both sets of results show similar variation trends not only for the FTF gain but also for the FTF phase. However, the frequency range and the minimum frequency of the FTF gain were not identical for the two studies. The differences in instability characteristics

were mainly influenced by the differences in experimental facilities. However, the different combustion type (fully versus partially premixed combustor) did not significantly influence the trend characteristics of the FTF. It is assumed that the similar flame structure provides the most important characteristics of the flame. Preetham et al. found the influence of the flame structure in the FTF characteristics by comparing a conical flame to a V-shaped flame [42]. Structural variations exert the main influence on the gain trend for FTF; the previously measured FTF (in the premixed combustor) and the measured FTF from the partially premixed combustor had similar swirl, stabilized V-shaped flames. Flame is also stabilized using a dump-shape combustor; these similarities directly influence similarities in the characteristics of the FTF gain.

Our previous analysis was introduced in this chapter to provide further understanding of the gain trend characteristics of FTF. Candel et al. [43] suggested the mechanism of low maximum and minimum variation trends as shown in Fig. 5.4.

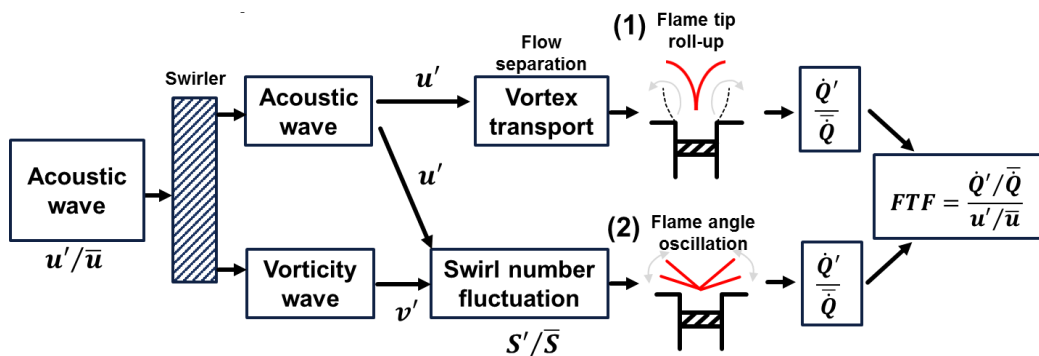


Fig. 5.4 Block diagram representation of mechanisms generating heat-release rate fluctuations in swirling flows (Candel et al. 2014) [43].

Acoustic fluctuations induce azimuthal velocity perturbations that combine with axial disturbances to give rise to swirl number fluctuations. In the linear regime, these perturbations are linked as shown in Equation 5.3 (Palies et al. 2010) [14]. S means the swirl number, v means the radial average velocity and u means the axial average velocity.

$$\frac{S'}{S} = \frac{v'}{v} - \frac{u'}{u} \quad (5.3)$$

Consequently, two processes induce heat release rate fluctuations the first through the direct effect of axial velocity fluctuations generating vortices at the dump plane, which in turn roll up the flame; the second resulting from flame angle oscillations due to swirl number oscillations. This has a direct impact on the swirling FTF, which features local minimum and maximum gain values that reflect the constructive or destructive interferences of the breathing motion and angle oscillation of the flame. Conditions leading to large swirl number oscillations induce a weak flame response; conversely, when swirl number fluctuations are absent, oscillations of the heat release rate reach a maximum [43].

The occurrence of the local minimum and maximum value of the FTF gain can be explained as shown in Fig. 5.5. The local maximum values were found at 100 Hz, with a constructive interaction being found. In contrast, the local minimum value was found in the 200 Hz modulation, with estimation of a destructive interaction.

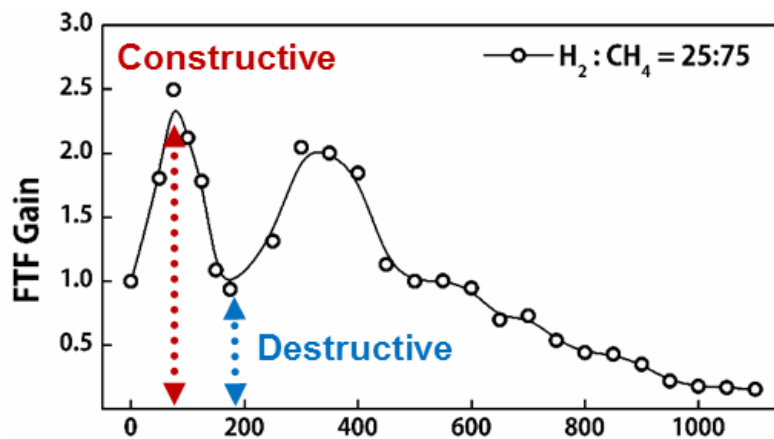


Fig. 5.5 Constructive and destructive interaction between flame breathing motion and flame angle oscillation in the FTF gain

5.4 Instability Prediction

The final objective of research into combustion instability is the desire to accurately predict its occurrence. The achievement of a general solution for instability prediction is very difficult, and many researchers are currently tackling this problem worldwide. However, the prediction of combustion instability in a lab-scale combustor has been successfully studied in recent years. The key parameter for the prediction of lab-scale experimental combustion instability is the accurate measurement of FTF. From the measured FTF, the heat release output during inlet fluctuation can be derived and the Helmholtz equation can be solved as the use of FTF as the unknown variable. OSCILOS (an open source code for simulating combustion instability; www.oscilos.com/) is a program that includes a Helmholtz equation solver, and through the program, combustion instability characteristics were predicted for our model combustor.

The fitted polynomial equation of the measured FTF was used as the simulation parameter and the reflection coefficient of inlet and outlet were selected as the fixed value (e.g., 1). The basic model of OSCILOS was the premixed combustor; the inlet fuel and air was simulated as the mixture to fulfill the initial condition of the calculation.

The predicted amplitude was ignored because the model and calculation solver has the limitation of being different from the actual conditions at the testing facility. The main focus of the prediction in this study was the prediction of peak frequency for combustion instability for each test condition, and (furthermore) the combustion instability at each test condition and its shift trend. The prediction was applied from H₂ 25% to 87.5% because the FTF was only measured in previously mentioned condition for the limitation of the velocity measurement facility. Fig. 5.6(a) shows the measured instability mode shifting phenomenon; Fig. 5.6(b), the predicted instability frequency based on OSCILOS. Some difference existed between the measured and predicted instability frequencies. However, the instability shifting trend based on the variation of fuel composition was also predicted successfully. These successful predictions can be largely attributed to the use of real flame as part of the testing conditions.

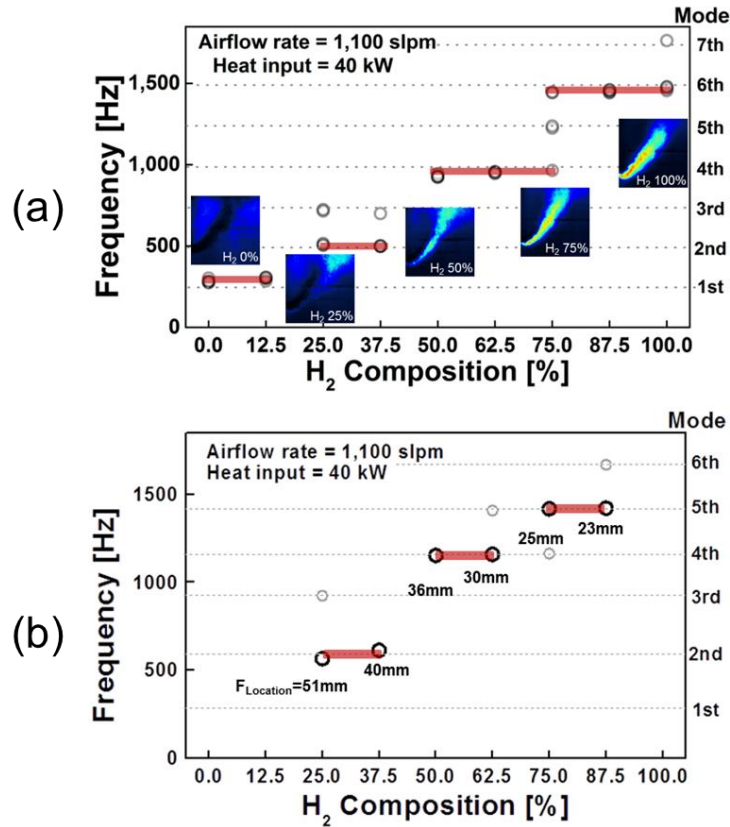


Fig. 5.6 Instability FMS phenomenon during the fuel composition variation (a) experimental results, (b) flame location considered prediction results.

The flame structure (discussed in Chapter 4) is a major parameter that affects combustion stability. The reduction in the flame's length is directly related to the convection time, and the reduction of the τ_{conv} is the main reason for the presence of the instability mode shifting phenomenon. Therefore, the usage of accurate flame structure with the FTF is the main reason for the proper prediction of instability mode shifting phenomenon in this study. In addition, the basic mechanism of instability mode shifting introduced in this research also assisted with the successful prediction of combustor instability.

CHAPTER 6

CONCLUSION

In this study, combustion instability characteristics were found in partially premixed combustor. The dynamic pressure data measurement and flame visualization technique were applied in various fuel composition for a fundamental study of the fuel flexibility problem. The reason of high harmonic instability and multi-mode instability were analyzed. Finally, the FTF were also measured in partially premixed combustor. A summary of the findings is as follows

First instability characteristics were found in $H_2/CH_4/CO$ composed fuel composition. The combustion instability occurred in the high H_2/CH_4 composed fuel, and an increase in the CO concentration of the fuel results in a decrease in the dynamic pressure amplitude. That is, when you change the fuel in the process of operating a gas turbine for synthesis gas, it is important to design a sequence that is able to avoid combustion instability. In addition, an increase in the inlet temperature affects the instability region, which must be related to the chemical properties of the fuel. In this study, the 3rd, 4th, and 6th instabilities were found by mode analysis and FFT of the dynamic pressure data in the unstable condition. The dump plane temperature increase was found in the unstable condition and the reason for this phenomenon was studied using flame visualization techniques. The phase-resolved OH-PLIF images showed that a large amount of the OH radical was formed in the unstable condition near the dump plane and it resulted in the dump plane temperature variation. Therefore, the dump plane temperature might be considered to be a variable in the combustion diagnostics of a gas turbine system.

Second, the relationship between FMS and fuel composition variations was identified, and the reason for FMS was analyzed using an experimental approach. The FMS was observed as the H_2 composition of the fuel increased. Variation in the τ_{conv} was the main reason for this phenomenon, and this finding was confirmed by τ_{conv} variation tests. A drastic variation in the τ_{conv} , which results in FMS, was found for the variables of fuel

composition and ϕ . In addition, the $\tau_{\text{conv_global}}$ of each test case was calculated based on the length of the unburned mixture region and fuel injection velocity, and the $\tau_{\text{conv_real}}$ was also calculated by the PIV-based actual flow field. The results from the τ_{conv} variation experiments identified a correlation between the length of the τ_{conv} and the FMS. The calculated $\tau_{\text{conv_global}}$ overlapping of each mode was shown, and matched well with the time-lag analysis-based instability occurrence theory. In other words, the instability triggering condition for each mode exists as the range, not a specific value. In conclusion, the length of the τ_{conv} is the trigger for FMS by selecting the specific frequency among the various intrinsic CI frequency modes, which are defined by the combustor geometry.

Third, the study on multi-mode instability in a partially premixed model combustor under varying test conditions using an experimental approach was conducted. The instabilities that occurred in the partially premixed combustor were analyzed and categorized in six cases based on time and frequency domain analysis. However, the time domain analysis and frequency domain analysis showed both the benefits and limitations in each approach. Therefore, continuous wavelet transform was applied to analyze the dynamic data and report the variations of the characteristic frequency based on time. From the continuous wavelet transform application, the multi-mode instability was separated into two cases. One case was the co-existence of the various instability frequencies, which was reflected as the deformed shape of the time domain dynamic pressure signal. The other case was the instability that mainly occurred in the specific frequency but travelled to the other frequencies in a very short time period. The cause of the multi-mode instability occurrence, which contained the co-existing instability and intermittent instability, was studied. In conclusion, the multi-mode instability mainly occurred in the τ_{conv} overlapping region. It was suspected that the time-lag-based instability possible region satisfied various instability modes. The instability mode co-existence or travelling phenomenon was found in the previously mentioned condition. In summary, multi-mode instability is unique and an unknown part of combustion instability research. However the fundamental instability occurrence mechanism of the multi-mode phenomenon is the same as that of the common instability theory. A suitable application of traditional instability analysis theory will be

useful for understanding multi-mode instability.

Finally, the FTF was measured to determine the intrinsic characteristics of the combustor, and the phase was normalized by the St. The FTF response was found by τ_{conv} variation tests (airflow rate and ϕ variation). The FTF gain characteristics remained during the airflow rate variations but changed drastically with variations in the fuel composition and the ϕ . This finding shows that the τ_{conv} changes alter FMS and influence the FTF characteristics. In other words, the FTF characteristics of the flame are predicted by the understanding of the τ_{conv} . The FTF gain trend was analyzed based on comparison of previous research and the high harmonic instability prediction possibility was also confirmed.

In conclusion, the τ_{conv} of the partially premixed combustion system is a key parameter in determining the CI mode and the intrinsic characteristics of the flame. In particular, FMS is controllable, and a specific mode of CI can even be generated by adjusting the τ_{conv} from the inverse correlation between the CI frequency and the τ_{conv} . In other words, the optimization of the τ_{conv} is an effective way to control the CI phenomenon in a partially premixed type combustor. In addition, understanding of high mode instability, which might be easily found in a high H_2 concentration fueled combustor, can be used for the development of the fuel-flexible gas turbine combustor.

REFERENCES

- [1] I. statistics, Energy balances of oecd countries, International Energy Agency, Place (2015).
- [2] S. Dodo, T. Asai, H. Koizumi, H. Takahashi, S. Yoshida and H. Inoue, Performance of a multiple-injection dry low NO_x combustor with hydrogen-rich Syngas fuels, *Journal of Engineering for Gas Turbines and Power*, 135 (1) (2013) 011501.
- [3] Q. Song, A. Fang, G. Xu, Y. Xu and W. Huang, Experimental investigation of thermoacoustic oscillations in syngas premixed multi-swirler model combustors, ASME Turbo Expo 2009: Power for Land, Sea, and Air, (2009) 669-678.
- [4] L. Figura, J.G. Lee, B.D. Quay and D.A. Santavicca, The effects of fuel composition on flame structure and combustion dynamics in a lean premixed combustor, ASME Turbo Expo 2007: Power for Land, Sea, and Air, (2007) 181-187.
- [5] T. Lieuwen, V. McDonell, E. Petersen and D. Santavicca, Fuel flexibility influences on premixed combustor blowout, flashback, autoignition, and stability, *Journal of engineering for gas turbines and power*, 130 (1) (2008) 011506.
- [6] T. Lieuwen, V. Yang and R. Yetter, Synthesis gas combustion: fundamentals and applications, CRC Press, Place (2009).
- [7] T. Lieuwen, Investigation of combustion instability mechanisms in premixed gas turbines, Mechanical Engineering, Doctor (1999).
- [8] T. Lieuwen, H. Torres, C. Johnson and B.T. Zinn, A mechanism of combustion instability in lean premixed gas turbine combustors, *Journal of Engineering for Gas Turbines and Power*, 123 (1) (2001) 182.
- [9] C. Kùlsheimer and H. Bùchner, Combustion dynamics of turbulent swirling flames, *Combustion and flame*, 131 (1) (2002) 70-84.
- [10] K.I. Matveev and F.E.C. Culick, A model for combustion instability involving vortex shedding, *Combustion Science and Technology*, 175 (6) (2003) 1059-1083.
- [11] N. Syred, A review of oscillation mechanisms and the role of the precessing vortex core (PVC) in swirl combustion systems, *Progress in Energy and Combustion*

- Science*, 32 (2) (2006) 93-161.
- [12] A.M. Steinberg, I. Boxx, M. Stöhr, C.D. Carter and W. Meier, Flow–flame interactions causing acoustically coupled heat release fluctuations in a thermo-acoustically unstable gas turbine model combustor, *Combustion and Flame*, 157 (12) (2010) 2250-2266.
- [13] S. Wang, S.-Y. Hsieh and V. Yang, Unsteady flow evolution in swirl injector with radial entry. I. Stationary conditions, *Physics of Fluids*, 17 (4) (2005) 045106.
- [14] P. Palies, D. Durox, T. Schuller and S. Candel, The combined dynamics of swirler and turbulent premixed swirling flames, *Combustion and Flame*, 157 (9) (2010) 1698-1717.
- [15] K.T. Kim and D.A. Santavicca, Interference mechanisms of acoustic/convective disturbances in a swirl-stabilized lean-premixed combustor, *Combustion and Flame*, 160 (8) (2013) 1441-1457.
- [16] I. Boxx, M. Stöhr, C. Carter and W. Meier, Temporally resolved planar measurements of transient phenomena in a partially pre-mixed swirl flame in a gas turbine model combustor, *Combustion and Flame*, 157 (8) (2010) 1510-1525.
- [17] M. Stöhr, C.M. Arndt and W. Meier, Transient effects of fuel–air mixing in a partially-premixed turbulent swirl flame, *Proceedings of the Combustion Institute*, 35 (3) (2015) 3327-3335.
- [18] Q.Z. David R. Noble, Tim Lieuwen, Syngas fuel composition sensitivities of combustor flashback and blowout, 23rd International Pittsburgh Coal Conference, (2006).
- [19] P.M. Allison, J.F. Driscoll and M. Ihme, Acoustic characterization of a partially-premixed gas turbine model combustor: Syngas and hydrocarbon fuel comparisons, *Proceedings of the Combustion Institute*, 34 (2) (2013) 3145-3153.
- [20] P.M. Allison, Y. Chen, M. Ihme and J.F. Driscoll, Coupling of flame geometry and combustion instabilities based on kilohertz formaldehyde PLIF measurements, *Proceedings of the Combustion Institute*, 35 (3) (2015) 3255-3262.
- [21] M.C. Lee, J. Yoon, S. Joo, J. Kim, J. Hwang and Y. Yoon, Investigation into the cause

- of high multi-mode combustion instability of H₂/CO/CH₄ syngas in a partially premixed gas turbine model combustor, *Proceedings of the Combustion Institute*, 35 (3) (2015) 3263-3271.
- [22] R. Balachandran, S.R. Chakravarthy and R.I. Sujith, Characterization of an acoustically self-excited combustor for spray evaporation, *Journal of Propulsion and Power*, 24 (6) (2008) 1382-1389.
- [23] G. Billoud, M.A. Galland, C. Huynh Huu and S. Candel, Adaptive active control of combustion instabilities, *Combustion Science and Technology*, 81 (4-6) (1992) 257-283.
- [24] S.J. Shanbhogue, Y.S. Sanusi, S. Taamallah, M.A. Habib, E.M.A. Mokheimer and A.F. Ghoniem, Flame macrostructures, combustion instability and extinction strain scaling in swirl-stabilized premixed CH₄/H₂ combustion, *Combustion and Flame*, 163 (2016) 494-507.
- [25] F. Boudy, D. Durox, T. Schuller and S. Candel, Nonlinear mode triggering in a multiple flame combustor, *Proceedings of the Combustion Institute*, 33 (1) (2011) 1121-1128.
- [26] J. Yoon, S. Joo, J. Kim, M.C. Lee, J.G. Lee and Y. Yoon, Effects of convection time on the high harmonic combustion instability in a partially premixed combustor, *Proceedings of the Combustion Institute*, (2016) in press.
- [27] J.H. Roel A.J. Muller, Wolfgang Polifke, Stability limits and non-linear characteristics of a self-excited combustion instability, 19th International Congress on Sound and Vibration (2012).
- [28] S.W. Hester, W.E. Anderson, M. Zoltowski and T.W. Feldman, High frequency signal analysis methods for acoustic modal onset in a continuously varying resonance combustor, (2014).
- [29] N. Noiray, D. Durox, T. Schuller and S. Candel, A unified framework for nonlinear combustion instability analysis based on the flame describing function, *Journal of Fluid Mechanics*, 615 (2008) 139.
- [30] C.M. Coats, Z. Chang and P.D. Williams, Excitation of thermoacoustic oscillations

- by small premixed flames, *Combustion and Flame*, 157 (6) (2010) 1037-1051.
- [31] Shreekrishna, S. Hemchandra and T. Lieuwen, Premixed flame response to equivalence ratio perturbations, *Combustion Theory and Modelling*, 14 (5) (2010) 681-714.
- [32] P. Palies, D. Durox, T. Schuller and S. Candel, Nonlinear combustion instability analysis based on the flame describing function applied to turbulent premixed swirling flames, *Combustion and Flame*, 158 (10) (2011) 1980-1991.
- [33] K.S. Kedia and A.F. Ghoniem, An analytical model for the prediction of the dynamic response of premixed flames stabilized on a heat-conducting perforated plate, *Proceedings of the Combustion Institute*, 34 (1) (2013) 921-928.
- [34] B. Schuermans, F. Guethe and W. Mohr, Optical transfer function measurements for technically premixed flames, *Journal of Engineering for Gas Turbines and Power*, 132 (8) (2010) 081501.
- [35] L. Tay-Wo-Chong and W. Polifke, Large eddy simulation-based study of the influence of thermal boundary condition and combustor confinement on premix flame transfer functions, *Journal of Engineering for Gas Turbines and Power*, 135 (2) (2013) 021502.
- [36] D. Kim, J.G. Lee, B.D. Quay, D.A. Santavicca, K. Kim and S. Srinivasan, Effect of flame structure on the flame transfer function in a premixed gas turbine combustor, *Journal of Engineering for Gas Turbines and Power*, 132 (2) (2010) 021502.
- [37] K.T. Kim, J.G. Lee, H.J. Lee, B.D. Quay and D.A. Santavicca, Characterization of forced flame response of swirl-stabilized turbulent lean-premixed flames in a gas turbine combustor, *Journal of Engineering for Gas Turbines and Power*, 132 (4) (2010) 041502.
- [38] T. Yi and D.A. Santavicca, Flame transfer functions for liquid-fueled swirl-stabilized turbulent lean direct fuel injection combustion, *Journal of Engineering for Gas Turbines and Power*, 132 (2) (2010) 021506.
- [39] K.T. Kim and D. Santavicca, Linear stability analysis of acoustically driven pressure oscillations in a lean premixed gas turbine combustor, *Journal of Mechanical*

- Science and Technology*, 23 (12) (2010) 3436-3447.
- [40] K.T. Kim, J.G. Lee, B.D. Quay and D.A. Santavicca, Spatially distributed flame transfer functions for predicting combustion dynamics in lean premixed gas turbine combustors, *Combustion and Flame*, 157 (9) (2010) 1718-1730.
- [41] S.M.R. Hosseini, C. Gardner and C. Lawn, The non-linear thermo-acoustic response of a small swirl burner, *Combustion and Flame*, 159 (5) (2012) 1909-1920.
- [42] Preetham, H. Santosh and T. Lieuwen, Dynamics of laminar premixed flames forced by harmonic velocity disturbances, *Journal of Propulsion and Power*, 24 (6) (2008) 1390-1402.
- [43] S. Candel, D. Durox, T. Schuller, J.-F. Bourgouin and J.P. Moeck, Dynamics of swirling flames, *Annual Review of Fluid Mechanics*, 46 (1) (2014) 147-173.
- [44] K.T. Kim and S. Hochgreb, Measurements of triggering and transient growth in a model lean-premixed gas turbine combustor, *Combustion and Flame*, 159 (3) (2012) 1215-1227.
- [45] M. Mathur and M. NR, Swirling air jets issuing from vane swirlers. 1. Free jets, *Journal of the Institute of Fuel*, 40 (316) (1967) 214-&.
- [46] J.M. Seitzman, A. Üngüt, P.H. Paul and R.K. Hanson, Imaging and characterization of OH structures in a turbulent nonpremixed flame, Symposium (International) on Combustion, 23 (1) (1991) 637-644.
- [47] S.R. Turns, An introduction to combustion, McGraw-hill New York, Place (1996).
- [48] M. Stöhr, C. Arndt and W. Meier, Effects of Damköhler number on vortex-flame interaction in a gas turbine model combustor, *Proceedings of the Combustion Institute*, 34 (2) (2013) 3107-3115.
- [49] M. Stöhr, I. Boxx, C. Carter and W. Meier, Dynamics of lean blowout of a swirl-stabilized flame in a gas turbine model combustor, *Proceedings of the Combustion Institute*, 33 (2) (2011) 2953-2960.
- [50] P. Petersson, R. Wellander, J. Olofsson, H. Carlsson, C. Carlsson, B.B. Watz, N. Boetkjaer, M. Richter, M. Aldén and L. Fuchs, Simultaneous high-speed PIV and OH PLIF measurements and modal analysis for investigating flame-flow interaction

- in a low swirl flame, *International Symposium Applied Laser Technical Fluid Mechanical*, (2012) 09-12.
- [51] P. Xavier, A. Vandiel, G. Godard, B. Renou, F. Grisch, G. Cabot, M.A. Boukhalfa and M. Cazalens, Analysis of the flame structure in a trapped vortex combustor using low and high-speed OH-PLIF, *ASME Turbo Expo 2014: Turbine Technical Conference and Exposition*, (2014) V04AT04A012-V004AT004A012.
- [52] J. Dawson, R. Gordon, J. Kariuki, E. Mastorakos, A. Masri and M. Juddoo, Visualization of blow-off events in bluff-body stabilized turbulent premixed flames, *Proceedings of the Combustion Institute*, 33 (1) (2011) 1559-1566.
- [53] N.A. Worth and J.R. Dawson, Cinematographic OH-PLIF measurements of two interacting turbulent premixed flames with and without acoustic forcing, *Combustion and Flame*, 159 (3) (2012) 1109-1126.
- [54] S. Hammack, S. Kostka, A. Lynch, C. Carter and T. Lee, Simultaneous 10-kHz PLIF and chemiluminescence imaging of OH radicals in a microwave plasma-enhanced flame, *IEEE Transactions on Plasma Science*, 41 (12) (2013) 3279-3286.
- [55] S. Meares, V.N. Prasad, M. Juddoo, K.H. Luo and A.R. Masri, Simultaneous planar and volume cross-LIF imaging to identify out-of-plane motion, *Proceedings of the Combustion Institute*, 35 (3) (2015) 3813-3820.
- [56] K. Ahn, J.-H. Kim and Y. Yoon, Application of PIV to over-expanded supersonic flows: Possibilities and limits, *Journal of visualization*, 6 (4) (2003) 353-361.
- [57] G. Liskiewicz and L. Horodko, Time-frequency analysis of the surge onset in the centrifugal blower, *Open Engineering*, 5 (1) (2015).
- [58] A. Renaud, S. Ducruix and L. Zimmer, Bistable behaviour and thermo-acoustic instability triggering in a gas turbine model combustor, *Proceedings of the Combustion Institute*, (2016) in press.
- [59] W. Li, F. Gu, A.D. Ball, A.Y.T. Leung and C.E. Phipps, A study of the noise from diesel engines using the independent component analysis, *Mechanical Systems and Signal Processing*, 15 (6) (2001) 1165-1184.
- [60] A.K. Sen, G. Litak, B.F. Yao and G.X. Li, Analysis of pressure fluctuations in a

- natural gas engine under lean burn conditions, *Applied Thermal Engineering*, 30 (6-7) (2010) 776-779.
- [61] A.K. Sen, J. Zheng and Z. Huang, Dynamics of cycle-to-cycle variations in a natural gas direct-injection spark-ignition engine, *Applied Energy*, 88 (7) (2011) 2324-2334.
- [62] D.P. Jena and S.N. Panigrahi, Motor bike piston-bore fault identification from engine noise signature analysis, *Applied Acoustics*, 76 (2014) 35-47.
- [63] C.O. Paschereit, B. Schuermans, W. Polifke and O. Mattson, Measurement of transfer matrices and source terms of premixed flames, *Journal of Engineering for Gas Turbines and Power*, 124 (2) (2002) 239.
- [64] A. Sengissen, J. Vankampen, R. Huls, G. Stoffels, J. Kok and T. Poinso, LES and experimental studies of cold and reacting flow in a swirled partially premixed burner with and without fuel modulation, *Combustion and Flame*, 150 (1-2) (2007) 40-53.
- [65] K.P. Geigle, W. Meier, M. Aigner, C. Willert, M. Jarius, P. Schmitt and B. Schuermans, Phase-resolved laser diagnostic measurements of a downscaled, fuel-staged gas turbine combustor at elevated pressure and comparison to LES predictions, *Journal of Engineering for Gas Turbines and Power*, 129 (3) (2007) 680.
- [66] G.J.M.S. W. S. Cheung, R.W. Copplestone, J. R. Tilston, C.W. Wilson, Simon R. Stow, Ann P. Dowling, Measurement and analysis of flame transfer function in a sector combustor under high pressure conditions, Proceedings of ASME Turbo Expo 2003 Power for Land, Sea, and Air, (2003).
- [67] C.H. A. Gentemann, K. Kunze, F. Kiesewetter, T. Sattelmayer, W. Polifke, Validation of flame transfer function reconstruction for perfectly premixed swirl flames, Proceedings of ASME Turbo Expo 2004 Power for Land, Sea, and Air, (2004).
- [68] T. Poinso and D. Veynante, Theoretical and numerical combustion, RT Edwards, Inc., Place (2005).
- [69] X. Han, J. Li and A.S. Morgans, Prediction of combustion instability limit cycle oscillations by combining flame describing function simulations with a thermoacoustic network model, *Combustion and Flame*, 162 (10) (2015) 3632-3647.
- [70] L. Selle, G. Lartigue, T. Poinso, R. Koch, K.-U. Schildmacher, W. Krebs, B. Prade,

- P. Kaufmann and D. Veynante, Compressible large eddy simulation of turbulent combustion in complex geometry on unstructured meshes, *Combustion and Flame*, 137 (4) (2004) 489-505.
- [71] J. Li and A.S. Morgans, Time domain simulations of nonlinear thermoacoustic behaviour in a simple combustor using a wave-based approach, *Journal of Sound and Vibration*, 346 (2015) 345-360.
- [72] C.F. Silva, F. Nicoud, T. Schuller, D. Durox and S. Candel, Combining a Helmholtz solver with the flame describing function to assess combustion instability in a premixed swirled combustor, *Combustion and Flame*, 160 (9) (2013) 1743-1754.
- [73] N. Bouvet, F. Halter, C. Chauveau and Y. Yoon, On the effective Lewis number formulations for lean hydrogen/hydrocarbon/air mixtures, *International journal of hydrogen energy*, 38 (14) (2013) 5949-5960.
- [74] M.-K. Kim, J. Yoon, J. Oh, J. Lee and Y. Yoon, An experimental study of fuel–air mixing section on unstable combustion in a dump combustor, *Applied Thermal Engineering*, 62 (2) (2014) 662-670.
- [75] L.E. Kinsler, A.R. Frey, A.B. Coppens and J.V. Sanders, Fundamentals of acoustics, Fundamentals of Acoustics, 4th Edition, by Lawrence E Kinsler, Austin R Frey, Alan B Coppens, James V Sanders, pp 560 ISBN 0-471-84789-5 Wiley-VCH, December 1999, 1 (1999).
- [76] E. Awad and F. Culick, On the existence and stability of limit cycles. for longitudinal acoustic modes in a combustion chamber, *Combustion Science and Technology*, 46 (3-6) (1986) 195-222.
- [77] C. Dong, Q. Zhou, Q. Zhao, Y. Zhang, T. Xu and S. Hui, Experimental study on the laminar flame speed of hydrogen/carbon monoxide/air mixtures, *Fuel*, 88 (10) (2009) 1858-1863.
- [78] B. Jones, J.G. Lee, B.D. Quay and D.A. Santavicca, Flame response mechanisms due to velocity perturbations in a lean premixed gas turbine combustor, *Journal of Engineering for Gas Turbines and Power*, 133 (2) (2011) 021503.
- [79] R.W. Grout, A. Gruber, C.S. Yoo and J.H. Chen, Direct numerical simulation of

flame stabilization downstream of a transverse fuel jet in cross-flow, *Proceedings of the Combustion Institute*, 33 (1) (2011) 1629-1637.

- [80] D.J. Micka and J.F. Driscoll, Stratified jet flames in a heated (1390K) air cross-flow with autoignition, *Combustion and Flame*, 159 (3) (2012) 1205-1214.

초 록

배기배출물 규제 강화 및 CO₂ 배출량 저감의 필요성에 따라 기존의 발전원에 대한 개선이 필요한 시점이다. 현재는 기존의 화석연료를 기반으로 한 에너지 시장에서 신재생 에너지로 넘어가는 과도기로, 새로운 에너지를 기반으로 한 발전 시스템이 기술적인 성숙을 이룰 수 있을 때까지, 기존의 발전 시스템 중 환경친화적인 가스복합화력 발전에 대한 관심이 높아지고 있다. 가스복합화력의 핵심인 가스터빈의 경우 석탄화력에 비하여 배기배출물 저감에 뛰어난 성능을 보이며, Syngas, SNG, Shale gas 등과 같은 새로운 연료의 적용이 용이한 장점이 있다. 이러한 신 연료는 기존연료와 달리, 연료 중 수소 비율이 높으며, 역화와 같은 연소과정의 문제를 최소화 하기 위하여 부분예혼합 혹은 확산화염의 형태의 연소가 필요하다. 따라서 연료의 다양성을 위한 가스터빈 연소기는 기존의 가스터빈 개발과는 그 방향성을 달리하며, 그러한 특성의 변화에 대한 상세한 연구가 필요하다. 이러한 연소기 개발 과정에서는 특히 연소불안정 문제를 주요한 이슈로 논의되고 있다.

본 연구에서는 연료조성의 변화가 부분예혼합 연소기에서 발생하는 연소불안정현상에 미치는 영향에 대하여 실험적으로 확인하였으며, 그 과정에서 계측된 고주파 연소불안정 모드에 대한 분류 및 원인 파악에 대한 상세 연구를 수행하였다. 또한 최근 활발한 연구가 이루어지고 있는 연소불안정 예측을 위하여, 화염전달함수 연구를 수행하였다.

우선 연료조성 변화에 따른 연소기의 특성파악을 위하여 수소/메탄/일산화탄소를 조성변화에 따라 45개의 연료조성에 대한 연소시험을 수행하였다. 그 결과 대부분의 연소불안정이 수소/메탄 연료조성에서 발생하는 것을 확인하였으며, 이러한 불안정조건에 대한 모드분석을 수행하였다. 연소기에서 발생하는 불안정이 길이방향 연소불안정의 3rd, 4th 그리고 6th 불안정임을 확인하였으며, 이에 대한 상세 연구를 위하여 연료조성을 수소/메탄으로 제한하였으며, 연소기 길이 및 부하 변동시험을 수행하였다. 연소기 길이 변경시험을 통하여 연소기에서 발생하는 불안정이 길이방향 모드임을 다

시 한번 확인하였으며 부하변동 시험과정에서도 길이방향 연소불안정의 공진 주파수로 고주파 불안정이 발생하는 것을 확인하였다.

연료조성변화에 따라 연소불안정 주파수가 1st 모드에서 6th 모드까지 증가하는 것을 확인하였으며, 이러한 모드천이현상의 원인 파악을 위하여 공기 공급속도, 당량비를 바꾸어가며 시험을 수행하였다. 다양한 인자에 대한 분석결과 화염의 구조적 변화가 연소불안정 모드천이현상에 직접적인 영향을 미치는 것으로 분석 되었으며, 또한 화염의 구조 변화는 시간지연 분석기법에서 convection time에 직접적으로 영향을 미치게 된다. 따라서 OH-PLIF 화염가시화 기법을 바탕으로 다양한 조건에 대한 convection time을 계산하였으며, 이를 통하여 연소불안정 모드 천이 현상과 convection time이 반비례 관계를 보임을 확인하였다. 이러한 convection time의 감소는 전체 시간지연의 감소를 야기하며, 간략화 된 Rayleigh's criteria 분석을 통하여 이러한 시간지연의 감소가 연소불안정 모드를 고주파 대역으로 천이시킬 것으로 예측 되었다.

상기 논의한 연소불안정 모드 천이 현상에 대한 상세 분석과정에서 다중 연소불안정 모드가 발생하는 것을 확인하였다. 이러한 다중모드의 원인 파악을 위하여 계측되었던 모든 조건의 불안정에 대한 분류를 수행하였으며, 시간에 따라 periodic 과 dynamic 두가지, 주파수 분석을 기반으로, FFT 분석 결과의 형태에 따라 single, dual 그리고 multiple frequency 세가지로 연소불안정 현상을 분류하였다. 이렇게 분류한 불안정 조건에 시간의 흐름에 따른 신호의 주파수 특성 변화를 한번에 파악할 수 있는 continuous wavelet transform을 적용하였다. 이를 통하여 다중모드 불안정의 경우 여러 개의 독립적인 불안정 주파수가 모든 시간변화에 관계 없이 존재하는 경우와 불안정 주파수가 지속적으로 변하는 경우로 나눌 수 있음을 확인하였다. 또한 연소불안정 모드 천이 과정에서 확인하였던 convection time 과 주파수의 반비례 상관관계에서 single frequency 조건만 남길 경우 convection time이 겹치는 영역이 제거됨을 확인하였다. 즉 열방출과와 압력과의 시간지연이 여러 주파수 대역의 연소불안정 가능영역을 만족시킬 경우 다중 모드 연소불안정이 발생하는 것으로 분석된다.

마지막으로 연소불안정 예측에 활용될 수 있는 화염전달함수에 대한 계측을 수행하였다. 연료조성에서의 수소비율 증가에 따라 화염전달함수 gain의 값이 감소하는 경

향을 보이는 것을 확인하였으며, 화염전달함수 위상의 감소율 또한 감소시키는 것으로 확인되었다. 동일한 열량공급을 위한 연료유량이 수소비율 증가에 따라 증가하게 되며, 이것이 연료의 공급속도 증가를 야기하여 섭동의 전파시간이 짧아지는 것으로 파악된다. 또한 공기공급속도, 당량비 변동 시험을 통하여 화염전달함수 특성에도 화염의 구조적 변화 및 convection time의 변화가 직접적으로 영향을 미치는 것으로 확인되었다. 이렇게 예측된 화염전달함수의 gain 값에 대한 기존의 연구와의 비교결과 gain 값 변동 특성의 원인을 파악하였다. 마지막으로 연소불안정 예측에 대한 예측을 수행한 결과 실제 실험에서 발생하였던 연소불안정 모드 천이현상을 예측결과에서 또한 확인할 수 있었다.

상기 연구를 통하여 부분예혼합 연소기에서 다양한 연료조건 변화에 따라 발생하는 고주파 연소불안정에 대한 다양한 특성을 파악하였으며 화염전달함수 특성연구를 수행하였다. 이러한 연구결과는 앞으로 다양한 연료를 적용할 수 있는 가스터빈 개발과정 및 고주파 공진 불안정에 대한 연구의 선행연구자료로 활용될 수 있을 것으로 기대된다.

중심어: 부분예혼합 연소기, 연소불안정, 연료다양성, 고주파 공진 불안정, 불안정 모드천이, 다중불안정 모드, 화염전달함수, OH-PLIF, PIV 연소불안정 예측

학 번: 2012-30180